Structural modifications and their effects on the catalytic behavior of metal surfaces and organometallic complexes:

Theoretical studies of oxygen adsorption on silver surfaces and aziridination catalysis by iron-tetracarbene complexes

A Dissertation Presented for the

Doctor of Philosophy

Degree

The University of Tennessee, Knoxville

Sara Beth Isbill

May 2019

© by Sara Beth Isbill, 2019
All Rights Reserved.

Acknowledgments

As I reflect on all of the moments that have led to the writing of this dissertation, I am overwhelmed by gratitude toward so many people. First, I thank my graduate advisor, Dr. Sharani Roy, for taking a chance on a young, insecure graduate student with little research and no computational experience. Under her mentoring, I have learned more than I can even begin to mention. I will forever think back to the things she has taught me over the last five years, not only about chemistry but about how to to conduct myself as a professional. I hope to make her proud as I carry her name on my resumé. I would also like to thank the rest of my dissertation committee, Dr. R. J. Hinde, Dr. Tessa Calhoun, and Dr. David Keffer. Through all of my exams, they have challenged me to constantly improve, and I thank them for all of their advice. I next thank my experimental collaborators for their many insightful conversations about the work we have done together. Thanks to my lab mates, who have encouraged me after rough group meetings, helped me prepared for qualifying exams, and listened to so many practice talks prior to conferences that they could have given the talk themselves. I must also thank the agencies that have funded our work and the organizations that manage the computational resources I have used. These include the National Institute of Health, National Science Foundation, The University of Tennessee, Knoxville, the Newton High-Performance Computing cluster, the Advanced Computing Facility, and XSEDE.

I would not have made it *through* graduate school without the aforementioned professors and colleagues; however, I would not have made it *to* graduate school with out those I must thank now. I would like to thank my science teachers and professors who first nurtured my love for science and who encouraged me to apply to the graduate program at UTK. Mr. Camp, my high school chemistry teacher, taught colligative properties by making ice cream in class and limiting reagents by making smore's. He was the faculty sponsor of

the Science Olympiad and Science Bowl teams. Through his many efforts, I gained an appreciation for science that has never left. I also thank him for the chemistry workbook he gave me upon hearing I was pursuing a degree in chemistry. This workbook still sits on my bookshelf. I also want to thank Dr. Matthew Krepps, Dr. Eddie Brown, Dr. Jonathan Hearn, and Dr. Johnny Evans. These men were my undergraduate chemistry professors, advisors, and mentors. They encouraged me to pursue graduate school and wrote the letters of recommendation that helped me reach UTK and ultimately the writing of this document.

I have saved the most important group of people for last. These are my family and friends, specifically my parents and sister. My younger sister, of whom I am so proud, has been my constant motivation to be my best. From a young age, my parent have worked to allow me to pursue my dreams, whether those dreams were to be an olympic gymnast (thanks to the 1996 olympic games) or to be a student for 20+ years. They have been an ear when I needed someone to talk with, a shoulder when life or school was hard, my cheerleader at even the smallest accomplishment to keep me motived, my sounding board when I had grand ideas such as staying a couple of days after a conference in California to visit Disneyland, my dog-sitter when I travelled to present my work, and so many other things. Without them, none of this would have been possible, and I am forever grateful.

Abstract

Great interest exists in efficient synthesis of epoxides and aziridines, molecules containing three-membered rings with oxygen and nitrogen atoms, respectively, due to their use in the chemical and pharmaceutical industries. Epoxides, such as ethylene oxide, can be partially oxidized to form ethylene glycol, a feedstock in many consumer products. Typically, ethylene oxide is made over a silver surface; however, there remain many questions as to the structure of the active catalyst. In this work, the interaction of atomic oxygen with two facets of silver has been investigated with molecular dynamics simulations and density functional theory (DFT) calculations. These studies revealed that oxygen interacts with Ag(111) and Ag(110) very differently as a function of coverage. The occupation of nearest-neighbor sites on the Ag(111) surface significantly decreases adsorption energies which is not observed on Ag(110). This result has been used to construct a simple adsorption model, which can predict the adsorption energy of a given arrangement of oxygen atoms if the number and types of neighbor interactions are known. Additionally, aziridines have been shown to possess antibiotic and anticancer properties. Due to enhanced stereochemical control, many aziridines are synthesized using organometallic catalysts. Our work investigates the effect of structural modifications on the reaction mechanism of two generations of iron-tetracarbene catalysts using DFT calculations. This study reveals both catalysts proceed through a radical intermediate, making them susceptible to intramolecular rotation, potentially reducing their stereochemical retention. We also show that the undesired metallotetrazene product can be destabilized by use of bulkier azides, further improving the atom-economy of the reaction. We then investigated further modifications of the second-generation catalyst, adding chiral wings in an effort to improve selectivity of a given enantiomer. This work reveals that though initially promising, these macrocycles do not catalyze aziridine through the same

mechanism as the achiral catalysts, if at all. In conclusion, our work reveals the complex role that structure plays in both homogeneous and heterogeneous catalytic systems.

Table of Contents

1 Introduction **1**

1.1 Background 1

1.1.1 Heterogeneous catalytic epoxidation over silver surfaces 2

1.1.2 Homogeneous catalytic aziridination using organometallic complexes . 5

1.2 Conclusion 8

2 Classical dynamics simulations of the interaction of atomic oxygen with Ag(111) and Ag(110) surfaces **9**

2.1 Disclosure 9

2.2 Introduction 9

2.3 Methods 11

2.3.1 Classical Molecular Dynamics Simulations 11

2.3.2 *Ab initio* calculations 12

2.3.3 Distributed work flow model 13

2.4 Results and discussion 14

2.4.1 Bulk Ag lattice parameters and unoxidized surface energies 15

2.4.2 Adsorption energies of isolated oxygen atoms: Comparison with DFT 17

2.4.3 Simulation of oxidized Ag surfaces 19

2.5 Conclusions 35

3 Adsorption of atomic oxygen on the Ag(111) surface **39**

3.1 Introduction 39

3.2 Methods 40

3.3 Results . . . 42
3.3.1 Pure surface and subsurface adsorption . . . 44
3.3.2 Mixed surface and subsurface adsorption . . . 48
3.3.3 Adsorption model . . . 48
3.4 Summary and conclusions . . . 50

4 Atomic Oxygen adsorption on Ag(110): A comparison with Ag(111) 52
4.1 Introduction . . . 52
4.2 Methods . . . 53
4.3 Results . . . 54
4.3.1 Surface relaxation of the clean surface . . . 55
4.3.2 Pure surface and subsurface adsorption . . . 57
4.3.3 Coverage dependence of work function . . . 59
4.4 Summary and conclusions . . . 60

5 Elucidation of the reaction mechanism of C_2 + N_1 aziridination from tetracarbene iron catalysts 61
5.1 Disclosure . . . 61
5.2 Introduction . . . 61
5.3 Methods . . . 64
5.4 Results and Discussion . . . 64
5.4.1 Formation of iron imides - Step A . . . 65
5.4.2 Formation of aziridines - Step B . . . 69
5.4.3 Formation of metallotetrazenes - Step C . . . 75
5.5 Conclusions . . . 78

6 Chiral iron-tetracarbene catalysts for stereoselective aziridination 80
6.1 Disclosure . . . 80
6.2 Introduction . . . 80
6.3 Methods . . . 81
6.4 Results . . . 81

6.4.1 Chiral iron-tetracarbene catalysts 82
6.4.2 Mechanistic investigation of favored chiral catalyst 84
6.5 Summary and Conclusions 86

7 Summary and Conclusions **87**
7.1 Interaction of atomic oxygen with Ag(111) and Ag(110) 87
7.2 Aziridination *via* iron-tetracarbene catalysts 89

Bibliography **91**

Appendix **105**

A Additional Tables and Figures from Chapter 2 **106**

Vita **117**

List of Tables

2.1 Number of atoms in MD simulations. 13

2.2 Surface energies (mJm^{-2}) of unoxidized Ag surfaces. 17

2.3 Results of ReaxFF and DFT calculations for adsorption energy for a single atomic oxygen bound to different binding sites on the relaxed Ag(111) surface. 18

2.4 Results of ReaxFF and DFT calculations for adsorption energy for a single atomic oxygen bound to different binding sites on the relaxed Ag(110) surface. 19

3.1 The adsorption energies (average and incremental) for a given set of mixed coverages investigated in the present study. 48

3.2 Calculated values of the O/Ag(111) adsorption model parameters. 50

5.1 Aziridination reactions with **5.1** and **5.2**. 73

5.2 Aziridination reactions with **5.1**. 78

A.1 Suite of 153 simulations performed the molecular dynamics investigations of the interaction of atomic oxygen with Ag(111) and Ag(110). 107

List of Figures

1.1 Structures of ethylene oxide and ethylene imide, the simplest oxygen- and nitrogen-containing three-membered rings. 1

1.2 Unreconstructed Ag(111) and Ag(110) surfaces. 3

2.1 Potential energies for bulk and unoxidized surface systems. 16

2.2 Time-averaged potential energy of oxygen as a function of temperature and coverage for the four different initial oxygen sites on the Ag(111) surface. . 20

2.3 Snapshots of the initial configuration (a) and the final configuration of the 0.5 fractional occupancy at 77 K (b), 300 K (c) and 500 K (d) for O atoms initially placed at the fcc hollow surface sites of the Ag(111) surface. 22

2.4 Plot of oxygen potential energy against charge shows a clear correlation between the two properties. 24

2.5 Plot of silver potential energy against fractional occupancy shows a clear correlation between the two properties. 26

2.6 Plots of the O-Ag RDF (a) and CN (b) for an oxygen atom at the hcp hollow site with a fractional coverage of 0.5 for various temperatures and the RDF (c) and CN (d) for an oxygen atom at the hcp hollow site at a temperature of 300 K for various fractional coverages. 28

2.7 Time-averaged potential energy of subsurface oxygen atoms as a function of temperature and coverage for the three different initial oxygen subsurface sites on Ag(111). 29

2.8 Snapshots of the initial configuration (a) and the final configuration (b) of the 0.5 fractional occupancy at 500 K for O atoms initially placed at the tetrahedral-3 subsurface sites of the Ag(111) surface. 30
2.9 Octahedral O-Ag RDF (a) and CN (b) and tetrahedral-1 O-Ag RDF (c) and CN (d) at 300 K and various fractional coverages. 31
2.10 Time-averaged potential energy of surface oxygen atoms as a function of temperature and coverage for the four different initial oxygen sites on the Ag(110) surface. 32
2.11 Snapshots of the initial configuration (a) and the final configuration of the 0.1 fractional occupancy at 77 K (b), 300 K (c) and 500 K (d) for O atoms initially placed at the fourfold hollow surface sites of the Ag(110) surface. . . 33
2.12 Snapshots of the initial configuration (a), the configuration at 0.138 ps (b), the configuration at 0.512 ps (c), and the final configuration (c) of the 1.0 fractional occupancy for O atoms initially placed at the fourfold hollow surface sites of the Ag(110) surface at 77 K. 34
2.13 O-Ag RDF (a) and CN (b) of the O atoms initially placed in the fourfold hollow site on Ag(110) at 77 K and the two extreme coverages studied. . . . 35
2.14 Time-averaged potential energy of subsurface oxygen atoms as a function of temperature and coverage for the four different initial oxygen sites on the Ag(110) surface. 36
2.15 Snapshots of the initial (a) and final (b) configurations for O atoms initially placed in the square pyramidal-1 (110) subsurface site and snapshots of the initial (c) and final (d) configurations for O atoms initially placed in the square pyramidal-4 (110) subsurface site. 37
2.16 O-Ag RDF (a) and CN (b) of O atoms placed at the long subsurface bridge and RDF (c) and CN (d) of O atoms placed at the square pyramidal-1 subsurface sites on the (110) surface at 300 K and various coverages. 38

3.1 Six-layer, (4×3) Ag(111) supercell. 41

3.2 Top-down and side views of the high-symmetry sites on the surface, in the subsurface, and in the second subsurface (subsurface-23) regions of the Ag(111) surface. 43
3.3 Average adsorption energy per AO ($E_{ads,avg}$) (left) and charge (right) as a function of AO coverage. 45
3.4 Incremental adsorption energy ($E_{ads,inc}$) as a function of coverage for the geometry at each coverage with the largest average interatomic oxygen spacing for the favored surface, subsurface, and subsurface-23 sites. 46
3.5 Top-down views of AO at the fcc hollow site for several coverages, showing the requirement that a nearest neighbor site be occupied beyond a coverage of 0.33 ML. For the 0.33 ML coverage and below, nearest-neighbor sites to an occupied fcc hollow site have been marked with an "x". Beyond this coverage, the added oxygen is marked with a green circle. 47
3.6 Average adsorption energy per AO ($E_{ads,avg}$) as a function of AO coverage calculated using the adsorption model developed in the present study. 51

4.1 Six-layer, (3×4) Ag(110) supercell. 54
4.2 Top-down and side views of the high-symmetry sites on the surface, in the subsurface, and in the second subsurface (subsurface-23) regions of the Ag(110) surface. 56
4.3 Top-down and side views of the relaxed Ag(111) and Ag(110) surfaces. . . . 57
4.4 Average adsorption energy per AO ($E_{ads,avg}$) as a function of AO coverage. . 58
4.5 Average work function of Ag(111) (left) and Ag(110) (right) surfaces as a function of AO coverage. 59

5.1 Catalytic cycle for the formation of aziridine from tetracarbene iron catalysts **5.1** and **5.2**. 63
5.2 DFT-computed free-energy pathway for formation of imide from reaction between an organic azide and **5.1**. 65

5.3 Energies, orbitals, and occupancies from DFT of the Fe d-orbital splitting of [(^{BMe_2},^{Et}TC^{H})Fe=N(tolyl)]. The zero of energy is set equal to the average energy of the d-orbitals of Fe. Canonical orbital surfaces are shown overlaying optimized molecular structures calculated with an isovalue of 0.04 with hydrogen atoms removed for clarity. 67
5.4 DFT-computed free-energy pathway for formation of imide from reaction between an organic azide and **5.2**. 68
5.5 DFT-computed free-energy pathway for formation of aziridine from *p*-tolyl imide and 1-decene using catalyst **5.1**. 70
5.6 General catalytic reaction. 71
5.7 DFT-computed free-energy pathway for formation of aziridine from *p*-tolyl imide and 1-decene using catalyst **5.2**. 74
5.8 DFT-computed free-energy pathway for formation of tetrazene from *p*-tolyl azide and mesityl azide with **1**. 76

6.1 Chiral iron tetracarbene catalysts for aziridination investigated in the present study. 82
6.2 Free energies (kcal/mol) of key species along the reaction pathway to aziridine for the four variations of iron-tetracarbene catalysts given in Figure 6.1. . . . 83
6.3 Possible bridge intermediates formed between the interaction of the cyclohexyl-winged imide (**6.2**) and 2,3,3-trimethylbutene. The two bridge intermediates differ only in the orientation of the methyl and *t*-butyl substituents relative to the macrocycle. On the left, the methyl substituent points toward the macrocycle while the *t*-butyl points toward the macrocycle on the right. . . . 85

A.1 Location of oxygens that were originally placed at the top site of the (111) surface at a 0.1 fraction coverage after relaxation. 106
A.2 Time-averaged charge on oxygen as a function of temperature and coverage for the four different initial oxygen sites on t he Ag(111) surface. 116

A.3 Time-averaged potential energy of surface silver atoms as a function of temperature and coverage for the four different initial oxygen sites on the Ag(111) surface. 116

Chapter 1

Introduction

1.1 Background

Some compounds containing heteronuclear three-membered rings have shown great promise as antibacterial agents.[1] Of special interest are rings that contain an oxygen or nitrogen atom, called epoxides and aziridines, respectively, shown in Figure 1.1. In fact, it has been shown that ethylene oxide, the simplest epoxide, and ethylene imine, the simplest aziridine, can be used as a gaseous disinfectant which is able to destroy microorganisms on a plethora of porous materials, such as bandages, food items, and moisture-sensitive medical equipment, that cannot be treated with other techniques.[1,2] Additionally, aziridines have been employed as antibiotics and cancer therapeutics.[3,4] Their large angle strain and high reactivity make both epoxides and aziridines ideal for ring-opening and ring-expansion reactions.[6–9] For example, ethylene oxide can be further oxidized to form ethylene glycol which is used in fuel cells, coolants, and polymerization reactions[5] while ring-opened aziridines can be used to

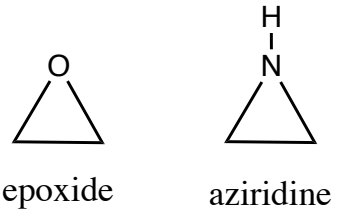


Figure 1.1: Structures of ethylene oxide and ethylene imide, the simplest oxygen- and nitrogen-containing three-membered rings.

form (-)-oseltamivir phosphate, the active ingredient in the influenza drug Tamiflu.[10]

Both homogeneous and heterogeneous catalysts are used to synthesize epoxides. In homogeneous catalysis, the reactant and product are in the same phase, for example, both in solution. A famous homogeneous catalyst developed by Jacobson showed high enantioselectivity for epoxidation with substituted alkenes.[11] This type of catalysis can yield products with high enantiomeric excess, in which the formation of one chiral product is favored over the other. This is ideal for pharmaceutical uses; therefore, many catalysts have been developed which homogeneously catalyze aziridines. A disadvantage of homogeneous catalysts is that additional reaction steps must be taken to separate the product and catalyst. The formation of ethylene oxide does not require such enantioselectivity as it is an achiral molecule. For synthesis of this species, heterogeneous catalysts offer a much simpler separation due to the existence of the product and catalyst in different phases, for example, gas-phase reactants adsorbing and reacting on a solid catalyst,[12] and are often used in the chemical industry. While significant advances have occurred for expoxidation with both types of catalysts, Section 1.1.1 will focus on the history and progress of heterogeneous catalysts. Section 1.1.2 will discuss the advances of homogeneous catalysts for enantioselective aziridination.

1.1.1 Heterogeneous catalytic epoxidation over silver surfaces

While the interaction of ethylene with oxygen has been studied over various transition metal surfaces, silver has shown a unique proficiency for the partial oxidation to form ethylene oxide.[13–15] Other surfaces favor full oxidation through an acetaldehyde intermediate, ultimately yielding combustion products CO, CO_2, and H_2O.[14] After years of investigating the mechanism of epoxidation, it has been shown that formation of an oxometallacycle intermediate is a key step for ethylene epoxidation on silver surfaces.[16–21] In this species, the carbon atoms of ethylene both bind to the surface, one to an adsorbed oxygen atom and the other directly to a silver atom.

While the epoxidation mechanism on silver has been elucidated, questions remain as to the structure of the catalytic surface, specifically under reaction conditions. Bulk silver has a face-centered-cubic (FCC) crystal structure. As with all crystals, bulk silver can be cleaved

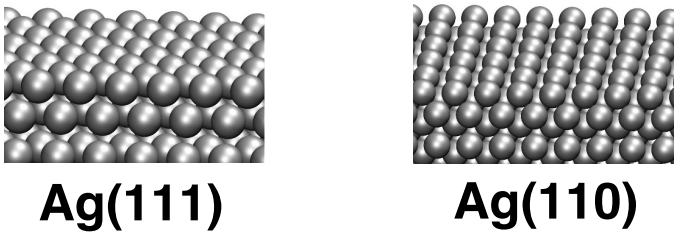


Figure 1.2: Unreconstructed Ag(111) and Ag(110) surfaces.

in different ways, leading to distinct surface-atom arrangements. Due to the atomically-flat nature of low-Miller-index surfaces, the interaction of both atomic and molecular oxygen with the (110) and (111) facets of silver have been intensely investigated.[22] As shown in Figure 1.2, the (111) surface of an FCC crystal has an $ABCABC$ stacking of the layers, with atoms in each layer arranged in hexagons. The (110) surface is significantly different with $ABAB$ stacking and a two-fold, rectangular symmetry. Once a surface has been made from a bulk crystal, the interlayer spacing of the first few layers can change as a result of the reduced coordination of the surface atoms. This phenomenon is known as surface relaxation. The surface can also change in the presence of adsorbates, known as surface reconstruction, in which the surface unit cell differs from the underlying bulk unit cell. The ratio of lattice vectors corresponding to these unit cells is often used to describe the nature of the reconstruction, known as Wood's notation.[23]

Surface-sensitive techniques such as low-energy electron diffraction (LEED),[23] x-ray photoelectron spectroscopy (XPS),[23] and scanning tunneling microscopy (STM)[24] have been instrumental in determining the surface reconstructions of silver in the presence of oxygen. Ag(110) is known to form a (2×1) adlayer, where oxygen atoms occupy bridge positions, as well as a missing-row variation of this (2×1) reconstruction.[25,26] Definitive models of the reconstructions on Ag(111) have been more elusive. Rovida *et al.* were the first to note the now famous Ag(111)-p(4×4) surface reconstruction in the presence of atomic oxygen using LEED.[27] They proposed this reconstruction consisted of a hexagonal arrangement of atoms in an Ag_2O trilayer. This structure was noted several years later by Campbell as

he determined the oxygen coverage in the reconstruction to be 0.41 ML using LEED, XPS, and temperature programmed desorption.[28] Since this time, modifications have been made to the reconstruction model proposed by Rovida *et al.* until two groups simultaneously, and seemingly independently, arrived at the same structure consisting of two Ag_6 triangles separated by furrows.[29,30] This structure was determined using a combination of STM, XPS, and density functional theory (DFT).[31] Many other reconstructions have been observed such as the c(5×$\sqrt{3}$),[29,32] $p(4\times5\sqrt{3})$,[29,32] and c(4×8),[33,34] all of which have surface-saturation coverages between 0.3 and 0.5 ML. Derouin *et al.* have shown that multiple reconstructions can co-exist on Ag(111) and are highly dependent on reaction conditions such as surface temperature and exposure time.[35]

While the surface structure under reaction conditions continues to be investigated, the active oxygen species during expoxidation has been identified. Two key oxygen species have been noted on silver surfaces: nucleophilic and electrophilic. Nucleophilic oxygen is involved in total oxidation, or combustion, while electrophilic oxygen leads to ethylene epoxidation. In an experiment using XPS and proton-transfer reaction mass spectrometry, high yields of ethylene oxide were only obtained in the presence of electrophilic oxygen. This species had a core-electron binding energy (CEBE) around 530 eV while the CEBE of nucleophilic oxygen was 528 eV.[36] Unfortunately, the nature of this species has not yet been definitively determined. Some have attributed the 530-eV oxygen species to surface contamination[33] or surface-bound atomic oxygen,[37] while others have assigned this peak to oxygen residing in the near-surface, or subsurface, region of silver.[38,39]

Several groups have considered the importance of subsurface oxygen on silver.[40–42] An extensive study of the interaction of atomic oxygen (AO) with Ag(111) was performed by Li, Stampfl, and Scheffler.[43,44] Using DFT, they investigated adsorption at all high-symmetry surface and subsurface sites at various coverages, as well as coverages containing both a surface and subsurface atom. Their work found the FCC and hexagonal-close packed (HCP) hollow sites to be the favored adsorption sites on the surface with adsorption energies of 3.6 and 3.4 eV, respectively, at a 0.11 ML coverage. The octahedral subsurface site, which sits directly beneath the FCC hollow surface site, was the favored adsorption site in the subsurface, with an adsorption energy of 2.9 eV at the same coverage. They also calculated

a 0.9-eV activation energy for oxygen to diffuse from the surface FCC hollow site to the octahedral subsurface site. Their work shows surface adsorption is favored over adsorption in the near-surface region at low coverages; however, this trend changed as they increased coverage, with subsurface adsorption being favored over surface adsorption by 0.7 eV at a 1.0 ML coverage. Investigations of AO adsorption on Ag(110) have been limited to low coverages, finding the fourfold hollow site to be favored with an adsorption energy of 3.9 eV, very similar to that at the FCC hollow site on Ag(111).[42] Other investigations have noted the presence of subsurface oxygen on this surface, as well, with Backx *et al.* observing its coexistence with surface oxygen at reaction temperatures.[45,46] Zhu *et al.* investigated the relative stability of surface and subsurface atomic oxygen on several faces of silver, including Ag(110).[47] They found only one stable subsurface site on this facet with an adsorption energy 0.7 eV less than surface adsorption at the fourfold hollow site. No current work has investigated adsorption of AO on the surface and in the subsurface at higher coverages.

Many advances in the understanding of silver surface reconstructions and the mechanism of ethylene epoxidation have occurred over the last several decades. However, to date, few investigations have sought to explain what initiates surface reconstruction, including what role subsurface oxygen may play. Chapter 2 seeks to provide new insight into this question using classical molecular dynamics simulations, while Chapter 3 addresses the same question using quantum-mechanical DFT. Chapter 3 also seeks to develop an adsorption model based on the occupation of nearest-neighbor sites to describe AO adsorption on an unreconstructed Ag(111) surface. Chapter 4 gives a brief comparison between the difference in AO interaction with Ag(111) and Ag(110).

1.1.2 Homogeneous catalytic aziridination using organometallic complexes

Due to their many uses, an efficient synthetic route to aziridines has been the focus of much work in the literature.[48–51] The uncatalyzed aziridination reaction involves directly adding a nitrogen-containing compound to the C=C double bound of an alkene to form the desired three-membered ring. This is the so-called "C_2+N_1" reaction as the two

carbons come from one species while the nitrogen comes from another. In recent years, the use of organometallic catalysts utilizing 3d and 4d metals such as chromium,[52] iron,[53–59] manganese,[60] cobalt,[61–67] copper,[68–70] ruthenium,[71–75] and rhodium[76] has led to great advances in the synthesis of aziridines. Many of these catalysts are limited to protected azides such as (p-toluenesulfonyl)iminophenyliodinane (PhI=NTs),[53–55,60,68,70,71] arylsulfonyl azides,[62,65,72,73] or diphenylphosphoryl azide (DPPA)[61,63,67] and alkenes such as styrene.[53,60–63,74] While the synthetic steps required to remove these protecting groups are often known and relatively simple, they decrease the atom economy of the reaction: additional reagents are required to remove the protecting group, and waste is produced. Over the last decade, advances in catalyst development have allowed for the use of organic azides as the nitrogen source, reducing the number of steps needed to obtain the aziridine and limiting waste to only environmentally-friendly N_2.

Cenini and co-workers developed ruthenium-porphyrin complexes that were found to efficiently catalyze the reaction of *p*-nitrophenyl azide and α-methyl styrene.[74] All complexes contained the same porphyrin backbone but differed in the wing groups decorating the macrocycle. Regardless of the porphyrin-substituent used, the catalyst showed selectivity greater than 85% for the desired aziridine product. While it was known that such transition-metal complexes are efficient catalysts for aziridination, the mechanism of olefin aziridination was not yet well understood. Zardi *et al.* performed DFT calculations to investigate the mechanism of aziridination by these ruthenium-porphyrin catalysts.[77] They considered four possible pathways through which the reaction could proceed: organic insertion, a concerted mechanism containing an azametallacyclobutane intermediate, a step-wise radical reaction, and a stepwise carbocation reaction. They found the ruthenium catalyst proceeds through a step-wise radical reaction which barrierlessly forms a bound aziridine once the radical intermediate is formed. An additional 11.3 kcal/mol of energy is needed to dissociate the aziridine-catalyst bond to give the free aziridine. A similar computational investigation was performed by Hopmann and Ghosh to elucidate the aziridination mechanism of a cobalt-porphyrin system.[64] Similarly to Zardi *et al.*,[77] they found the reaction proceeded through a radical intermediate which barierlessly formed aziridine. Unlike the ruthenium complex, no bound aziridine was found for the cobalt complex.

The first catalyst developed that could catalyze aziridination reactions using a wide variety of alkenes, including alkyl alkenes, with organic azides was synthesized by Cramer and Jenkins in 2011.[56] $[(^{Me,Et}TC^{Ph})Fe(NCCH_3)_2](PF_6)_2$ was found to catalyze aziridination at moderate to high yields for 1-decene, *cis*-cyclooctene, *trans*-4-octene, 1-methyl-cyclohexene, and 2,3-dimethyl,-2-butene using methyl azide. The iron(II)-tetracarbene catalyst could be easily recovered due to its insolubility in the reaction mixture at room temperature and reused up to three additional times. As mentioned previously, the use of organic azides in such reactions has long been a goal as it improves the atom economy by eliminating the need for additional reactions to remove protecting groups from the aziridine; however, this iron(II)-tetracarbene catalyst required a large excess of alkene to obtain the best yield. While Cramer and Jenkins confirmed their reaction proceeded through an iron(IV) imide species, they later showed a second equivalent of azide could react with the imide to form a metallotetrazene, $[(^{Me,Et}TC^{Ph})Fe((p\text{-tolyl})N_4(p\text{-tolyl}))](PF_6)_2$.[78] The catalyst could be recovered by heating the tetrazene to 85 °C. Unfortunately, this process also gave off a second product, 4,4'-dimethylazobenzene. This reduced the yield of the desired aziridine product when the aziridination reaction was run at a high enough temperature to overcome tetrazene formation. A simple structural modification of $[(^{Me,Et}TC^{Ph})Fe(NCCH_3)_2]$ $(PF_6)_2$ which replaced the Fe(II)-center with a Cr(III) atom and coaxial acetonitrile ligands with chlorides led to aziridination with protic alkenes in the absence of high alkene loading.[52] Computational studies revealed this enhanced reactivity was a result of the *trans* chloride that remains bound in the imide. While the *trans* chloride does not effect the stability of the imide intermediate, the metallotetrazene is significantly destabilized by its presence ($\Delta G = -33.8$ kcal/mol versus -72.9 kcal/mol).

In an attempt to improve upon their previous work, Jenkins and co-workers developed a new generation of the $[(^{Me,Et}TC^{Ph})Fe(NCCH_3)_2](PF_6)_2$ catalyst which replaced the methyl bridges of the macrocycle with dimethyl boranes and removed the phenyl groups from the carbenes.[58] This new catalyst, $[(^{BMe_2,Et}TC^{H})Fe]$, showed reactivity with both alkyl azides and aliphatic alkenes. It was hypothesized the increased reactivity was a result of electronic-structure changes caused by placing the electron-withdrawing borons in the macrocycle. This advancement greatly broadened the class of reactants available to transition-metal catalyzed

C_2+N_1 aziridination. However, this catalyst still faces issues with atom economy, requiring large excess of alkene.

Computational investigations can give great insight into the observed differences in reactivity between the two structurally-different generations of iron tetracarbene catalysts developed by the Jenkins group. Additionally, the mechanism of aziridination and subsequent consequences on stereochemical retention can be determined and compared to experimental observations. Chapter 5 details such an investigation using DFT which compares the calculated mechanism with the iron-tetracarbene catalysts to porphyrin systems investigated by Zardi *et al.* and Hopmann and Ghosh.[64,77] To investigate improved atom economy and stereochemical control of the aziridine product, this work was extended to chiral variations of the second-generation catalyst in Chapter 6.

1.2 Conclusion

Structural modifications of catalysts can have significant impacts on reactivity. This dissertation investigates the effect of oxygen adsorption on two faces of silver surfaces, as well as the effect of changes in the macrocyclic-backbone of iron-tetracarbene catalysts. Chapter 7 summarizes the contributions to the field of epoxidation and aziridination made by the work in this dissertation, as well as outlines how this work can be used as a foundation to further our understanding of these systems through additional research.

Chapter 2

Classical dynamics simulations of the interaction of atomic oxygen with Ag(111) and Ag(110) surfaces

2.1 Disclosure

The following chapter has been taken, with permission, from a journal article published in *Molecular Simulation* with mostly minor modifications.[79] As detailed in Section 2.3.3, the calculations were performed as part of a course assignment. All students who performed calculations have been explicitly recognized in the acknowledgements of the journal article. Under the guidance of David Keffer and Sharani Roy, Sara Isbill organized and analyzed the results from the simulations and made major contributions to the writing of the manuscript.

2.2 Introduction

While transition metals are commonly used to catalyze the oxidation of small organic compounds, the mechanisms of these reactions are not well understood. An oxidation reaction on metal surfaces that has been deeply studied at the fundamental level using both experiment and theory is ethylene epoxidation on the silver (111) surface. While significant strides have been taken towards revealing the complex chemical pathways of these surface

reactions, several aspects of the catalysis, particularly the different ways in which oxygen interacts with the catalyst as well as with the reactants have yet to be elucidated. Even in the absence of organic reactants, an understanding of the distribution of oxygen on oxidized silver surfaces is important in developing mechanistic pathways for catalyzed reactions. This understanding is critical for designing better catalysts for this and other important reactions. In the current study we have conducted a theoretical investigation into the structure and energetics of surface and subsurface oxygen on silver.

Due to the industrial importance of this reaction, many studies have been done to better understand both the structure of the oxidized silver surface as well as the mechanism by which it catalyzes the oxidation of ethylene. Rovida *et al.*[27] were the first to propose a structure for oxygen chemisorbed on an Ag(111) surface. Using LEED, they observed a $p(4\times4)$ superstructure. The Rovida model was modified by Campbell who suggested the Ag_2O was arranged such that the topmost silver layer was between two oxide layers.[80] After the development of the STM,[24] images of the silver oxide surface could be visualized and the now Rovida-Campbell model was again slightly modified by Carlisle *et al.* who found the stoichiometric ratio of the oxide surface to be $Ag_{1.83}O$ rather than Ag_2O.[81]

Michaelides *et al.* believed these suggested models were only metastable structures at best and that another, more stable, structure for the oxidized silver surface exists.[22] Other possible Ag:O reconstructions have been reported over the past decade as the definitive structure for industrial catalysts continues to be debated.[29,30,33,34] Many of these studies have also noted the presence and potential effects of oxygen stored within the silver surface rather than just simply adsorbed to the surface.[82,83]

While several valuable studies have been done on the Ag(111) surface, much is still unknown about the behavior of surface and subsurface oxygen. In the current work we have studied oxidized silver surfaces at varying oxygen coverages and temperatures to further understand the surface structure of Ag(111) and Ag(110) catalysts.

2.3 Methods

2.3.1 Classical Molecular Dynamics Simulations

Classical molecular dynamics (MD) simulations are employed in this study in order to observe the collective effect of many O and Ag atoms beyond the scope of more accurate, but computationally more expensive, DFT calculations. Additionally, a full matrix of 153 distinct simulations were performed in which five parameters were varied, including (1) the type of surface, (111) or (110); (2) the initial location of the oxygen atoms (surface, subsurface or both surface and subsurface), (3) the initial binding site (the number of local minima depends upon choice of (1) and (2)), (4) the fractional coverage of oxygen (0.1, 0.5, and 1.0), and (5) the temperature (77 K, 300 K, and 500 K). A table showing the complete matrix of simulations is given in Table A.1 of Appendix A. This extensive suite of simulations is feasible only with the significant computational advantage of classical simulations relative to quantum mechanical calculations.

The initial configuration for each simulation was determined as follows. Bulk silver simulations were performed in the isobaric-isothermal (NpT) ensemble, in order to determine the appropriate lattice parameter for simulations at each of the three temperatures. The (111) and (110) surfaces were constructed with these lattice parameters. Oxygen atoms were placed at symmetry points corresponding to the binding sites. There are four surface sites of silver (111): top, bridge, fcc hollow, and hcp hollow. There are three subsurface sites of silver (111): tetrahedral-1, tetrahedral-3, and octahedral. There are four surface sites of silver (110): top, short bridge, long bridge, and fourfold hollow. There are four subsurface sites of silver (110): square pyramidal-1, square pyramidal-4, short subsurface bridge, and long subsurface bridge. For simulations where the oxygen fractional occupancy was less than one, the oxygen atoms were placed in the specified type of site randomly. Before simulation, a minimization (*via* the conjugate gradient method) of the oxygen, holding the Ag atoms constant was performed. This minimization proved necessary to ensure a stable initial configuration.

The ReaxFF potential was used to model all interactions in the system.[84] This potential has been shown to describe the lattice parameters of Ag (FCC) and Ag_2O (Cuprite) well. It

has been used to model Ag deposition on ZnO. To our knowledge, the potential has not been used for oxidized silver surfaces. However, there is, at the present time, no other classical potential remotely capable of describing this system. Embedded atom method potentials can routinely describe metals.[85] Buckingham potentials routinely describe metal oxides.[86] While some potentials for the classical simulation of both the metal and metal oxides exist, for example Cu/Cu_2O,[87] Si/SiO_2,[88] and Cu/SiO_2,[89] this remains a need for the modeling community.

The simulations were performed in Large-scale Atomic/Molecular Massively Parallel Simulator (LAMMPS).[90] Periodic boundary conditions were employed in all dimensions, including those parallel to the surface (x and y). The dimension of the simulation box in the z dimension was set to an arbitrarily large value (100 Å beyond the surface) to prevent interaction between images. The simulations were performed in the canonical (NVT) ensemble and the velocity Verlet algorithm was used to integrate the equations of motion with a time step of 0.125 fs.[91,92] The Nosé-Hoover thermostat controlled the temperature with a characteristic damping period of 12.5 fs.[91,93] The point charge associated with each atom was recalculated at every time step, allowing for dynamic charge evolution. For each simulation, 80,000 steps were taken resulting in simulations of 10 ps each. Significant equilibration was observed only during the first ps.

The size of the simulation box was chosen to minimize system size effects. The dimensions parallel to the surface vary between the (111) and (110) surfaces and as a function of temperature (which changes the lattice parameter). In every case, the dimension of the simulation box in the x and y dimension fell between 41.3 Å and 48.0 Å. The thickness of the Ag slab was set to at least 40 Å so that there was no direct or indirect interaction between the two surfaces. In all simulations the positions of Ag atoms in the unit cells of the bottom layer were fixed. All other Ag atoms were allowed to evolve dynamically. The number of atoms in each simulation is given in Table 2.1.

2.3.2 *Ab initio* calculations

To compare the behavior of the classical ReaxFF potential with quantum-mechanical calculations, oxygen binding energies at all of the high-symmetry sites on both the Ag(111)

Table 2.1: Number of atoms in MD simulations. Values in parentheses correspond to coverages that contain both surface and subsurface oxygen atoms.

surface	number of oxygen layers	fractional occupancy	number of Ag atoms	number of O atoms
(111)	1 (2)	0.1	4608	26 (52)
(111)	1 (2)	0.5	4608	128 (256)
(111)	1 (2)	1.0	4608	256 (512)
(110)	1 (2)	0.1	3920	14 (28)
(110)	1 (2)	0.5	3920	70 (140)
(110)	1 (2)	1.0	3920	140 (280)

and Ag(110) surfaces were calculated using DFT with the Vienna *ab initio* Simulation Package (VASP).[94,95] For the DFT calculations, it was decided that properly describing the interatomic distances of the silver atoms in the surface was presently more important than properly describing adsorption energies of O on Ag due to the interest in this work to better understand the motion of O through Ag(111) and Ag(110). Therefore, the PBEsol exchange-correlation functional[96] was used as it gave a lattice constant of 4.06 Å which is in good agreement with the experimental value of 4.09 Å.[97] The PBEsol functional was used in conjunction with the PBE projector augmented-wave (PAW) pseudopotential to describe electron-nuclear interactions.[98] Both surfaces were modeled as six-layer slabs with 72 total atoms for the (111) and (110) surfaces. A plane wave energy cut-off of 400 eV, a Monkhorst-Pack k-point grid of 5×5×1, and a vacuum layer twice the thickness of the surface slab were sufficient to give convergence with respect to energy change per atom for both the (111) and (110) surfaces.[99] Methfessel-Paxton smearing was used with a smearing width, σ, of 0.2 eV which gave an entropy change less than 0.01 meV/atom.[100] To model adsorption, atoms in the top three layers of each surface were relaxed until the forces felt by all atoms in those layers were less than 0.01 eV/Å.

2.3.3 Distributed work flow model

The matrix of 153 simulations were performed by 26 graduate students enrolled in a graduate-level course entitled "Modeling & Simulation in Materials Science & Engineering: Classical

Mechanics" (MSE 614) at the University of Tennessee, Knoxville in the spring semester of 2016. Each student was assigned a 3×3 sub-grid of simulations involving a matrix of three fractional occupancies (0.1, 0.5, and 1.0) and three temperatures (77 K, 300 K, and 500 K). The other parameters, type of Ag surface, and the location and binding site of oxygen, varied between students.

In a distributed work flow task, there should be some measure of quality assurance, in this case, sufficient to meet the standards of peer review. This is especially true in a course in which the familiarity of the students with classical MD varied greatly and included some students with little previous experience with MD simulation (although perhaps a third had familiarity with DFT calculations). Two measures of quality assurance were implemented. First, since 234 (26 students×9 simulations/student) simulations were run and the complete matrix contained only 153 unique simulations, the majority of the simulations were run twice by two different students, allowing for head-to-head comparison of the results. Second, and perhaps more importantly, David Keffer and Sara Isbill wrote a program ahead of time to generate 153 LAMMPS input files and the corresponding 153 initial configuration files. While the overhead involved in writing this code was not negligible, it resulted in a process in which none of the simulations had to be discarded under the suspicion of user error. The role of each student was to perform the simulations and to analyze the dependence of the structure, energetics, and dynamics on the temperature and fractional occupancy present in their 3×3 sub-grid of simulations.

2.4 Results and discussion

The results and discussion section is organized into three parts. In the first section, we discuss results from simulation of the bulk Ag and unoxidized Ag surfaces, which produced lattice parameters and surface energies as a function of temperature. In the second section, we introduce oxygen into the system and compare binding energies of oxygen at specific sites between ReaxFF and DFT. This provides a validation of the classical potential. In the third section, we report on the structure and energetics apparent from the suite of 153 simulations of the various oxidized surfaces.

2.4.1 Bulk Ag lattice parameters and unoxidized surface energies

via minimization, we obtained the same lattice parameter (4.216 Å) and cohesive energy (−3.04 eV) of bulk Ag at 0 K using the ReaxFF potential as Lloyd *et al.*[84] *via* simulation in the NpT ensemble, the bulk Ag lattice constants at 77 K, 300 K, and 500 K were found to be 4.220 Å, 4.233 Å, and 4.246 Å, respectively. While the calculated lattice constants are slightly larger than the experimental value of 4.09 Å at room temperature,[97] they correspond to a calculated thermal expansion coefficient of approximately 1.40×10^{-5} K^{-1} which agrees reasonably well with the experimental value of 1.89×10^{-5} K^{-1}.[97] As another measure of comparison between simulation and experiment, a first-order finite difference approximation, (E(500 K)-E(77 K)) / (500-77), between the simulations of bulk Ag at 500 K and 77 K returns a heat capacity of 0.237 $Jg^{-1}K^{-1}$, which is within 1% of the experimental value at 293 K (0.235 $Jg^{-1}K^{-1}$).

Simulations of the (111) and (110) Ag surfaces were also performed in the absence of any oxidation at 77 K, 300 K, and 500 K. These simulations allow surface energies and binding energies to be calculated. They were performed in the NVT ensemble under the same conditions as the oxidized surfaces described in Section 2.3.1. In order to calculate the surface energy, we have to account for the fact that in our simulations, we have one free surface (at the top) and one rigid surface (at the bottom), which have different surface energies. We are only interested in the energy of the free surface. In order to account for the rigid surface, which is essentially an artifact of the simulation, we perform six additional simulations (of the (111) and (110) surfaces at each of the three temperatures) in which both surfaces are held rigid. From these simulations, the surface energy of the rigid surface, $E_{surf,rigid}$, is given by

$$E_{surf,rigid} = \frac{1}{2}\frac{\left(E_{2rigid} - \frac{N_{2rigid}}{N_{bulk}}E_{bulk}\right)}{A_{2rigid}} \tag{2.1}$$

where E_i, N_i, and A_i correspond to the potential energy, number of atoms, and surface area of simulation i, where i corresponds either to the bulk simulation or the simulation with 2 rigid surfaces. From simulations with one free and one rigid surface, the surface energy of the free surface, $E_{surf,free}$, is given by

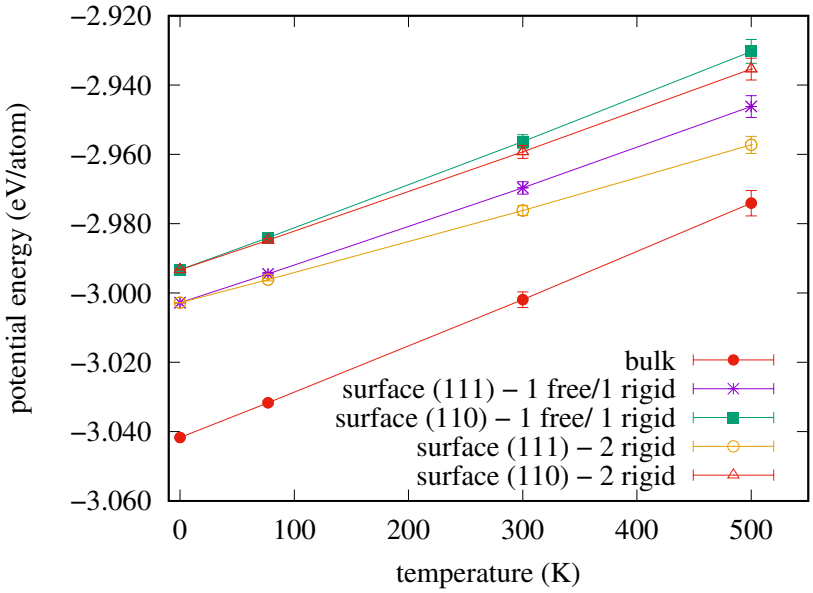


Figure 2.1: Potential energies for bulk and unoxidized surface systems.

$$E_{surf,rigid} + E_{surf,free} = \frac{\left(E_{free/rigid} - \frac{N_{free/rigid}}{N_{bulk}} E_{bulk}\right)}{A_{free/rigid}} \tag{2.2}$$

In Figure 2.1, we plot the total potential energies of the simulations of the bulk system as well as the simulations of the unoxidized surfaces with two rigid surfaces or one free and one rigid surface as a function of temperature. For all cases, the potential energy increases with temperature, as expected, as the increased thermal motion of the atoms allows them to explore volumes with less favorable energetics far from the lattice points. One also observes that the free surface is less energetically favorable than the rigid surface for the same reason; rigid atoms are locked at the energetically favored lattice points. Based on the information presented in Figure 2.1 and equations 2.1 and 2.2, the following surface energies are reported in Table 2.2. As expected, the (111) surface is more stable than the (110) surface. The surface energy has very weak dependence with temperature. We note that this surface energy is substantially lower than experimentally derived measures of (111) Ag surface (1205 $\mathrm{mJm^{-2}}$).[101] Possible causes for this discrepancy include (1) differences between the model and the experiment (the model has defect-free, atomically perfect surfaces) and (2) limitations of the Ag potential used. Furthermore, Bonzel *et al.* noted that the surface

Table 2.2: Surface energies (mJm^{-2}) of unoxidized Ag surfaces.

Temperature (K)	(111)	(110)
0	173.8	206.1
77	173.6	205.9
300	172.5	205.4
500	172.0	205.6

free energies of crystalline metals are difficult to measure and the spread in experimental values for low-index orientations is significant.[102]

2.4.2 Adsorption energies of isolated oxygen atoms: Comparison with DFT

In this section, the intent is to perform a comparison of energetic results from ReaxFF and DFT. Because the DFT results come from geometry optimization calculations, they correspond to a temperature of 0 K. Therefore, in order to make a meaningful comparison, corresponding properties using ReaxFF are generated from minimization rather than simulation at a finite temperature. The property chosen as the point of comparison is the binding energy. For both the classical and quantum mechanical calculations, the binding energy was determined *via*

$$E_{bind} = -\frac{(E_{oxidized\ surface} - E_{Ag\ surface} - N_O E_O)}{N_O} \tag{2.3}$$

where N_O is the number of O atoms in the simulation of the oxidized surface and is the energy of an isolated oxygen atom, which is zero in ReaxFF. Using this convention, a positive number indicates adsorption is exothermic (favorable) with respect to the Ag surface and O atoms far from one another while a negative number indicates adsorption is endothermic (unfavorable).

The binding energies of a single oxygen atom at each symmetry site of the Ag(111) and Ag(110) surface and subsurface were calculated with the ReaxFF potential and compared to those calculated with DFT. The results of these binding energies are given in Tables 2.3 and

Table 2.3: Results of ReaxFF and DFT calculations for adsorption energy for a single atomic oxygen bound to different binding sites on the relaxed Ag(111) surface. This corresponds to fractional coverages of 0.004 for ReaxFF and 0.08 for DFT. An asterisk (*) denotes that oxygen moved from the subsurface site closer to the surface during relaxation.

Symmetry site	ReaxFF E_{ads} (eV)	ΔE_{ReaxFF} (eV)	DFT E_{ads}	ΔE_{DFT} (eV)
fcc hollow	6.63	0.00	3.54	0.00
hcp hollow	6.70	0.07	3.44	−0.10
bridge	6.42	−0.21	3.20	−0.34
top	4.10	−2.53	1.90	−1.64
octahedral	9.20	2.57	2.83	−0.71
tetrahedral-1	7.60	−0.97	2.32	−1.22
tetrahedral-3	7.60	−0.97	2.87*	−0.67

2.4. While the dissociation energy of O_2 in the gas phase calculated with DFT is 7.06 eV (5.16 eV experimentally[103]), it is significantly lower when oxygen is adsorbed on the surface. Kunisada and Sakaguchi calculated activation barriers to molecular oxygen dissociation on Ag(111) ranging from 1.37 eV to 2.18 eV for different oxygen orientations parallel to the Ag(111) surface.[104] Roy *et al.* report a surface O_2 dissociation energy between 0.41 eV and 0.49 eV where again the values vary depending on O_2 orientation.[46]

For the Ag(111) surface it can be seen that while the adsorption energies with ReaxFF are larger than those calculated with DFT by a factor of nearly two for the surface sites and nearly three for the subsurface sites, some of the trends are consistent between the two methods. Both methods find the hollow surface sites to be favored over the bridge and top sites, though the order of preferred hollow site switches from the fcc hollow with DFT to the hcp hollow with ReaxFF. In both the classical and quantum calculations the top site was found to be much less stable than the bridge or hollows, so much so in ReaxFF the oxygen almost always moved off the top site to either the hcp hollow or fcc hollow during relaxation, as shown in Figure A.1 in Appendix A for the 0.1 fractional coverage simulation at 77 K. ReaxFF also over stabilizes the subsurface sites at low coverages. Li, Stampfl, and Scheffler have computationally shown with DFT that adsorption energies on surface sites decrease at a much faster rate with coverage than subsurface sites, leading to a flip in preferred binding from surface to subsurface at approximately 0.50 ML coverage.[43,44] While ReaxFF does not

Table 2.4: Results of ReaxFF and DFT calculations for adsorption energy for a single atomic oxygen bound to different binding sites on the relaxed Ag(110) surface. This corresponds to fractional coverages of 0.007 for ReaxFF and 0.08 for DFT. An asterisk (*) denotes that oxygen moved from the subsurface site closer to the surface during relaxation.

Symmetry site	ReaxFF E_{ads} (eV)	ΔE_{ReaxFF} (eV)	DFT E_{ads}	ΔE_{DFT} (eV)
fourfold hollow	8.16	0.00	4.14	0.00
long bridge	5.66	−2.50	4.07	−0.07
short bridge	5.57	−2.59	3.72	−0.42
top	5.32	−2.84	2.66	−1.48
square pyramidal-1	8.19	−0.03	2.65	−1.49
square pyramidal-4	8.16*	0.00	4.14*	0.00
long subsurface bridge	9.22	1.06	3.42	−0.72
short subsurface bridge	7.77	−0.39	2.29	−1.85

capture this rather difficult preference switch, it can be used to make predictions of the surface behavior at higher oxygen coverages.

For the Ag(110) surface, binding energy trends for surface sites are equivalent between ReaxFF and DFT. Both find the hollow to be the most favorable binding site for AO and the top site to be the least favorable, though the binding energies differ as was seen for the (111) surface. The surface binding trends observed here are supported by the work done by Rawal *et al.*[42] The trends for subsurface binding between the two computational techniques are quite different. While both ReaxFF and DFT find the short subsurface bridge site to be the least favored, they show different trends for the other subsurface sites. As with the (111) surface, the subsurface binding sites are slightly over stabilized compared to DFT. To our knowledge an extensive study of AO binding in the (110) subsurface in not yet available in the literature to compare possible switches between surface and subsurface binding with coverage as has been done for the (111) surface.

2.4.3 Simulation of oxidized Ag surfaces

In this section, we present and discuss the results of the simulations of the oxidized Ag surfaces. We organize this work into four subsections: surface O on the (111) surface,

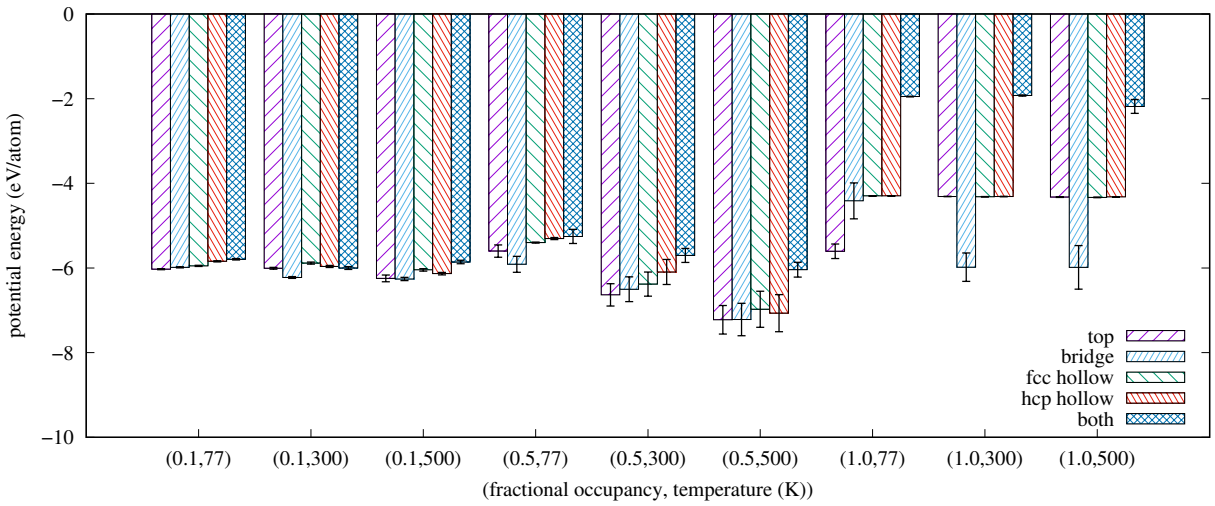


Figure 2.2: Time-averaged potential energy of oxygen as a function of temperature and coverage for the four different initial oxygen sites on the Ag(111) surface.

subsurface O on the (111) surface, surface O on the (110) surface, and subsurface O on the (110) surface.

Surface oxygen on the Ag(111) surface

In this subsection, we discuss five sets of simulations, in which each set contains a 3×3 matrix of fractional occupancies and temperature. The difference between the simulations is the initial position of the oxygen atoms. In four of the sets, there is only a surface layer and the O atoms are placed at the top, bridge, fcc hollow, and hcp hollow sites. In the last set, there are both surface and subsurface layers, with the surface O occupying fcc hollow sites and the subsurface O occupying octahedral sites. Again, for simulations where O atoms were initially placed at the top site, most O atoms moved to hcp hollow sites with the rest moving to fcc hollow sites during the relaxation prior to the simulation. O atoms placed at all other (111) surface sites were still in their respective sites at the start of the simulation.

With the ReaxFF interaction potential it is possible to associate a potential energy with each atom. It is therefore possible to obtain the ensemble-average potential energy of an oxygen atom by averaging the potential energy of each individual O atom over all atoms of O as well as over time during the course of the simulation. This average potential energy of

an O atom is plotted in Figure 2.2. Simulations are grouped as elements of the 3×3 grid of temperature (77 K, 300 K, and 500 K) and fractional occupancy (0.1, 0.5, and 1.0).

Within a group of simulations at common temperature and fractional occupancy, the only difference is initial position of the oxygen atoms. If the O atoms possess sufficient energy to overcome diffusion barriers separating sites, then all simulations in this group will sample the same distribution of sites and a common potential energy will be generated. To the extent that this is not the case, then, at least during the time span of the simulation, the O atoms were not able to sample sites freely and erase the memory of their initial placement. Intuitively, one might expect that temperature plays a key role in this redistribution. At low temperatures, the O atoms lack sufficient kinetic energy to move from the local minima in potential energy presented by their initial site, while at high temperature, they are free to do so. In fact, Figure 2.2, shows a more complicated trend controlling O placement on the Ag(111) surface. It is fractional occupancy, rather than temperature that seems to play a critical role in this process of O redistribution and relaxation. At low fractional occupancy, the difference between average O potential energy from similar simulations, differing only in initial placement of O, exceeds the standard deviation at all temperatures. Whereas, at high fractional occupancy, the difference between simulations at a common temperature is negligible (with one exception, which shall be explained later). At intermediate loading there is a different behavior, characterized by much larger standard deviations in the potential energy. One reason for the differences in potential energy is the random placement of O atoms on the surface at the 0.1 and 0.5 fractional coverages. The combined effect of initial configuration and amount of surface to subsurface movement of O atoms, which will be discussed more in the following paragraph, could lead to the observed deviations.

In Figure 2.2, we can also observe the temperature dependence of the potential energy at varying fractional occupancies. Intuitively, we expect the potential energy of the entire system to rise with increasing temperature. Here, where we inspect only the O atoms, we find very weak temperature dependence in the potential energy of the O atoms at low fractional occupancy and at high fractional occupancy. However, at a fractional occupancy of 0.5, we observe the counter-intuitive behavior of a large decrease in the potential energy (it becomes larger in magnitude and more negative) with increasing temperature. This behavior

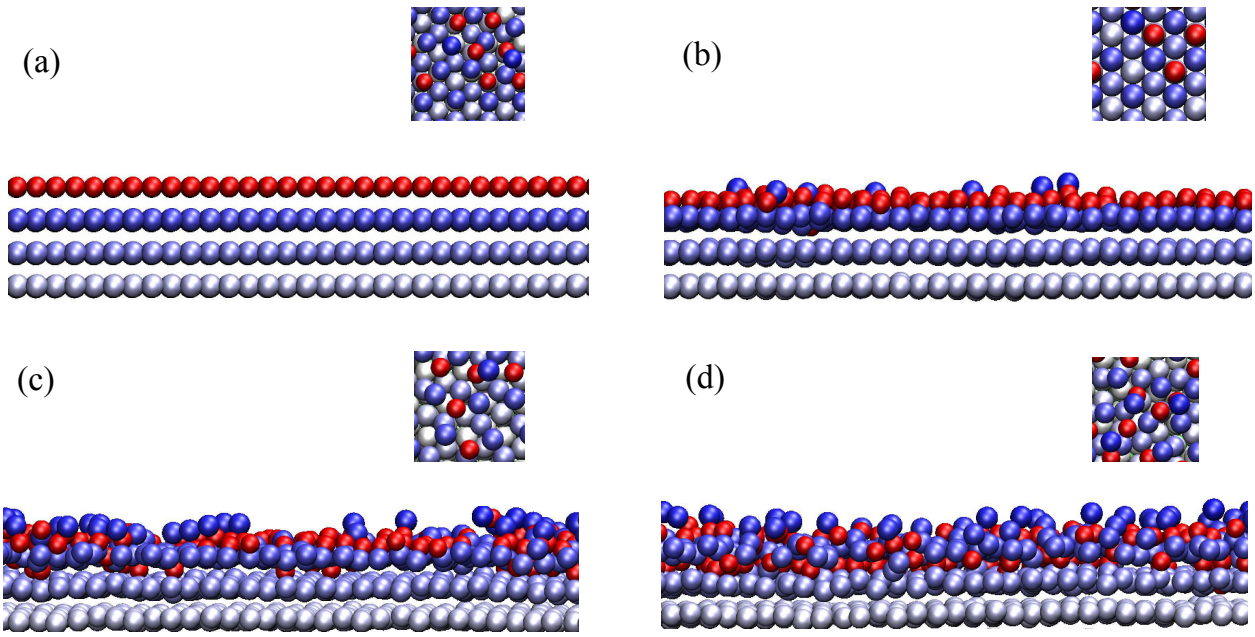


Figure 2.3: Snapshots of the initial configuration (a) and the final configuration of the 0.5 fractional occupancy at 77 K (b), 300 K (c) and 500 K (d) for O atoms initially placed at the fcc hollow surface sites of the Ag(111) surface. O atoms are shown in red and the Ag atoms shown in blue are darkest near the surface and become lighter as they move toward bulk.

is due to relocation of the O atoms from the surface sites to more favorable subsurface sites. This can be seen in movies and snapshots of the simulations. See for example Figure 2.3. In fact, we note that, for the systems that follow, a decrease in the potential energy of O with increasing temperature is a signature of redistribution of O and the accompanying highly disordered reconstruction of the surface. In Figure 2.3, at a fractional occupancy of 0.5, as the temperature increases more O atoms are able to migrate to the subsurface location. For the cases where O atoms begin at a hollow site this reconstruction was caused by Ag atoms moving above the O surface layer; whereas, when O atoms begin at bridge sites reconstruction was initiated by O atoms moving into the subsurface. We also note that this redistribution results in a more disordered surface, characterized by larger error bars (one standard deviation each) in the O potential energy. This redistribution of O has a critical fractional occupancy. At low fractional occupancies, it does not occur. At a fractional occupancy of 1.0, it again does not occur for nearly all cases. A full monolayer of O stabilizes the oxide surface layer for all but the bridge case. Whether this metastable

full surface oxide monolayer is experimentally achievable is unknown; if the deposition of O is slower than the movement to subsurface sites, a full monolayer at the surface would likely not form. In the simulation, of course, it was specified in the initial condition. Three anomalous points were observed where at least one surface O atom moved to the subsurface in the absence of reconstruction at fractional coverages of 0.1 or 1.0. One occurred at a fractional occupancy of 1.0 and a temperature of 77 K, where the O atoms began at the top site, resulted because a single O atom, as it moved from the unfavorable top site, was able to migrate to a subsurface site. The other anomalous points were for O atoms placed in the hcp hollow sites of a fractional coverage of 0.1 and temperature of 300 K and 500K. Surface reconstruction was seen to occur when O atoms were initially placed at the bridge site even at a full coverage of oxygen. Placing one O atom in a bridge site per surface Ag atom fills only half of the available bridge sites, allowing O atoms to move from their initial site, prompting surface reconstruction without moving close enough to repel one another.

We also note in Figure 2.2 based on the data series, in which both a surface and subsurface layer of oxygen are present, that the presence of the subsurface layer weakens the binding of the surface layer. The effect of this weakening increases with increasing fractional occupancy of O. The corresponding potential energies for subsurface O from these same simulations is presented in the next section.

Based on the reported cohesive energies of bulk Ag, AgO, and Ag_2O calculated using both DFT and ReaxFF,[84] it is clear that at 0 K the bulk metal oxides are more stable than the bulk metal. Even at finite temperature, movement of oxygen to subsurface sites is consistent with the greater thermodynamic stability of the oxide, especially at higher oxygen chemical potentials. Of course, the observed kinetics of the system toward this state is a function of temperature, surface structure, and fractional occupancy of oxygen.

While electronic properties are generally not available in classical simulations, with the ReaxFF potential, we have allowed the charge to dynamically evolve in time. Thus we have at least a measure of the extent of charge transfer based on the point charge associated with each atom. In Figure A.2 in Appendix A, we present a plot for the average O charge (averaged over all O atoms and over simulation time) analogous to that for the potential energy shown in Figure 2.2. Struck by the qualitative similarity of the two plots, we plotted

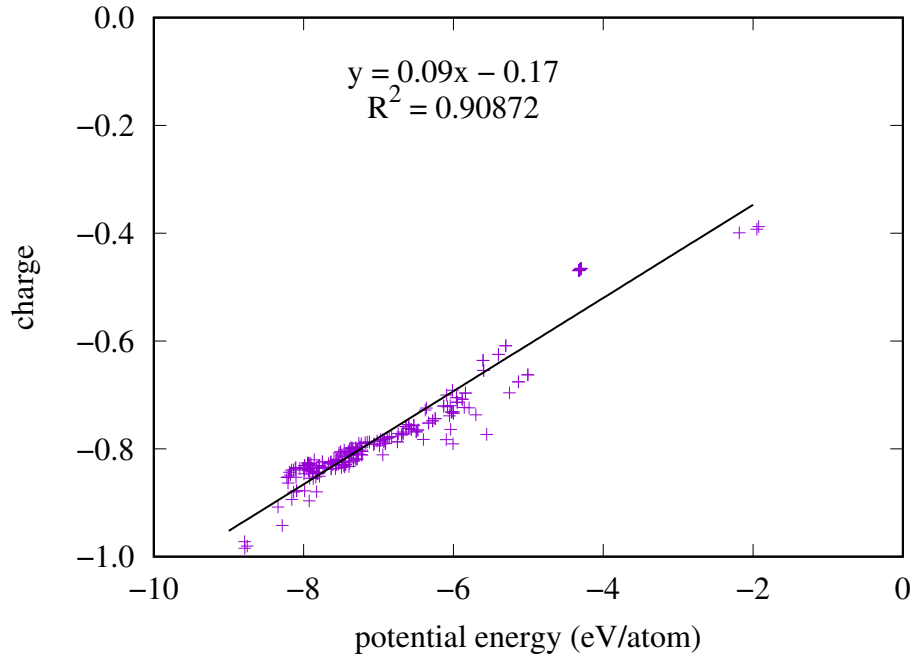


Figure 2.4: Plot of oxygen potential energy against charge shows a clear correlation between the two properties.

average O charge vs average O potential energy for all 153 simulations (not just the (111) surface O discussed in this subsection), as shown in Figure 2.4. Here we clearly observed O charges in the range -0.4 to -1.0 e^- and note that O charge and potential energy are highly correlated. As the magnitude of the charge becomes greater, the potential energy deepens. Thus, from the point of view of the O atom, being in a local environment where charge transfer is favored strengthens the binding with the surface.

We shall show that this correlation between charge and potential energy extends also to correlation between the coordination of Ag atoms around O. Increased coordination corresponds to a lower potential energy and increases the degree of charge transfer. This seems to be a characteristic of this parameterization of the ReaxFF potential. The previously published DFT study, which indicates that, at low loadings the more highly coordinated subsurface sites are less energetically favorable relative to the less coordinated surface sites, predicts a more complicated relationship between charge transfer, binding energy and coordination than what is captured here. At the very least this observation identifies a

potential source of the direction for improvement in a subsequent parameterization of the reactive potential.

In Figure A.3 of Appendix A, we show the average potential energy of Ag atoms for simulations in which O are on the surface sites of Ag(111). Less insight is gained from these plots because most of the Ag are not surface atoms. However, we do note that, in contrast to what was observed for O in Figure 2.4, the potential energy of Ag atoms is not correlated with the charge. In fact, in Figure 2.5. we show that for all systems, the charge on the silver correlates with O fractional occupancy. In other words, the more O present on the surface, the greater the average charge transfer experienced by Ag atoms. This observation is entirely reasonable when considered from the point of view that the Ag surface is responding to the presence of O.

While snapshots can be used to provide visual evidence of the structural changes corresponding to the energetic and electronic trends in Figures 2.2 and 2.4, radial distribution functions (RDFs) provide statistically sound measures of local atomic structure. The integral of the RDF provides the cumulative coordination number (CN). For each simulation the RDF and CN for O-O, O-Ag and Ag-Ag were recorded. In this report, we present only the O-Ag RDFs and CNs, as they provide the greatest insight into the manner in which O situates itself within the Ag matrix. In an O-Ag RDF, an O sits at the origin, and the RDF describes the distribution of Ag about the O. In Figure 2.6, the O-Ag RDF and CN for a selected simulation of O in the surface sites of Ag(111) are shown. From the RDFs at a fractional occupancy of 0.5 (Fig. 2.6(a)), we observe more structure at lower temperature, as expected. However, from the integrated RDF (Fig. 2.6(b)), we observe that the coordination number increases with increasing temperature, thus explaining the seemingly counter-intuitive result shown in Figure 2.2, where the potential energy of O become more favorable with increasing temperature. As the O migrate to subsurface sites, their CN number increases, resulting in lower potential energy and greater charge transfer. From the RDFs at a temperature of 300 K (Fig. 2.6(c)), we observe one type of ordering of O at 0.1 occupancy and another order at 1.0. At an occupancy of 0.5, the O atoms are most disordered. The plot of the CN for these simulations (Fig. 2.6(d)) provides the structural confirmation of the minimum observed in the O potential energy as a function of fractional occupancy. Despite the disorder at 0.5, the

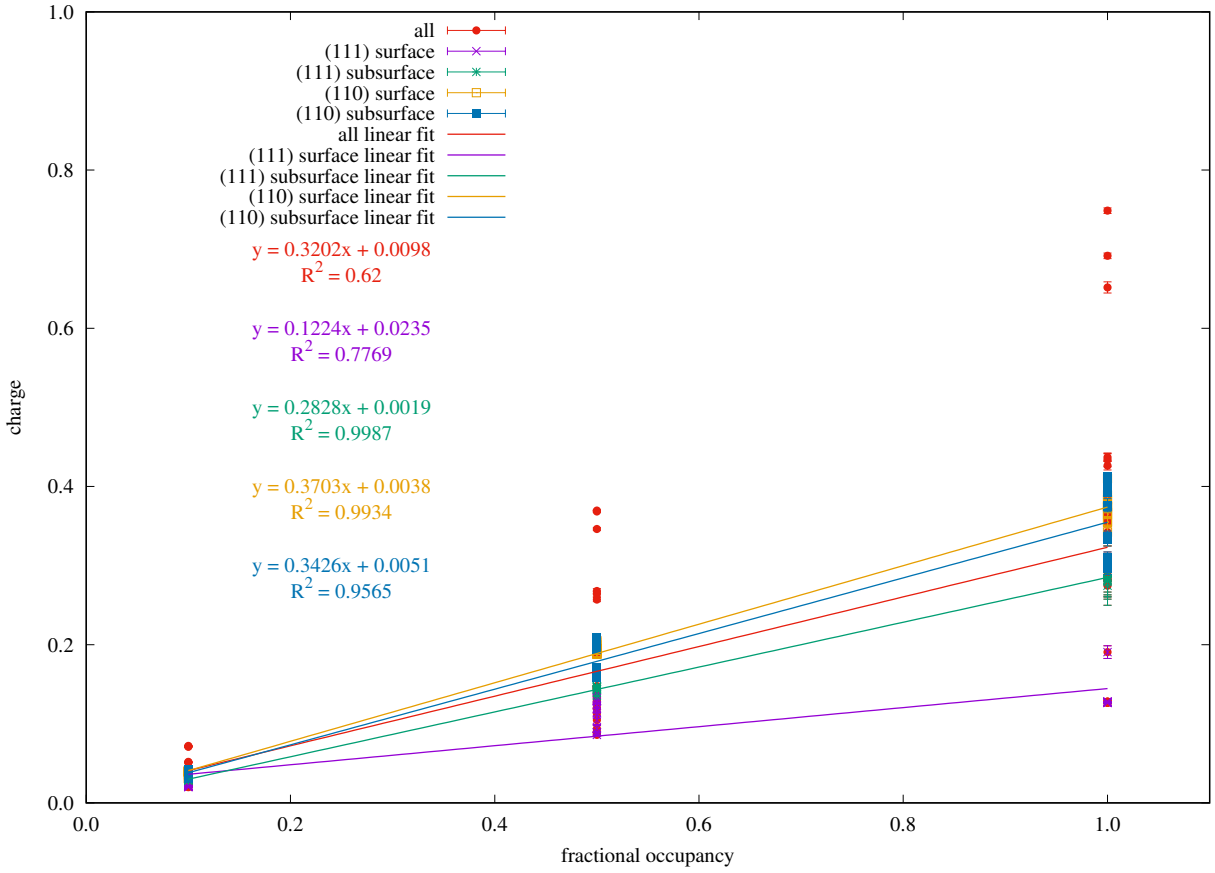


Figure 2.5: Plot of silver potential energy against fractional occupancy shows a clear correlation between the two properties.

CN of Ag around O is greatest at this intermediate fractional occupancy, especially in the short range of 2.3 to 3.7 Å, where the potential energy contributions are most significant.

The average mean square displacements (MSDs) of O and Ag atoms were also recorded for all simulations. They are not shown as they add little insight into the discussion. All of the MSDs reach a plateau, the height of which reflects whether the O atoms remained in their initial site or redistributed to another site. The plateau itself indicates that, if redistribution of the atoms occurred, it ended early in the simulation and was followed by a period where the atoms vibrated about their selected site. These simulations, 10 ps in length, were too short to measure statistically reliable diffusion coefficients for either surface motion or penetration into the bulk.

Subsurface oxygen on the Ag(111) surface

In this subsection, we discuss four sets of simulations where, again, each set contains a 3×3 matrix of fractional occupancies and temperatures. In three of the sets, there is only subsurface oxygen which has been placed at the tetrahedral-1, tetrahedral-3 and octahedral sites. The last set is the mixed surface and subsurface coverages discussed in the previous subsection, which contains O occupying both fcc hollow sites and octahedral sites.

A similar analysis as discussed previously has been performed for subsurface O on the Ag(111) surface. Figure 2.7 shows the average potential energy of an O atom in the various subsurface sites. At all combinations of fractional occupancy and temperature, the octahedral site is found to be the most stable site. The nature of subsurface redistribution of O atoms is slightly different than that of surface O. We observe that most subsurface O remains in subsurface sites; however, we do observe for some simulations a few O atoms migrate to the surface.

Once again, fractional coverage is seen to play a critical role in surface reconstruction. Low fractional coverage leads to a rather stable surface with oxygen and silver moving to a more stable arrangement when temperatures are large enough to overcome the surface reconstruction barriers. This can be seen to happen for all but the lowest temperature case. The same reconstruction to a more stable configuration at high enough temperatures can be seen for the 0.5 fractional coverage where overall the system is slightly less stable compared to

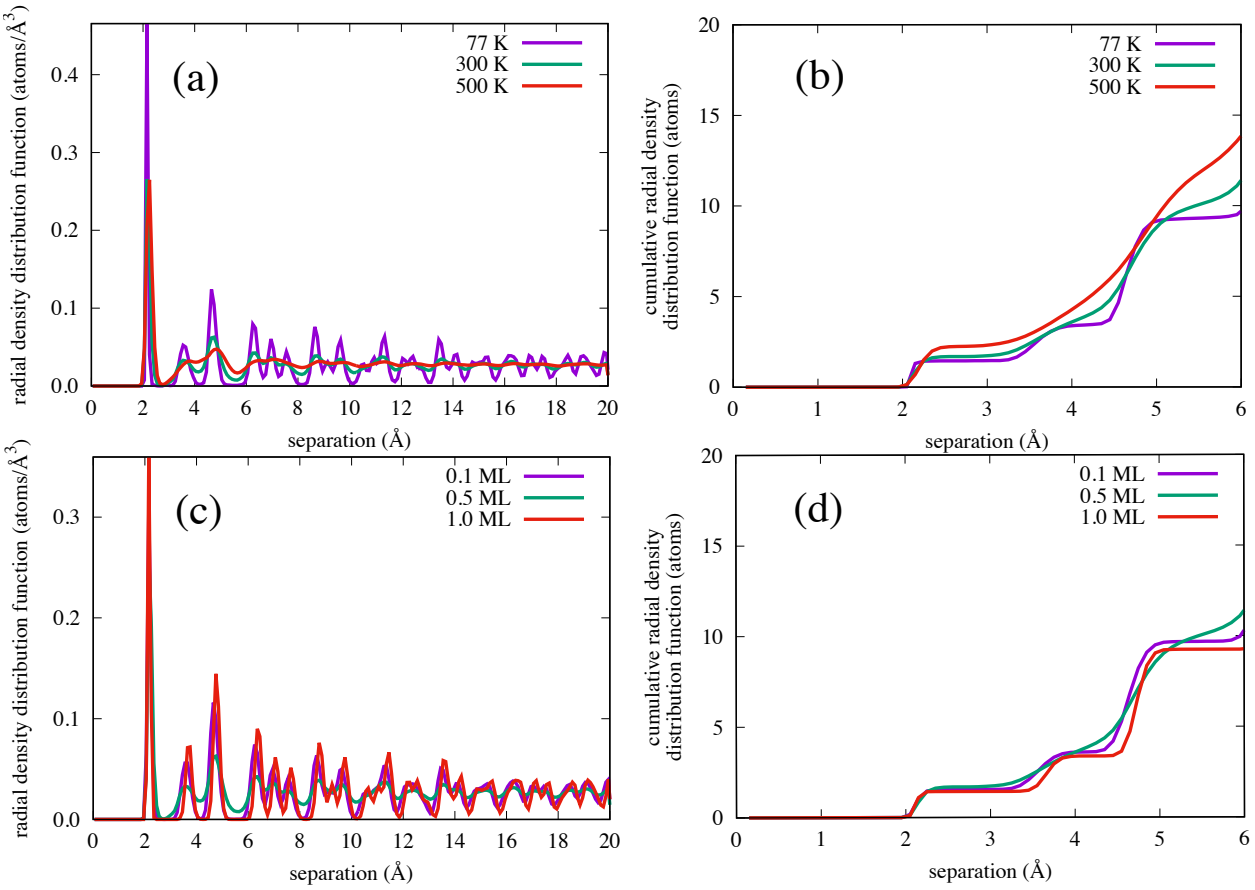


Figure 2.6: Plots of the O-Ag RDF (a) and CN (b) for an oxygen atom at the hcp hollow site with a fractional coverage of 0.5 for various temperatures and the RDF (c) and CN (d) for an oxygen atom at the hcp hollow site at a temperature of 300 K for various fractional coverages. All surfaces in this plot are Ag(111).

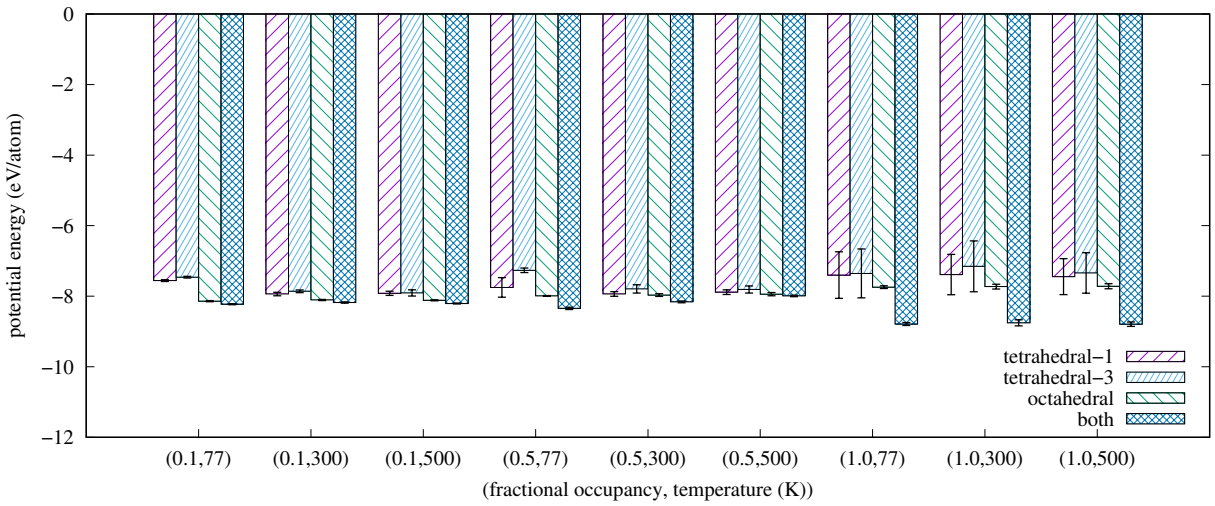


Figure 2.7: Time-averaged potential energy of subsurface oxygen atoms as a function of temperature and coverage for the three different initial oxygen subsurface sites on Ag(111).

the low coverage potential energy. Figure 2.8 shows the initial (a) and final (b) configurations observed when O atoms were initially placed in the tetrahedral-3 site with a 0.5 fractional coverage and temperature of 500 K. The potential energy of the oxygen increases further at the full fractional coverage. O atoms in the full coverage system can no longer initiate surface reconstruction due to the high symmetry of the system. The error bars for O atoms initially in tetrahedral sites at a full coverage are much larger than those for the octahedral site at a full coverage or any site at a 0.1 or 0.5 fractional coverage. This will be discussed below. From Figure 2.8 we observe the O potential energy becomes less favorable with increasing coverage. Only for the tetrahedral-3 site at the full fractional coverage does the potential energy become less negative when increasing temperature from 77 K to 300 K; however, this increase in potential energy is within the standard deviation of the tetrahedral-3 site at both temperatures.

The lower potential energy of the 0.1 and 0.5 fractional coverages can be explained by inspecting snapshots of the simulations and RDFs (Fig. 2.9). Both confirm that surface reconstruction occurs for the 0.1 and 0.5 fractional coverages when oxygen starts in one of the tetrahedral sites but it does not occur when O is initially placed in the octahedral site. As with the (111) surface, the surface reconstruction coincides with an increase in the CN of

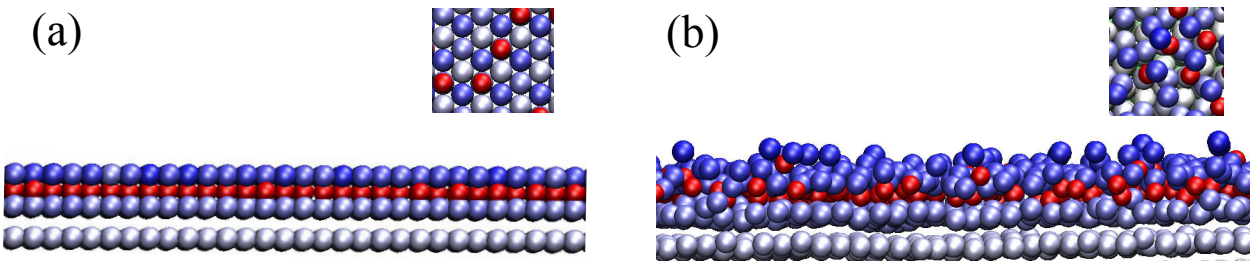


Figure 2.8: Snapshots of the initial configuration (a) and the final configuration (b) of the 0.5 fractional occupancy at 500 K for O atoms initially placed at the tetrahedral-3 subsurface sites of the Ag(111) surface. The color scheme follows that of Figure 2.3.

O. It is unknown if the lack of reconstruction at the octahedral site is a realistic observation or an artifact of the ReaxFF potential due to its over stabilization of the octahedral site.

At the full 1.0 fractional coverage, a different type of reconstruction is seen. Rather than the highly symmetric surface becoming disordered, the top two layers of silver and the layer of oxygen simultaneously shift en masse as needed so that the O atoms reside in octahedral sites. This effect is likely an unphysical consequence of starting the simulation in a highly symmetric but metastable configuration. The barrier to surface motion must be lower than the diffusion barriers between subsurface sites.

Surface oxygen on the Ag(110) surface

In this subsection, we discuss five sets of simulations where, again, each set contains a 3×3 matrix of fractional occupancies and temperatures. In four of the sets, there is only surface oxygen which has been placed initially at the top, fourfold hollow, long bridge, and short bridge sites. The last set is the mixed surface and subsurface coverages which contain O initially occupying both hollow surface sites and square pyramidal-1 subsurface sites.

As a first step to look at the behavior of surface oxygen on the (110) surface, the time-averaged potential energy of oxygen in the different surface adsorption sites has been plotted in Figure 2.10. As with the 0.5 fractional coverage of O atoms on the (111) surface (Fig. 2.2), the potential energy becomes more negative with increasing temperature for all coverages on the (110) surface. This decrease in potential energy with temperature is again due to surface reconstruction. Reconstruction increases slightly with coverage, but temperature plays the dominant role in reconstruction on the less tightly packed (110) surface. This

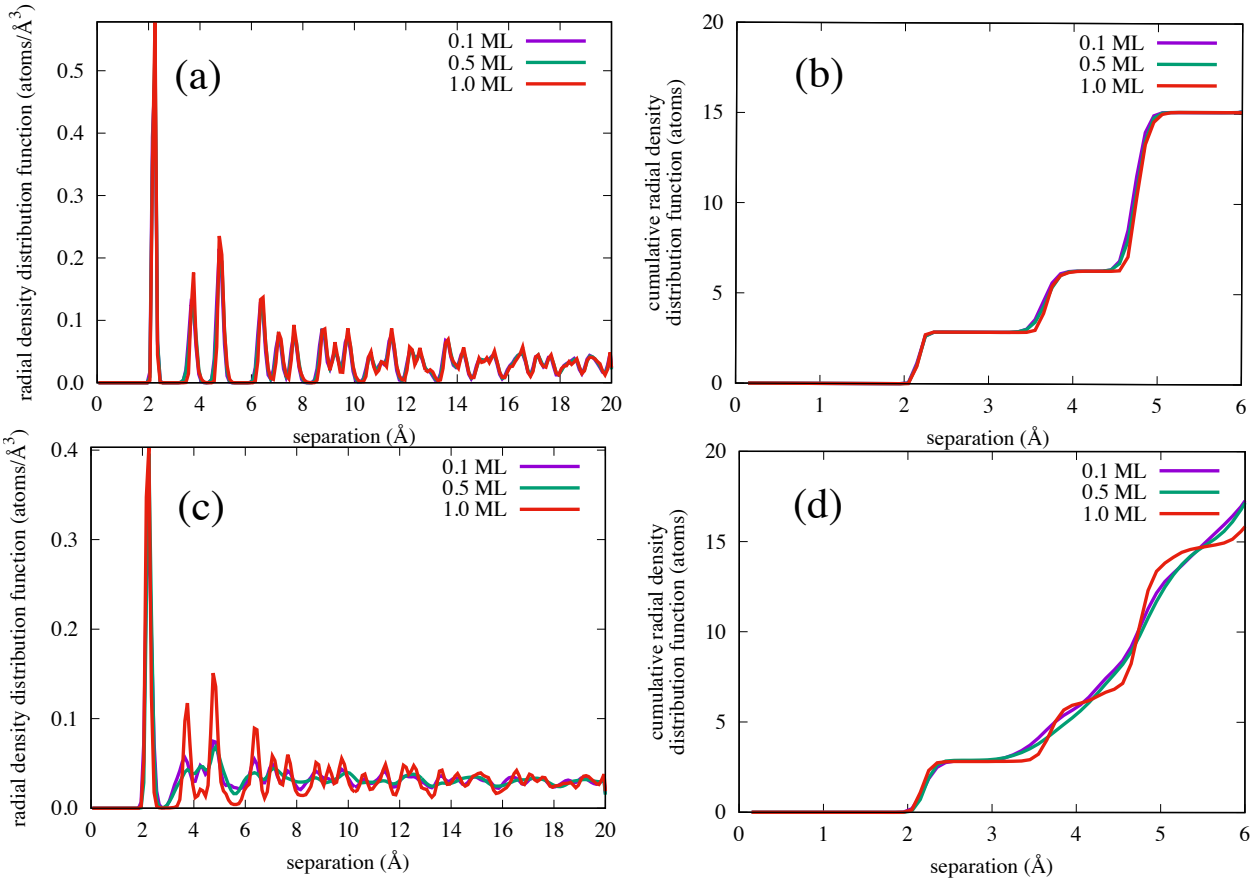


Figure 2.9: Octahedral O-Ag RDF (a) and CN (b) and tetrahedral-1 O-Ag RDF (c) and CN (d) at 300 K and various fractional coverages.

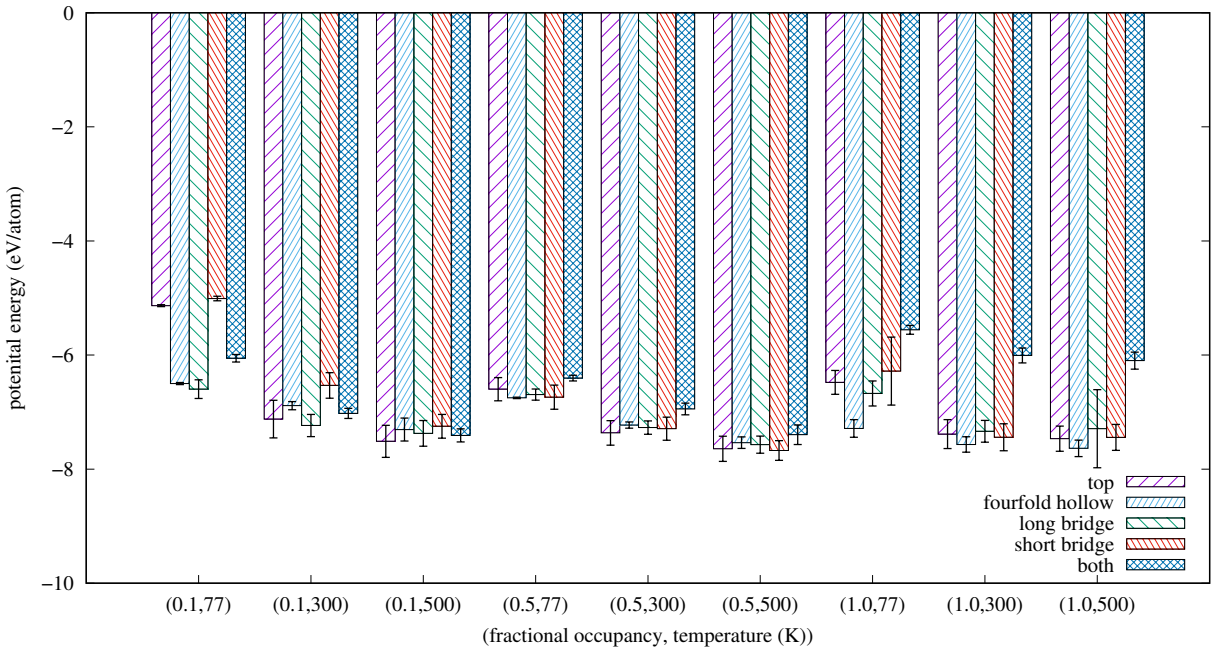


Figure 2.10: Time-averaged potential energy of surface oxygen atoms as a function of temperature and coverage for the four different initial oxygen sites on the Ag(110) surface.

can clearly be seen in Figure 2.11 which shows the initial configuration (Fig. 2.11 (a)) and final configurations at 77 K (Fig. 2.11 (b)), 300 K (Fig. 2.11 (c)), and 500 K (Fig. 2.11 (d)) for a 1.0 fractional coverage of O atoms initially placed at the fourfold hollow site. No reconstruction is observed at 77 K while slight reconstruction is observed at higher temperatures.

Watching movies of the trajectories and analyzing the RDF and CN plots confirm slight reconstruction at low temperature for most initial configurations and larger amounts at high temperature for all initial configurations. Little to no reconstruction was seen on the (111) surface at a full fractional coverage yet this coverage results in the most reconstruction when O atoms are initially placed on the (110) surface. Diffusion of O atoms to the subsurface was also observed for almost all coverages and temperatures. We believe more motion of surface O atoms to the subsurface was observed for the (110) surface due to the presence of more space between Ag atoms than in the (111) surface. Only the 0.1 fractional coverage of O atoms initially placed in the fourfold hollow site at 77 K did not result in any O atom movement to the subsurface. However, the same initial site and temperature but at a full fractional coverage resulted in all O atoms moving to the subsurface prior to reconstruction

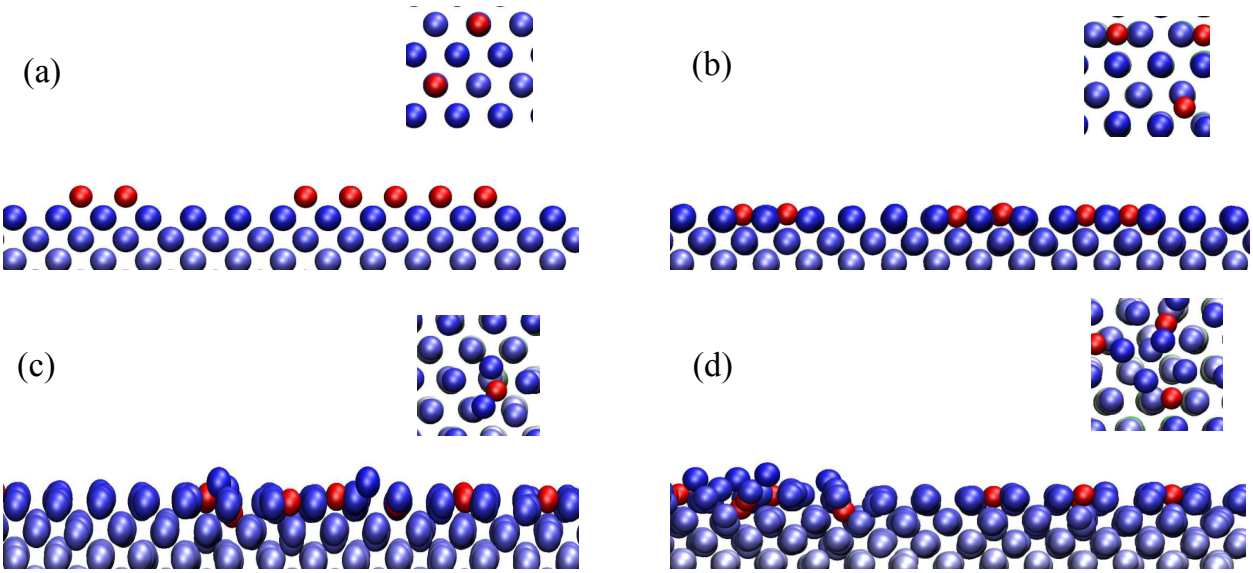


Figure 2.11: Snapshots of the initial configuration (a) and the final configuration of the 0.1 fractional occupancy at 77 K (b), 300 K (c) and 500 K (d) for O atoms initially placed at the fourfold hollow surface sites of the Ag(110) surface. The color scheme follows that of Figure 2.3.

(Fig. 2.12 and 2.13). The en masse motion of O atoms to the subsurface at the full coverage is similar to the coordinated motion of Ag and O atoms observed when O atoms were initially placed in the tetrahedral sites on the (111) surface at a fractional coverage of 1.0. This, again, is likely an unphysical consequence of starting the simulation in a highly symmetric but metastable configuration.

When oxygen is initially placed in both surface and subsurface sites, similar disorder and reconstruction as previously discussed was observed at all coverages; however, no O atom movement between surface and subsurface was observed. For the simulations of a 1.0 fractional coverage of O atoms in both the surface and subsurface, O surface atoms were seen to be shot off from the surface at high temperatures. While desorption at high temperatures is very possible, the observed O atom ejection is likely an artifact of the initial configuration.

Subsurface oxygen on the Ag(110) surface

In this subsection we discuss the final five 3×3 grids of simulations. In four of the sets, there is only subsurface oxygen which has been placed at the square pyramidal-1, square pyramidal-4, long subsurface bridge, and short subsurface bridge sites. The last set is the

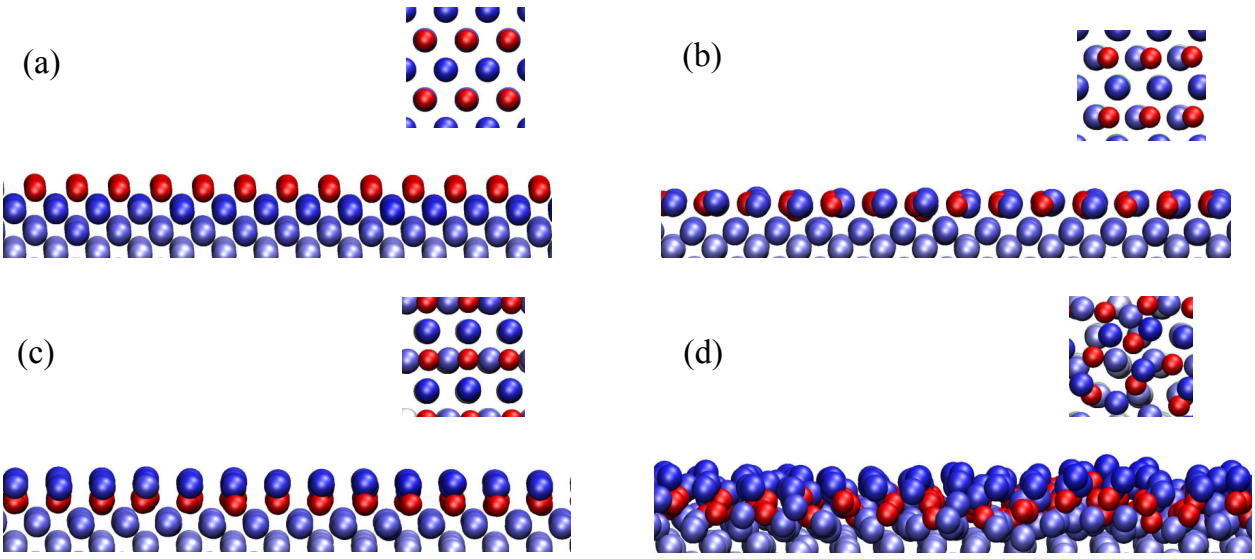


Figure 2.12: Snapshots of the initial configuration (a), the configuration at 0.138 ps (b), the configuration at 0.512 ps (c), and the final configuration (c) of the 1.0 fractional occupancy for O atoms initially placed at the fourfold hollow surface sites of the Ag(110) surface at 77 K. The color scheme follows that of Figure 2.3.

mixed surface and subsurface coverages which contain O occupying both hollow surface sites and square pyramidal-1 subsurface sites.

The time-averaged potential energy of O when oxygen atoms were initially placed in the Ag(110) subsurface sites is shown in Figure 2.14. Compared with the corresponding plots in the previous sections, fewer clear trends are immediately seen for the (110) subsurface. This is partially due to movement of most O atoms to new sites during the initial relaxation prior to the simulation beginning. For example, O atoms placed in the square pyramidal-4 site and long subsurface bridge sites moved up into surface sites and occupied combinations of hollow and bridge sites. Atoms placed in the other two sites (the square pyramidal-1 and short subsurface bridge sites) moved laterally to either a hollow or a subsurface bridge site. This movement is likely due to the artificially high binding energies at the hollow surface and subsurface bridge sites from the ReaxFF potential. Though most O atoms did not remain in their initial sites during relaxation, we still observe rich behavior. Nearly every simulation resulted in some surface disorder while the extent of this disorder and reconstruction varied greatly. This is reflected in the potential energies shown in Figure 2.14 and shown visually in Figure 2.15. Some sites see very little change in potential energy with

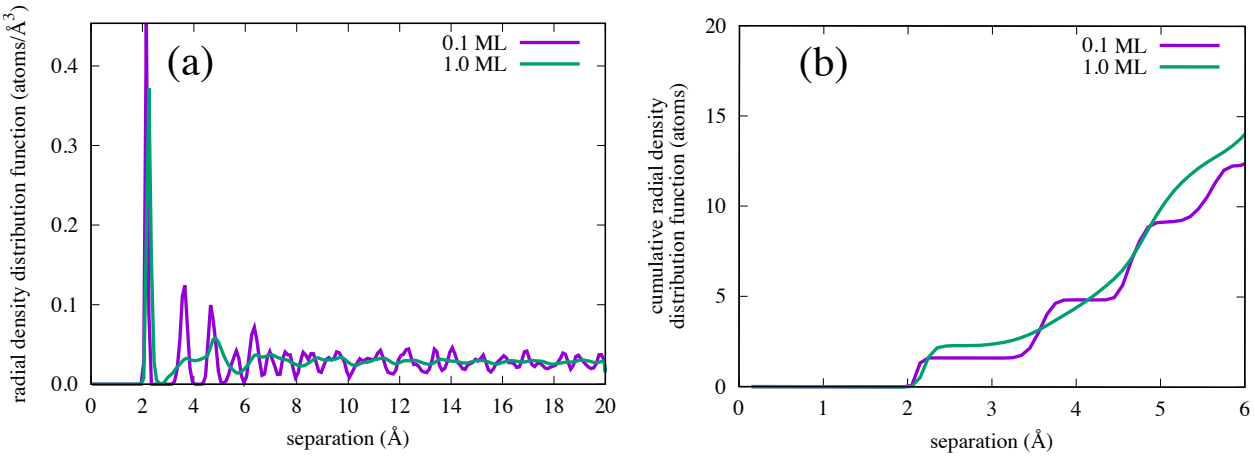


Figure 2.13: O-Ag RDF (a) and CN (b) of the O atoms initially placed in the fourfold hollow site on Ag(110) at 77 K and the two extreme coverages studied.

increasing temperature and coverage (for example square pyramidal-1) when compared with other sites (square pyramidal-4).

RDF and CN plots, as well as videos of the trajectories give more insight into the amount of reconstruction observed for the various site, temperature, and coverage combinations. For the square pyramidal-1 simulations, O atoms remain at the site they move to during the relaxation while some of the Ag atoms move from their lattice sites. For this site, disorder increased both with temperature and coverage (Fig. 2.16). Similar behavior was observed for the 0.1 and 0.5 fractional coverages for O atoms initially placed at the long subsurface bridge sites. Full loading at this site resulted in surface reconstruction that increased with temperature. Lower coverages of O placed initially in square pyramidal-4 and short subsurface bridge sites led to disorder of Ag atoms and the full coverage led to large amounts of reconstruction.

2.5 Conclusions

We have performed molecular dynamics simulations using ReaxFF on a suite of 153 simulations which sample two different surfaces of Ag with different temperatures and fractional occupancies of oxygen. The binding energy of O atoms placed at the different high-symmetry sites on both the Ag(111) and Ag(110) surface and subsurface have also been calculated with DFT to test the reliability of ReaxFF for this Ag/O system. In

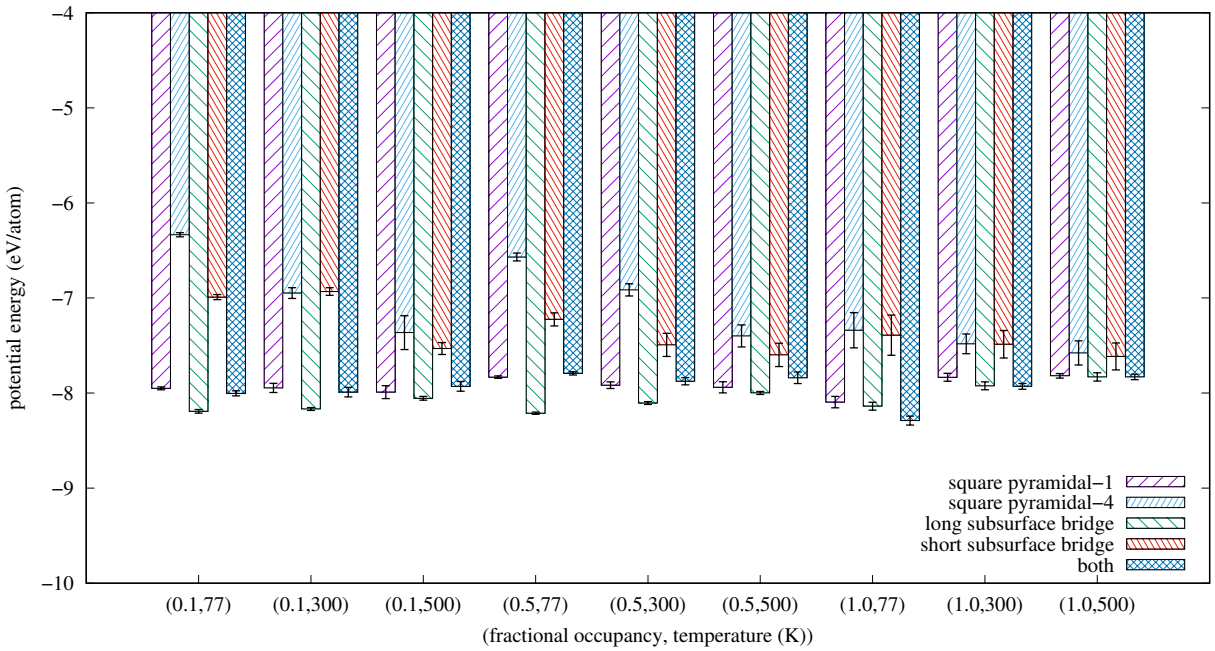


Figure 2.14: Time-averaged potential energy of subsurface oxygen atoms as a function of temperature and coverage for the four different initial oxygen sites on the Ag(110) surface.

general, ReaxFF and DFT showed qualitative agreement with one another, allowing trends in behavior to be obtained. A few thermodynamic properties of bulk Ag were calculated with ReaxFF and found to be in good agreement with the experimental values in the literature.

We have found that for many of the conditions sampled in the current study, disordered reconstruction leads to a system that is more energetically favorable than the initial configuration where Ag atoms were at their perfect lattice sites. The driving force behind this reconstruction is largely an increase in the coordination of O by Ag, resulting in a more favorable binding site. The extent of reconstruction and atomic motion that initiates the reconstructive process is highly dependent on surface type, fractional occupancy, initially occupied site, and temperature. In most cases, an increase in temperature enhances reconstruction, as is the case on Ag(110). Contrarily, on Ag(111) it is fractional coverage rather than temperature that effects reconstruction. In several cases, a full monolayer of O either prevents reconstruction entirely or leads to an alternate reconstruction than that observed at partial coverages. This effect appears to be due to a highly symmetric, but metastable initial condition. Whether this state can be reproduced experimentally remains

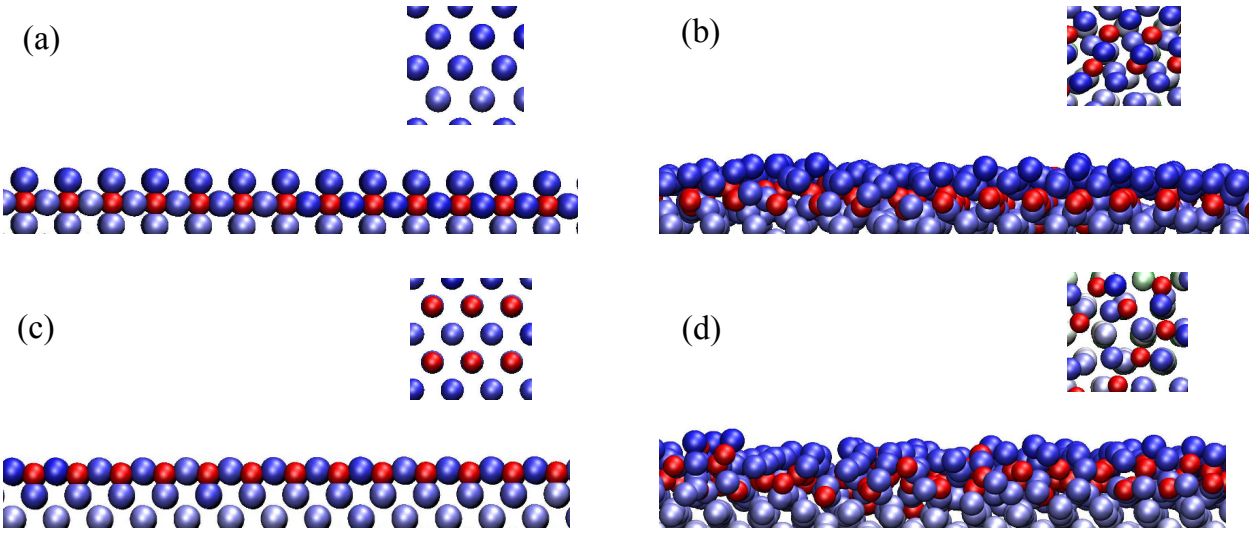


Figure 2.15: Snapshots of the initial (a) and final (b) configurations for O atoms initially placed in the square pyramidal-1 (110) subsurface site and snapshots of the initial (c) and final (d) configurations for O atoms initially placed in the square pyramidal-4 (110) subsurface site. Both snapshots are for simulations performed with a fractional coverage of 1.0 and temperature of 300 K. The color scheme follows that of Figure 2.3.

unknown. In any case, these simulations clearly show that O atoms move between surface and subsurface sites with the ReaxFF potential, as has been observed experimentally.[33,80,82,83]

The current work has demonstrated that the surface structure of oxidized silver can vary widely depending on reaction conditions. Further development or reparameterization of this potential specifically for this system could allow the force field to capture more subtle behaviors, such as the switch in binding preference observed in Ag(111), (surface sites being more favorable at low loading but subsurface sites being more favorable at high loading) that the current parameterization of the potential does not fully capture. This reconstruction must be due to interactions beyond the nearest neighbor, since our simulations show that the potential energy strictly becomes more favorable with coordination number of Ag around O, independent of O loading.

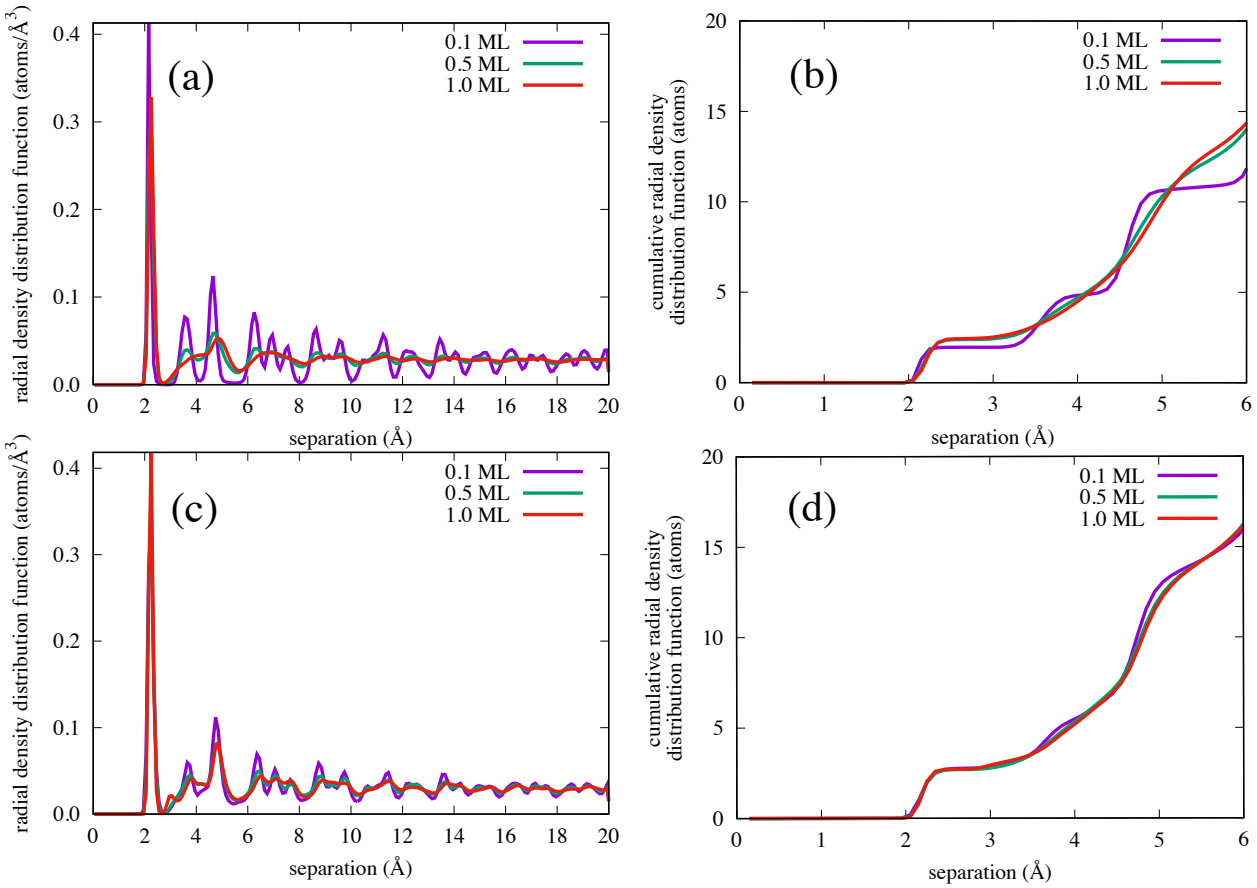


Figure 2.16: O-Ag RDF (a) and CN (b) of O atoms placed at the long subsurface bridge and RDF (c) and CN (d) of O atoms placed at the square pyramidal-1 subsurface sites on the (110) surface at 300 K and various coverages.

Chapter 3

Adsorption of atomic oxygen on the Ag(111) surface

3.1 Introduction

The interaction of oxygen with silver surfaces has been extensively studied due to the unique ability of silver to partially oxidize simple hydrocarbons, such as ethylene to ethylene oxide.[27,28,33,35,37,38,40,41,43,44,105–117] Despite the large number of both experimental and computational studies, the exact structure of the active epoxidation catalyst remains unknown. Experimental and simulated XPS experiments have shown the existence of at least two different oxygen phases on Ag(111), the most studied silver surface due to its stability.[34,37–39,107,113,115,117] One species, the nucleophilic oxygen, has been attributed to attack of the C-H bond of hydrocarbons while the second phase, electrophilic oxygen, is believed to insert into the C=C bond of ethylene through an oxometallacyle intermidate.[18,39] Discussion continues as to the nature of the electrophilic oxygen, with some reporting it to be oxygen residing in the near-surface, or subsurface, region of the crystal.[38,118] This has motivated several computational studies which have investigated the relative adsorption energies of AO on the surface and in the subsurface of Ag(111).[40,43,44,110] While some of these studies have investigated the coverage-dependent adsorption of AO up to a full monolayer, experiments show the surface coverage does not exceed approximately 0.4 ML.[29,32,34] In fact, the surface begins to reconstruct at much lower local coverages,

leading to several different reconstructions. Though the surface becomes saturated by 0.4 ML, temperature programmed desorption experiments show much higher total coverages of oxygen, suggesting oxygen penetrates the surface to reside in the subsurface and/or bulk region of the crystal.[35] While several computational studies have investigated the stability of various surface reconstructions under industrial reaction conditions,[22,34,41,109,119] the potential role of subsurface AO in the initiation of reconstruction has not been studied.

In the present work, we seek to investigate the adsorption energies of AO on the surface, in the subsurface, and in the subsurface region between layers two and three using DFT for seven coverages ranging from 0.08 to 0.58 ML. These results have been used to both qualitatively explain the saturation coverage of oxygen in several well-known reconstructions and what role subsurface AO might play in initiating this process. Additionally, these adsorption energies have also been used to develop a model which describes adsorption as a function of number and type of occupied neighbor sites.

3.2 Methods

DFT calculations were performed using VASP (versions 5.3.5 and 5.4.4),[94,95,120,121] a periodic plane-wave code. Electron exchange-correlation was described using the generalized gradient approximation (GGA) of Perdew, Burke, and Ernzerhof (PBE).[122,123] Interactions between nuclei and core electrons were described using the PAW method[98,124] constructed for the PBE functional. The plane-wave basis set was expanded with an energy cutoff of 400 eV. Methfessel-Paxton[100] smearing was used with a smearing width of 0.2 eV, giving an entropy change less than 0.01 meV/atom. The PBE functional, combined with a Monkhorst-Pack[99] k-point grid of 15×15×15, gave a lattice constant of 4.146 Å which compares well with the experimental value of 4.09 Å.[97]

The Ag(111) surface was described using a (4×3) unit cell and a six-layer periodic slab resulting in 12 atoms per layer for a total of 72 Ag atoms (Figure 3.1). The bottom three layers were fixed at the DFT-bulk geometry while the top three layers and all adsorbates were allowed to fully relax. A vacuum layer twice as thick as the surface slab was added above the topmost Ag layer to minimize interactions between replica slabs along the z-direction.

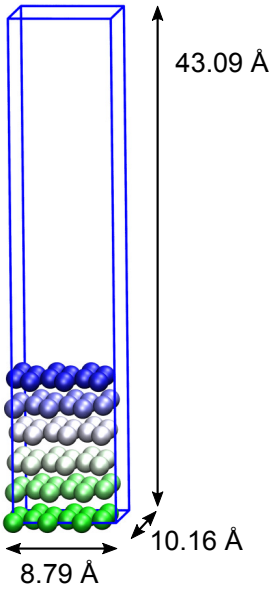


Figure 3.1: Six-layer, (4×3) Ag(111) supercell. The layers are colored such that dark blue Ag atoms are surface atoms and the color transitions to green as Ag atoms approach the bulk.

This resulted in a supercell with dimensions of 8.79 Å × 10.16 Å × 43.09 Å. A 5×5×1 Monkhorst-Pack k-point grid was used to sample the first Brillouin zone. The work function of the Ag(111) surface was calculated to be 4.44 eV which compares well to 4.46 ± 0.02 eV measured by Chelvayohan and Mee.[125]

DFT was used to calculate electronic energies and geometries of different optimized structures for various oxygen coverages on Ag(111). Initial starting geometries were optimized using the conjugate-gradient algorithm until the forces on the mobile nuclei (top three Ag layers and adsorbates) were less than 0.3 eV/Å. The partially relaxed structure was then further optimized using the quasi-Newton algorithm until the forces on the mobile nuclei were less than 0.05 eV/Å. The adsorption energy has been calculated in two ways. The first describes the system once it has reached equilibrium and assumes all AO are adsorbed equally. For this average-adsorption, $E_{ads,avg}$ is defined as

$$E_{ads,avg} = -\left(\frac{E_{O/Ag(111)} - \left(E_{Ag(111)} + N_O E_O\right)}{N_O}\right) \tag{3.1}$$

where $E_{O/Ag(111)}$ is the energy of the optimized O/Ag(111) structure, $E_{Ag(111)}$ is the energy of the optimized clean Ag(111) surface, E_O is the energy of an isolated oxygen atom, and N_O is the number of oxygen atoms present in the O/Ag(111) structure. The second adsorption energy models an instantaneous adsorption process to describe the adsorption of an additional AO to a surface at a given coverage. This incremental-adsorption, $E_{ads,inc}$, is defined as

$$E_{ads,inc} = -\left(E_{O/Ag} - E_{O-1/Ag(111)} - E_O\right) \tag{3.2}$$

where $E_{O-1/Ag(111)}$ is a coverage one AO less than the coverage $E_{O/Ag(111)}$. Charge transferred from Ag(111) to O during adsorption was calculated using the Bader method of charge density partitioning.[126–128]

3.3 Results

There are four high-symmetry surface sites and three high-symmetry subsurface sites on Ag(111). The surface sites are the fcc hollow, hcp hollow, bridge, and top. The subsurface sites, which sit directly beneath surface sites, are the octahedral site beneath the fcc hollow, the tetrahedral-1 site beneath the top site, and the tetrahedral-3 site beneath the hcp hollow. There is no subsurface site beneath the bridge surface site. Due to the inclusion of three mobile silver layers in our calculations, there is an additional subsurface region available in this study located between layers 2 and 3 of the Ag(111) supercell, denoted subsurface-23 in this work. The same types of sites are available in both the subsurface and subsurface-23 region. Top-down and side views of atomic oxygen placed in all surface, subsurface, and subsurface-23 sites are shown in Figure 3.2.

In the following sections, the effects of coverage on adsorption energy and charge of AO that occupy either surface or subsurface sites of Ag(111) are investigated. In addition, how these adsorption energies change when oxygen occupies both surface and subsurface sites is investigated. We have found adsorption energies for surface oxygen are very dependent on the number and type of occupied neighbor sites. These findings have thus been used to develop an adsorption model that predicts AO adsorption energies based on the number and types of occupied neighboring sites.

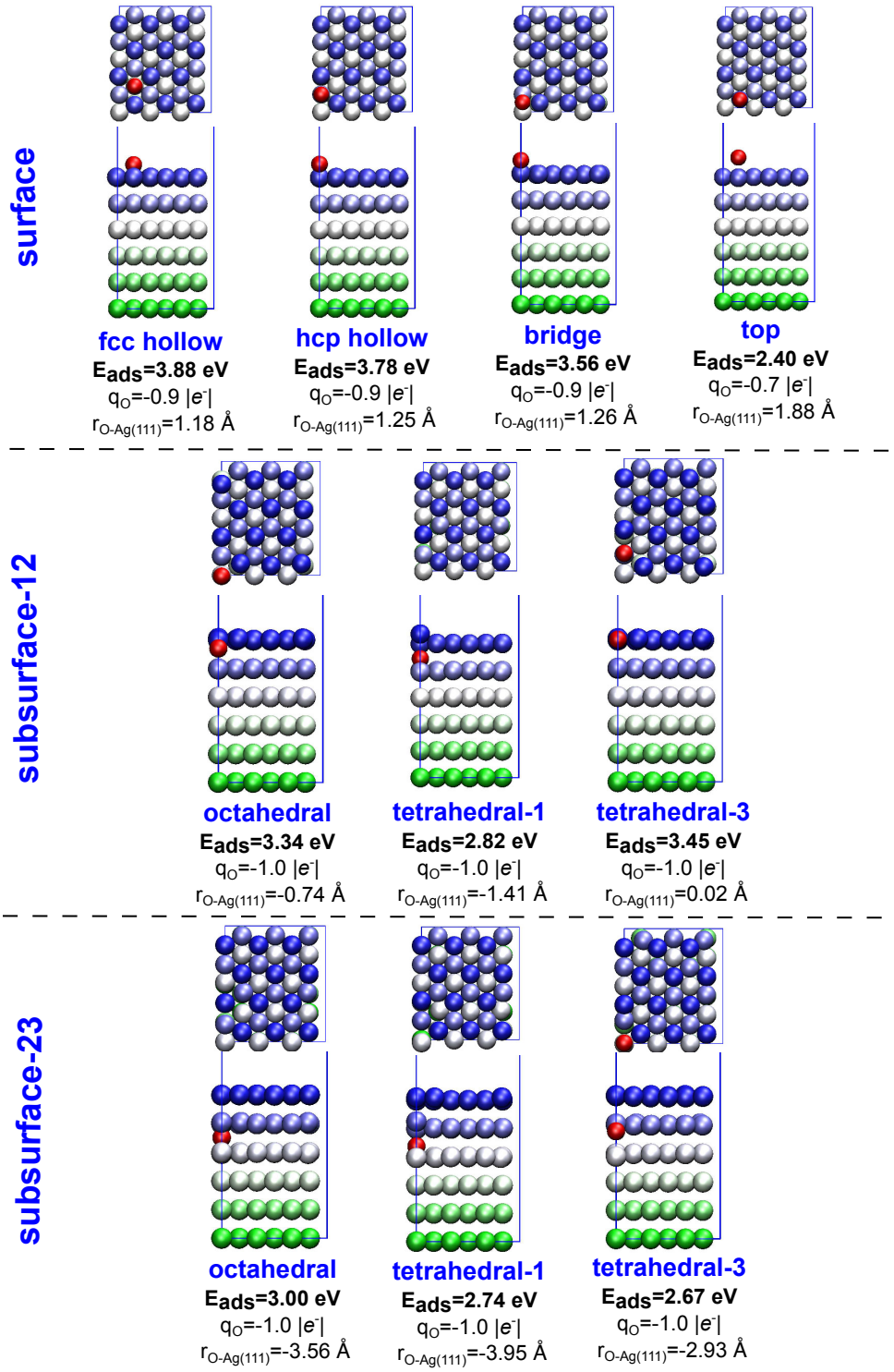


Figure 3.2: Top-down and side views of the high-symmetry sites on the surface, in the subsurface, and in the second subsurface (subsurface-23) regions of the Ag(111) surface. The adsorption energies, Bader charge on O, and the binding distances are provided for each site at an O coverage of 0.08 ML.

3.3.1 Pure surface and subsurface adsorption

While realistic surfaces would contain subsurface oxygen only in the presence of surface oxygen, it is of academic interest to investigate the adsorption properties of subsurface oxygen in the absence of surface oxygen to eliminate any cooperative contributions to adsorption between oxygen in the different regions. Thus, AO has been placed in the surface, the subsurface, or the subsurface-23 region. As shown in Figure 3.2, AO adsorption on the Ag(111) surface at the fcc hollow site is most favored with an E_{ads} of 3.88 eV at a coverage of 0.08 ML. At this coverage, the average and incremental adsorption energies are the same. Adsorption at the fcc hollow site is followed closely by adsorption at the hcp hollow site with an adsorption energy of 3.78 eV, a difference of only 0.1 eV. The bridge and top sites are less stable than the fcc hollow by 0.32 eV and 1.48 eV, respectively. The order of site preference agrees with previous studies reported in the literature.[43,44] Bader charge analysis of the adsorbed O atom at the surface sites show charge transfer of $-0.9\ |e^-|$ for AO at the two hollow and bridge sites, and $-0.7\ |e^-|$ at the top site. This shows a clear correlation between adsorption energy and charge transfer: in general, more charge transfer is associated with stronger AO adsorption. All $z_{O-Ag(111)}$ binding geometries, the distance from the O atom to the surface, range from 1.2 Å for the more strongly bound sites to 1.9 Å for the more weakly bound sites.

The octahedral and tetrahedral-3 sites are the preferred subsurface adsorption sites with adsorption energies of 3.34 eV and 3.45 eV, respectively. The tetrahedral-1 site has a slightly weaker adsorption energy of 2.82 eV. While adsorption at the tetrahedral-3 site is stronger than that at the octahedral site at this coverage, visualization of the optimized geometry and analysis of the binding geometry ($z_{O-Ag(111)}$) reveals the AO moved from the subsurface region to the surface during optimization. The tetrahedral-3 site is therefore not a stable adsorption site in the subsurface at a 0.08 ML coverage. Though generally the adsorption energy for AO in the subsurface is weaker than that on the surface at the same coverage, the charge transferred from the metal surface to the O atom is slightly greater with values of $-1.0\ |e^-|$ for the octahedral, tetrahedral-3, and tetrahedral-1 sites. The same trends in adsorption energy and charge transfer are observed when AO is placed in the subsurface-23

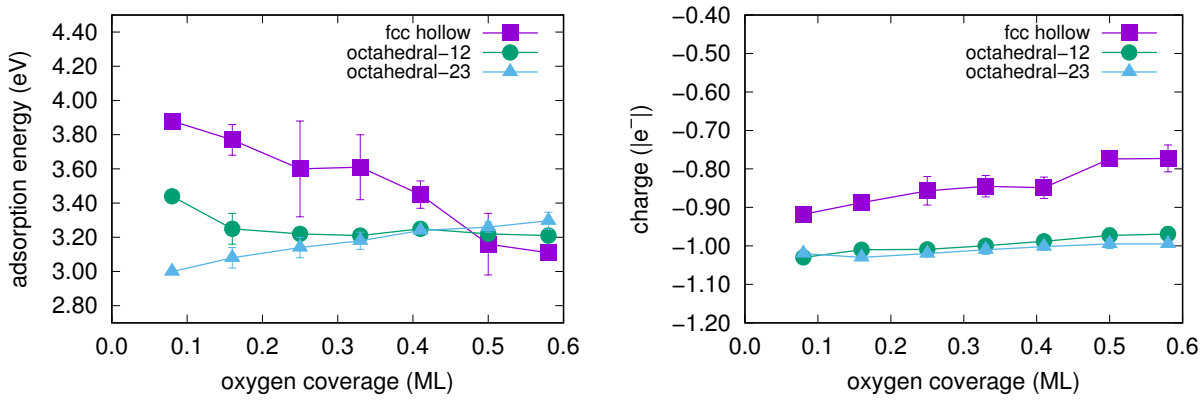


Figure 3.3: Average adsorption energy per AO ($E_{ads,avg}$) (left) and charge (right) as a function of AO coverage. For intermediate coverages, two geometries have been considered. The data point is the average adsorption energy or charge with the range given by the error bars. The current adsorption energy calculated at 0.41 ML agrees well with the experimental value calculated by Campbell using temperature programmed desorption experiments.[28]

region, though the adsorption energy again decreases slightly (Figure 3.2). The adsorption energy for AO in the octahedral subsurface-23 site is 3.00 eV compared to 3.34 eV between layers 1 and 2.

In addition to 0.08 ML, coverages of 0.16, 0.25, 0.33, 0.41, 0.50, and 0.58 ML have also been studied to see how the AO-adsorption energy changes with coverage for the favored surface, subsurface, and subsurface-23 sites. Each coverage considers only occupation of the favored site of interest. For all but the 0.08 ML coverage, several possible AO arrangements exist. To investigate the fundamentals of adsorption, the current study does not include ordered adsorption or surface reconstructions; therefore, two geometries for each intermediate coverage have been investigated. In one geometry, AO atoms have been placed in nearest-neighbor sites of the same high-symmetry site while the other geometry attempts to maximize the interatomic oxygen distance. These geometries are expected to model the two extremes of possible AO interaction for a given coverage. Figure 3.3 shows $E_{ads,avg}$ (left) and charge (right) with respect to coverage for the favored surface and subsurface sites between layers 1 and 2 and between layers 2 and 3. For the intermediate coverages where multiple geometries were examined, the average is plotted with the range shown by the error bars. It is seen that $E_{ads,avg}$ decreases for surface AO with increasing coverage but remains relatively unchanged for subsurface or subsurface-23 AO. The decrease in surface $E_{ads,avg}$ is large enough that at

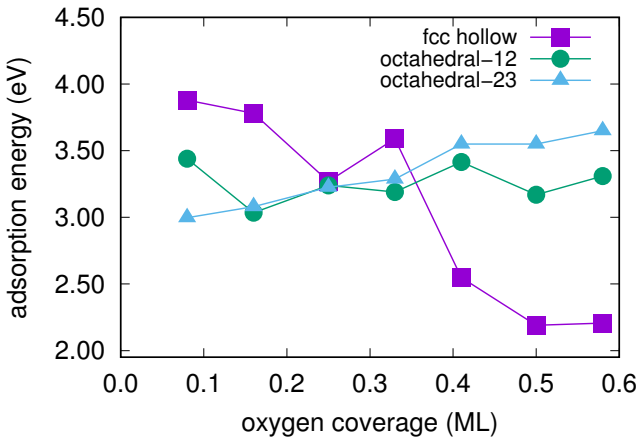


Figure 3.4: Incremental adsorption energy ($E_{ads,inc}$) as a function of coverage for the geometry at each coverage with the largest average interatomic oxygen spacing for the favored surface, subsurface, and subsurface-23 sites.

a coverage of 0.50 ML, adsorption on the surface and in both regions of the subsurface are equally favorable. At coverages beyond 0.50 ML, the average adsorption per oxygen becomes less for surface AO than for subsurface or subsurface-23 AO. Similar behavior is observed for the coverage dependence of charge transfer. The charged transferred from silver to oxygen decreases with increasing coverage for surface oxygen but remains fairly constant for AO in subsurface and subsurface-23 sites.

The same qualitative results are obtained when plotting $E_{ads,inc}$ as a function of coverage for the geometries which maximize the O-O distances; however, the observed flip in preference from surface to subsurface at high coverages is much more pronounced and occurs at a slightly lower coverage. The nearest-neighbor geometries have been neglected here as moderate surface coverages pushed oxygen atoms out of the fcc hollow site. As shown in Figure 3.4, $E_{ads,inc}$ on the surface decreases drastically with increasing coverage. There is a decrease of 1.04 eV when increasing the surface coverage from 0.33 to 0.41 ML. This sharp decrease can be explained by visually examining the unreconstructed Ag(111) surface. Beyond a coverage of 0.33 ML, a nearest neighbor site must be occupied (Figure 3.5). Due to the large amount of charge on each AO, there is a large, unfavorable interaction to occupy neighboring surface sites. Thus, it is much less favorable to add an additional AO to a 0.33 ML-covered surface. It would be more favorable for an additional AO to occupy a subsurface site where the negative charge on oxygen appears to be better stabilized. The adsorption energy for adding

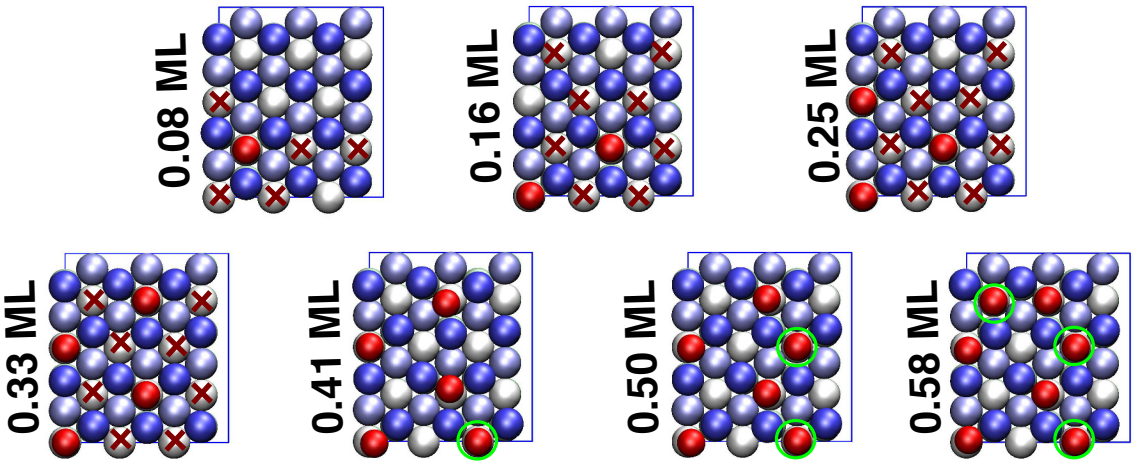


Figure 3.5: Top-down views of AO at the fcc hollow site for several coverages, showing the requirement that a nearest neighbor site be occupied beyond a coverage of 0.33 ML. For the 0.33 ML coverage and below, nearest-neighbor sites to an occupied fcc hollow site have been marked with an "x". Beyond this coverage, the added oxygen is marked with a green circle.

an additional AO to the subsurface, and especially the subsurface-23, appears to show a cooperative effect with $E_{ads,inc}$ increasing slightly with coverage.

While no surface reconstruction has been considered at this stage in the study, it is encouraging that a change in preference from surface to subsurface is observed around a surface coverage of 0.50 ML for the average adsorption and between 0.33 and 0.41 ML for the incremental adsorption. As mentioned previously, there are several Ag(111) surface reconstructions with saturated-surface coverages between 0.375 and 0.41 ML.[29,32,34] Our calculations have also shown that the silver surface can be distorted in the presence of subsurface oxygen at tetrahedral-1 and tetrahedral-3 subsurface and subsurface-23 sites (Figure 3.2). Each of these sites has a silver atom either directly above or directly below the AO. This silver atom is displaced vertically to accommodate the AO. Tetrahedral sites could become occupied as oxygen diffuses in the subsurface or subsurface-23 region, breaking the high symmetry of the surface and initiating reconstruction. One such reconstruction is the $p(4\times4)$ for which Campbell[80] has calculated an AO adsorption energy of 3.42 eV using temperature programmed desorption and Redhead analysis.[129] This adsorption energy is in excellent agreement with our calculated $E_{ads,avg}$ of 3.45 eV for the fcc hollow site at a 0.41-ML coverage.

Table 3.1: The adsorption energies (average and incremental) for a given set of mixed coverages investigated in the present study. The site-specific coverage breakdown, as well as the total coverage are also given.

Θ_{surf} (ML)	$\Theta_{subsurface}$ (ML)	$\Theta_{subsurface-23}$ (ML)	Θ_{total} (ML)	$E_{ads,inc}$	$E_{ads,avg}$
0.50	0.00	0.00	0.50	3.06	3.29
0.41	0.08	0.00	0.50	3.05	3.29
0.41	0.00	0.08	0.50	3.26	3.32
0.00	0.50	0.00	0.50	3.23	3.24
0.00	0.41	0.08	0.50	3.32	3.26
0.25	0.33	0.00	0.58	2.95	3.24
0.25	0.25	0.08	0.58	3.32	3.30
0.50	0.16	0.00	0.66	2.62	3.16
0.41	0.25	0.00	0.66	4.10	3.34
0.41	0.16	0.08	0.66	3.40	3.26

3.3.2 Mixed surface and subsurface adsorption

In addition to calculating adsorption energies for oxygen atoms either on the surface or in the subsurface, mixed coverages, those that have oxygen present in both the surface and subsurface, have been investigated. Coverages investigated include total coverages of 0.50, 0.58, and 0.66 ML with the AO atoms distributed among the surface and subsurface in different ways. Table 3.1 gives the distribution of coverage among the surface, subsurface, and subsurface-23 regions, total coverage, $E_{ads,avg}$, and $E_{ads,inc}$. As can be seen in Table 3.1, $E_{ads,avg}$ is fairly robust across the total coverages investigated; however, $E_{ads,inc}$ depends less on total coverage and more on the distribution of AO between the different regions of the surface.

3.3.3 Adsorption model

The adsorption energies reported in Section 3.3.1 have been used to develop a model to describe AO adsorption on Ag(111). Analysis of the pure- and mixed-coverage geometries show no clear correlation between adsorption energy and total coverage. Rather, it appears adsorption depends on the number and type of neighbor sites occupied by AO. Thus, the

model developed in the present work predicts adsorption energy as a function of number and types of neighbors.

In this model, we consider oxygen atoms adsorbed at fcc hollow sites on the surface, octahedral sites in the subsurface, and tetrahedral-3 sites in the subsurface-23. While the tetrahedral-3 site is not the most favored adsorption site in the subsurface-23 region, this site sits directly below the octahedral subsurface site, simplifying our model slightly. The total adsorption energy (E_{total}) of N oxygen atoms adsorbed at these sites is given by

$$E_{total} = n_s E_s + n_{ss12} E_{ss12} + n_{ss23} E_{ss23} + \Delta E_s + \Delta E_{ss12} + \Delta E_{ss23} + \Delta E_{s-ss12} + \Delta E_{ss12-ss23} \quad (3.3)$$

where

$$N = n_s + N_{ss12} + N_{ss23}, \quad (3.4)$$

$$\Delta E_s = n_{n-s}\Delta E_{n-s} + n_{nn-s}\Delta E_{nn-s} + n_{nnn-s}\Delta E_{nnn-s}, \quad (3.5)$$

$$\Delta E_{ss12} = n_{n-ss12}\Delta E_{n-ss12} + n_{nn-ss12}\Delta E_{nn-ss12} + n_{nnn-s12}\Delta E_{nnn-ss12}, \quad (3.6)$$

$$\Delta E_{ss23} = n_{n-ss23}\Delta E_{n-ss23} + n_{nn-ss23}\Delta E_{nn-ss23} + n_{nnn-s23}\Delta E_{nnn-ss23}, \quad (3.7)$$

$$\begin{aligned} \Delta E_{s-ss12} = {} & n_{above-s-ss12}\Delta E_{above-s-ss12} + n_{n-s-ss12}\Delta E_{n-s-ss12} \\ & + n_{nn-s-ss12}\Delta E_{nn-s-ss12} + n_{nnn-s-ss12}\Delta E_{nnn-s-ss12}, \end{aligned} \quad (3.8)$$

and

$$\begin{aligned} \Delta E_{ss12-ss23} = {} & n_{above-ss12-ss23}\Delta E_{above-ss12-ss23} + n_{n-ss12-ss23}\Delta E_{n-ss12-ss23} \\ & + n_{nn-ss12-ss23}\Delta E_{nn-ss12-ss23} + n_{nnn-ss12-ss23}\Delta E_{nnn-ss12-ss23}. \end{aligned} \quad (3.9)$$

In the above equations, n_{type} is the number of occupied sites of that type or the number of neighbor interactions of that type, E_{type} denotes an adsorption energy of that type, ΔE_{type} denotes a pair-interaction energy of that type, s denotes a surface site, $ss12$ denotes a subsurface site, $ss23$ denotes a subsurface-23 site, n denotes a nearest-neighbor pair, nn denotes a next-nearest neighbor pair, nnn denotes a next-next-nearest-neighbor pair, and *above* denotes a pair in which one atom is directly above the other atom. The subscript $n - type$ denotes a nearest-neighbor pair of oxygen atoms adsorbed at the same

Table 3.2: Calculated values of the O/Ag(111) adsorption model parameters.

ΔE (eV)	E_{ads}	*above*	n	nn	nnn
s	3.88	–	−0.36	−0.12	0.02
$ss12$	3.34	–	−0.04	−0.31	−0.12
$ss23$	2.67	–	0.20	0.02	−0.06
$s - ss12$	–	−0.57	−0.09	−0.20	−0.09
$ss12 - ss23$	–	0.16	0.07	0.08	0.02

type of site, whereas the subscript $n - type1 - type2$ denotes a nearest-neighbor pair of oxygen atoms adsorbed at two different types of sites. Positive adsorption energies are exothermic (favorable). A positive interaction energy indicates that the interaction is attractive (cooperative), and a negative interaction energy indicates that the interaction is repulsive (non-cooperative). Interactions beyond next-next-nearest neighbor pairs are ignored. The values of the parameters in the model are given in Table 3.2.

Using these interaction energies, the model-predicted adsorption energies have been calculated for the pure surface, subsurface, and subsurface-23 geometries for coverages 0.25 ML and greater. As can be seen in Figure 3.6, the present model qualitatively describes the adsorption trends observed in the DFT calculations (left panel of Figure 3.3). The model predicts that $E_{ads,avg}$ decreases for surface AO while increasing slightly for subsurface-23 AO at higher coverages, leading to a flip in preferred adsorption site, though the coverage at which the flip occurs deviates from that calculated with DFT. This model was also used to predict adsorption energies of mixed coverages. Using the interaction energies given in Table 3.2, the present model calculated average adsorption energies within 10% error of the DFT-calculated values. This is a very encouraging result for the simple model detailed here.

3.4 Summary and conclusions

In conclusion, the adsorption energy of AO on Ag(111) has been investigated using DFT. In agreement with previous reports in the literature, the fcc hollow surface site and octahedral subsurface site were favored.[43,44] Our work revealed a flip in preference from surface to subsurface between a coverage of 0.3 and 0.5 ML, depending on whether an

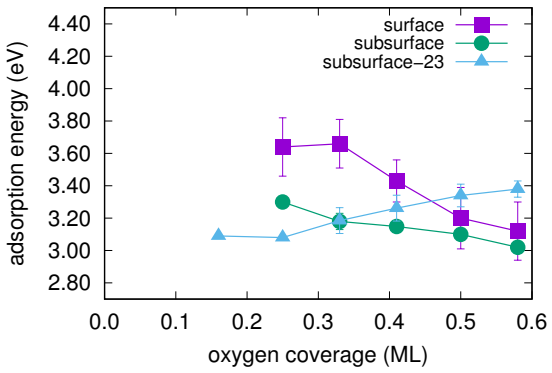


Figure 3.6: Average adsorption energy per AO ($E_{ads,avg}$) as a function of AO coverage calculated using the adsorption model developed in the present study.

average or instantaneous adsorption energy was calculated. Further investigation showed the importance of nearest-neighbor interactions on the surface. We hypothesize the non-cooperative effect of nearest-neighbor site occupation on the Ag(111) surface leads to the change in preference to subsurface adsorption once such nearest-neighbor interactions can no longer be avoided on the surface where the anionic character of the adsorbed AO is less stabilized. Our calculations show occupation of certain subsurface sites lead to surface distortions which could act as nucleation points for surface reconstruction. This new insight into the significant role of nearest-neighbor interactions led to the development of an adsorption model which can predict adsorption energies based of the geometry of adsorbed surface, subsurface, and subsurface-23 oxygen atoms. Our current model can only account for oxygen at one type of site in each adsorption region and can have up to a 10% error with respect to our DFT calculations. Work is on-going to extend this model to additional high-symmetry sites and investigate any additional interactions which could reduce the error.

Chapter 4

Atomic Oxygen adsorption on Ag(110): A comparison with Ag(111)

4.1 Introduction

While many investigations into the interaction of oxygen with low-Miller index surfaces have focused on Ag(111) due to its inertness when compared to other faces of silver, Ag(110) has also been of great interest as a catalyst for the partial oxidation of ethylene. Several studies have shown that both the Ag(111) and Ag(110) facets of silver are selective catalysts for ethylene epoxidation.[21,130] Gravil and Bird have shown that atomic-oxygen species are easily accessible on Ag(110) due to an O_2-dissociation energy of 0.62 eV.[131] Similar studies by Roy *et al.*[46] and Rawal *et al.*[42] investigated the dissociation of O_2 on Ag(110), as well, calculating a dissociation barrier of 0.43 and 0.42 eV, respectively, in fair agreement with Gravil and Bird[131] but in excellent agreement with each other. Roy *et al.* also observed some oxygen initially placed on the surface diffused to the subsurface region of the slab during geometry optimization.[46] This suggests a small or non-existent barrier for AO diffusion into the subsurface on Ag(110).

A computational investigation by van den Hoek, Baerends, and van Santen showed that subsurface oxygen plays a significant role in ethylene epoxidation.[132] Using cluster models, they showed a barrier to ethylene epoxidation in the absence of subsurface oxygen on Ag(110) due to a repulsive interaction between surface AO and ethylene. This barrier disappears

when oxygen occupies both surface and subsurface sites as ethylene-oxygen antibonding bands become filled.

Though significant work has been done to investigate the interaction of AO with Ag(110), no study could be found that elucidated the coverage dependence of these interactions. A computational study which gives a head-to-head comparison of Ag(110) with Ag(111) is also lacking at present. In the current work, we compare the adsorption energy of key AO coverages on Ag(110) to those investigated on Ag(111) in Chapter 3.

4.2 Methods

To ensure the present results could be compared directly with those reported in Chapter 3, the same computational parameters as those discussed in Section 3.2 have been used. The Ag(110) surface was described using a (3×4) unit cell and a six-layer periodic slab resulting in 12 atoms per layer for a total of 72 Ag atoms (Figure 4.1). As with the Ag(111) slab, the bottom three layers of the Ag(110) supercell have been held fixed at the DFT-bulk geometry while the top three layers and all adsorbates were allowed to fully relax. With a vacuum twice as thick as the surface slab, the resulting supercell had dimensions of 11.73 Å × 12.44 Å × 26.38 Å. A 5×5×1 Monkhorst-Pack k-point grid was used to sample the first Brillouin zone. The work function of the Ag(110) surface was calculated to be 4.15 eV, which compares very well to 4.14 ± 0.04 eV measured by Chelvayohan and Mee.[125]

DFT was used to calculate electronic energies and geometries of different optimized structures of three different oxygen coverages on Ag(110). The algorithms and force criteria match those used for optimizations of the Ag(111) surface reported in Section 3.2. For this study, adsorption energies were only calculated in a way which models equilibrium behavior by assuming all AO are adsorbed equally. This average-adsorption, E_{ads} is defined as

$$E_{ads} = -\left(\frac{E_{O/Ag(110)} - \left(E_{Ag(110)} + N_O E_O\right)}{N_O}\right) \tag{4.1}$$

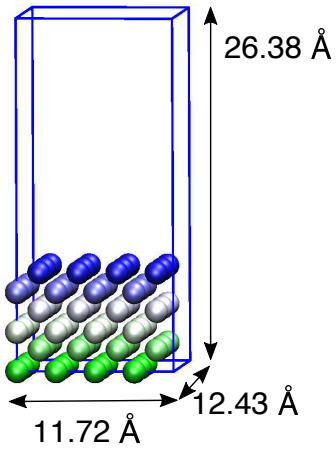


Figure 4.1: Six-layer, (3×4) Ag(110) supercell. The layers are colored such that dark blue Ag-atoms are surface atoms and the color transitions to green as Ag atoms approach the bulk.

where $E_{O/Ag(110)}$ is the energy of the optimized O/Ag(110) structure, $E_{Ag(110)}$ is the energy of the optimized, clean Ag(110) surface, E_O is the energy of an isolated oxygen atom, and N_O is the number of oxygen atoms present in the O/Ag(110) structure.

4.3 Results

There are four high-symmetry surface sites and four high-symmetry subsurface sites on Ag(110). The surface sites are the fourfold hollow, long bridge, short bridge, and top. The subsurface sites, which sit directly beneath surface sites, are the square pyramidal-4 site beneath the fourfold hollow site, the short bridge subsurface site beneath the long bridge surface site, the long bridge subsurface site beneath the short bridge surface site, and the square pyramidal-1 site beneath a top site. Due to the inclusion of three mobile silver layers in our calculations, an additional subsurface region is available, called the subsurface-23 region. This additional region is located between layers 2 and 3 of the Ag(110) supercell. While the same type of sites exist in the subsurface and subsurface-23 regions, the two square pyramidal sites become equivalent due to symmetry in the subsurface-23. This symmetry is broken in the subsurface region due to the termination at the surface. Top-down and side

views of AO placed in all surface, subsurface, and subsurface-23 sites are shown in Figure 4.2.

In the following sections, the effects of coverage on adsorption energy and AO charge that occupy either surface or subsurface sites of Ag(110) are investigated. These results will be compared to those from a similar study on Ag(111) reported in Chapter 3.

4.3.1 Surface relaxation of the clean surface

Significant structural differences between the (111) and (110) facets of silver exist prior to adding adsorbates to the system. These differences involve both the interlayer and interatomic spacing of silver atoms and are shown in Figure 4.3. Though both supercells contain 12 atoms in each of the six layers, the spacing between each layer is much less in Ag(110) than in Ag(111). There is a 2.39-Å space between layers in the Ag(111) surface while this distance is reduced to 1.47 Å in the Ag(110) slab. These interlayer spacings are inherent from cleaving bulk silver to give the desired surface, prior to surface relaxation. Due to reduced coordination numbers of the surface atoms, the interlayer spacing of Ag(110) near the surface decreases by 9% between layers 1 and 2 and increases by approximately 4% between layers 2 and 3 upon relaxation, giving spacings of 1.33 Å and 1.53 Å, respectively. No such relaxation is observed on Ag(111) as this is the close-packed surface. Due to this surface relaxation, the subsurface region of Ag(110) is very small, suggesting AO will have to lie in the plane of the silver atoms to be accommodated in this region. While this was not seen to happen with Ag(111) and may seem unlikely, the interatomic spacing of silver on Ag(110) is larger than that on Ag(111). The (111) facet of silver has a three-fold atomic symmetry, where each surface atom makes up one vertex of an equilateral triangle of with nearest-neighbor atoms in the absence of surface reconstructions. In our model, this interatomic distance is 2.93 Å. Ag(110) has a rectangular symmetry, which leads to long and short bridge sites on the surface. The Ag-Ag distance along the rows (short bridge) is 2.93 Å whereas the Ag-Ag distance across the rows (long bridge) is 4.15 Å. There is, therefore, significant space for oxygen to reside in the long bridge site, both on the surface and in the subsurface.

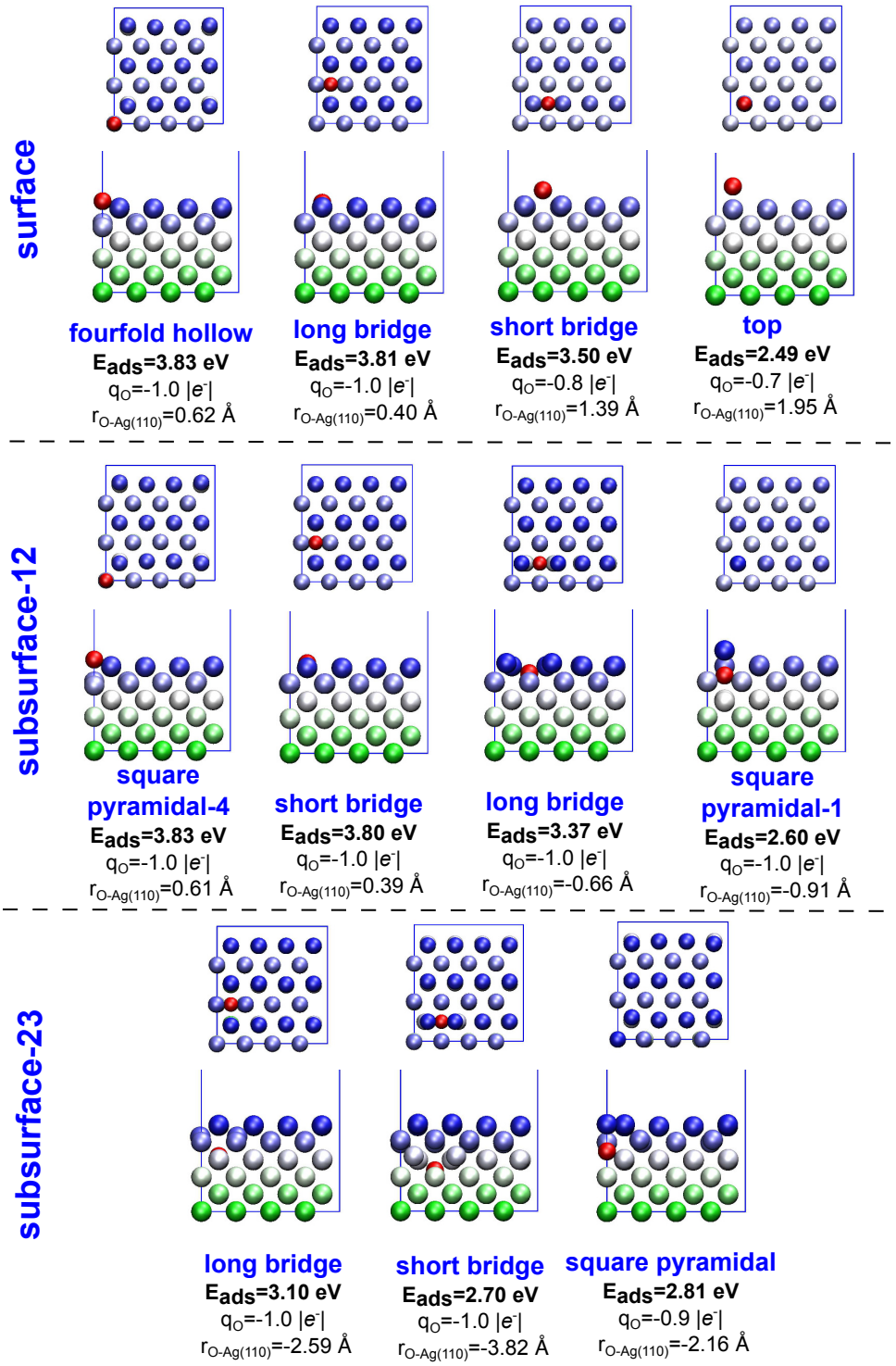


Figure 4.2: Top-down and side views of the high-symmetry sites on the surface, in the subsurface, and in the second subsurface (subsurface-23) regions of the Ag(110) surface. The adsorption energies, Bader charge on O, and the binding distances are provided for each site at an O coverage of 0.08 ML.

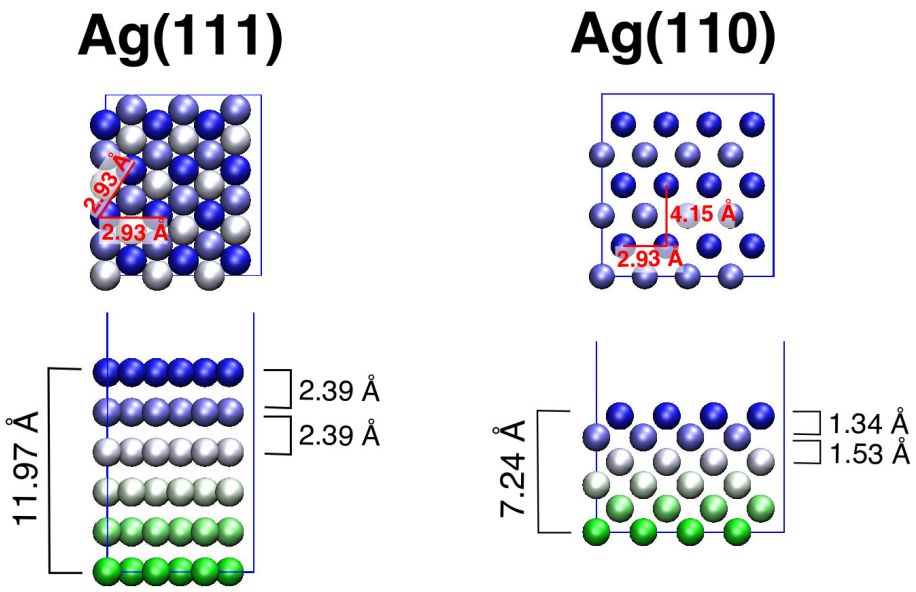


Figure 4.3: Top-down and side views of the relaxed Ag(111) and Ag(110) surfaces with in-plane nearest-neighbor and interlayer distances given for each surface.

4.3.2 Pure surface and subsurface adsorption

To compare the interaction of AO on Ag(110) with that of Ag(111), we have calculated the adsorption energy of oxygen on the surface, in the subsurface, or in the subsurface-23 region at a 0.08 ML coverage. As shown in Figure 4.2, AO adsorption on the Ag(110) surface at the fourfold hollow and long bridge sites are equally favored with a E_{ads} of 3.83 and 3.81 eV, respectively. Adsorption at these sites is followed by adsorption at a short bridge site (E_{ads}=3.50 eV) with the top site being least favored (E_{ads}=2.49 eV). This qualitatively agrees with previous studies reported in the literature.[42] Bader charge analysis of the adsorbed O atom at the surface sites show charge transfer of approximately $-1.0\ |e^-|$ for AO at the hollow and long bridge sites, $-0.8\ |e^-|$ at the short bridge site, and $-0.7\ |e^-|$ at the top site. These results are in excellent agreement with adsorption on the Ag(111) surface where E_{ads} at the hollow sites was 3.88 and 3.78 eV, E_{ads} at the bridge site was 3.56 eV, and E_{ads} at the top site was 2.40 eV. Bader charges on Ag(111) ranged from -0.9 to $-0.7\ |e^-|$.

Due to the reduced interlayer spacing in the Ag(110) subsurface, adsorption studies in the subsurface revealed several sites were not stable. While the short bridge and square pyramidal-4 subsurface sites are shown to have the most favorable adsorption energies,

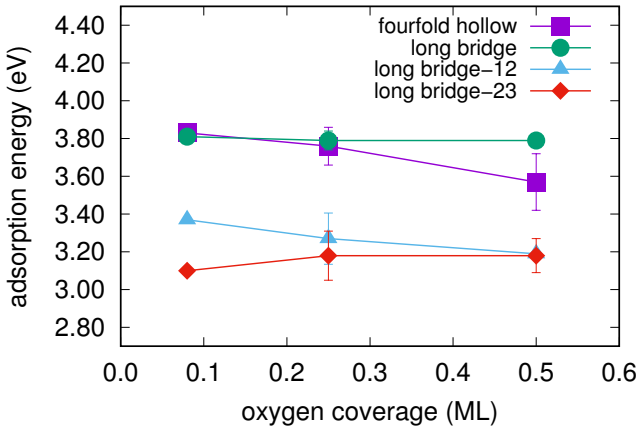


Figure 4.4: Average adsorption energy per AO ($E_{ads,avg}$) as a function of AO coverage. For intermediate coverages, two geometries have been considered. The data point is the average adsorption energy with the range given by the error bars.

visualization of the optimized geometries and analysis of the binding geometries ($z_{O-Ag(110)}$) reveals the AO moved from the subsurface region to the surface during optimization. This is not surprising as these two subsurface sites are directly beneath the most favored surface sites. This leaves the long bridge and square pyramidal-1 sites as the only stable subsurface sites at a 0.08 ML coverage on Ag(110) with adsorption energies of 3.37 and 2.60 eV, respectively. The short bridge site in the subsurface-23 region was again found not to be a stable adsorption site at 0.08 ML, with the AO moving to the region between layers 3 and 4. As in the subsurface, the long bridge site was found to be the favored adsorption site in the subsurface-23 region with an adsorption energy of 3.10 eV.

While several coverages were investigated in Chapter 3 for AO adsorption on Ag(111), only adsorption at two additional coverages of 0.25 and 0.50 ML were calculated for Ag(110). Investigation of adsorption at these additional coverages should give a reasonable comparison with Ag(111) as it was by 0.50 ML that the change in preference from surface to subsurface occurred. If similar behavior occurs on Ag(110), it is reasonable that it should occur by 0.50 ML. Figure 4.4 shows AO adsorption at the favored surface, subsurface, and subsurface-23 sites on Ag(110) as a function of coverage. In contrast to the flip in preference calculated at high coverages on Ag(111), surface adsorption is still significantly favored over adsorption in the subsurface at 0.50 ML. In fact, adsorption at the surface long bridge site is unaffected by the increased coverage. This is not the case for oxygen adsorption at the fourfold hollow

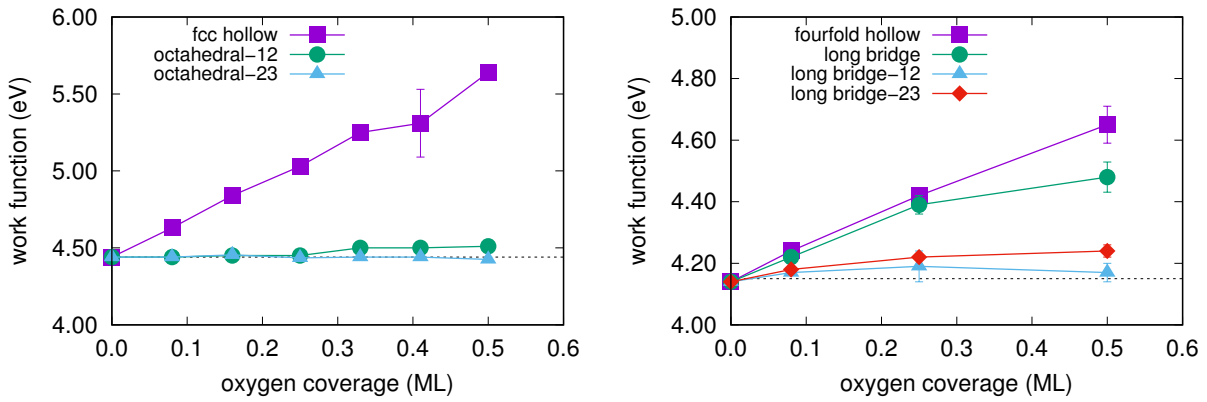


Figure 4.5: Average work function of Ag(111) (left) and Ag(110) (right) surfaces as a function of AO coverage. For intermediate coverages, two geometries have been considered. The data point is the average work function with the range given by the error bars.

site where E_{ads} decreases to 3.57 eV at a 0.50 ML coverage, 0.26 eV less than adsorption of a single oxygen atom at the hollow site. The adsorption energy at the fcc hollow site on Ag(111) decreased from 3.88 to 3.16 eV (ΔE_{ads}=0.72 eV) for the same change in coverage.

4.3.3 Coverage dependence of work function

To investigate the effect of coverage on the electronic properties of the two silver facets, work functions were calculated at each coverage (Figure 4.5). As shown on the left, Ag(111) shows a fairly linear increase in work function with increasing coverage. There is no such change in work function when AO is placed in the subsurface. Similar behavior is calculated on the Ag(110) surface, where the work function increases more when AO is placed at a surface site rather than a subsurface site. While the trends between Ag(111) and Ag(110) are similar, the change in work function going from 0.08 to 0.50 ML is much larger for the close-packed surface. The work function on Ag(110) is always less than that on Ag(111). Li, Stampfl, and Scheffler noted that large changes in work function, such as that calculated on Ag(111), indicates the surface AO will be strongly anionic.[109] This should disfavor epoxidation where the electrophilic oxygen needs to insert into the C=C double bound. More negatively charged AO will repel this bond. Therefore, epoxidation should be favored on the Ag(110) surface based on the electronics of the two unreconstructed facets at moderate oxygen coverages.

4.4 Summary and conclusions

This work shows several key differences in the way two low-Miller-index surfaces interact with AO as a function of coverage. While AO preferably adsorbs on the surface of Ag(111) at low coverages, adsorption in the subsurface becomes favored at high coverages. This change in preference was not observed on the Ag(110) facet. It is reasonable that AO binds much less favorably in the subsurface of Ag(110) than the surface due to the significantly reduced interlayer spacing. There is, however, more interatomic space which reduces the repulsion of the negatively-charged adsorbed oxygen atoms. This O-O separation is only available on Ag(111) by accessing subsurface sites. Additionally, the work function of both surfaces increases when oxygen is placed at surface sites but remains relatively unchanged when placed in subsurface sites. The calculated change in work function for surface adsorption on both surfaces indicate more O-O repulsion on Ag(111), suggesting epoxidation would preferably occur on Ag(110), though this preference is likely very slight.

Chapter 5

Elucidation of the reaction mechanism of $C_2 + N_1$ aziridination from tetracarbene iron catalysts

5.1 Disclosure

The work presented in the following chapter was done in collaboration with the group of Professor David Jenkins at the University of Tennessee, Knoxville. All experimental work was performed by Preeti Chandrachud under the guidance of David Jenkins. Preliminary calculations were performed by Jesse Kern and completed by Sara Isbill, under the guidance of Sharani Roy. It will soon be submitted for publication.

5.2 Introduction

Catalytic aziridination has made noteworthy strides in the last decade due to the development of many new catalysts.[53,60,61,70,133–136] These advances are significant since aziridines are found not only in natural products,[3,4,137] but are also critical intermediates that can be ring-opened stereospecifically or transformed into a plethora of more complex heterocyclic ring systems *via* ring expansion.[8,138–143] For example, Kang[10] and Ghorai[144] have showcased chiral ring-opening reactions with *meso* aziridines, while Zhao, Chai and Wang developed

the first pyrroloindoline synthesis from aziridines and indoles.[145–147] Although synthesis of primary aziridines has advanced recently with improved stereochemical control, a cost-effective method for the synthesis of biologically significant aziridines that is compatible with a variety of R-groups off the nitrogen is still a critical synthetic challenge. A $C_2 + N_1$ route is an effective method of catalytic aziridination, which can be improved further with a greater understanding of its mechanism.

A $C_2 + N_1$ approach to aziridination features an alkene (C_2) and a nitrene fragment (N_1) combining to make the aziridine.[148] Nitrene fragments most commonly come from protected azides (e.g. TsN_3[9,73,149] $TcepN_3$,[67] and $(SES)N_3$),[72,73] aryl azides[56,74,150] and, more recently, alkyl azides,[58] all of which are easy to synthesize.[150–153] While porphyrin and salen complexes are successful catalysts for *N*-substituted aziridination,[61–63,73,74] very few mechanistic studies have been performed for these systems.[64,77] We have reported two iron *N*-heterocyclic carbene (NHC)-based catalysts for aziridine synthesis using aliphatic alkenes with aryl as well as alkyl azides.[56,58] This pair of catalysts yields the first set that is effective with aliphatic alkenes and these two classes of nitrene reagents, making them an ideal showcase for a mechanistic study.[68]

While the basic components of a catalytic cycle for our tetracarbene iron catalysts have been proposed previously (Scheme 5.1),[78] the individual elementary steps within each component of the cycle (shown as A, B, and C) have not been examined. These individual steps have considerable implications for the effectiveness of the aziridination reaction, and understanding them can answer several key questions about the catalysis. For example, why do alkyl azides react catalytically with the second-generation system (**5.1**) but not with the first-generation system (**5.2**)? Many other aziridination catalysts are limited to reactions with aryl azides as well.[74,150] More critically, how does the alkene react with the purported iron-imide intermediate? Does it proceed through an azametallacyclobutane intermediate (box reaction) or a series of one-electron reductions (open-chain-radical reaction)? This question is particularly critical because of the implications for stereochemical control. Finally, what is the role of the metallotetrazene during catalysis? Does prevention of metallotetrazene allow for catalysis to occur using lower alkene loadings, thus making it much more economical? Elucidating these aspects of the mechanism for our catalytic systems

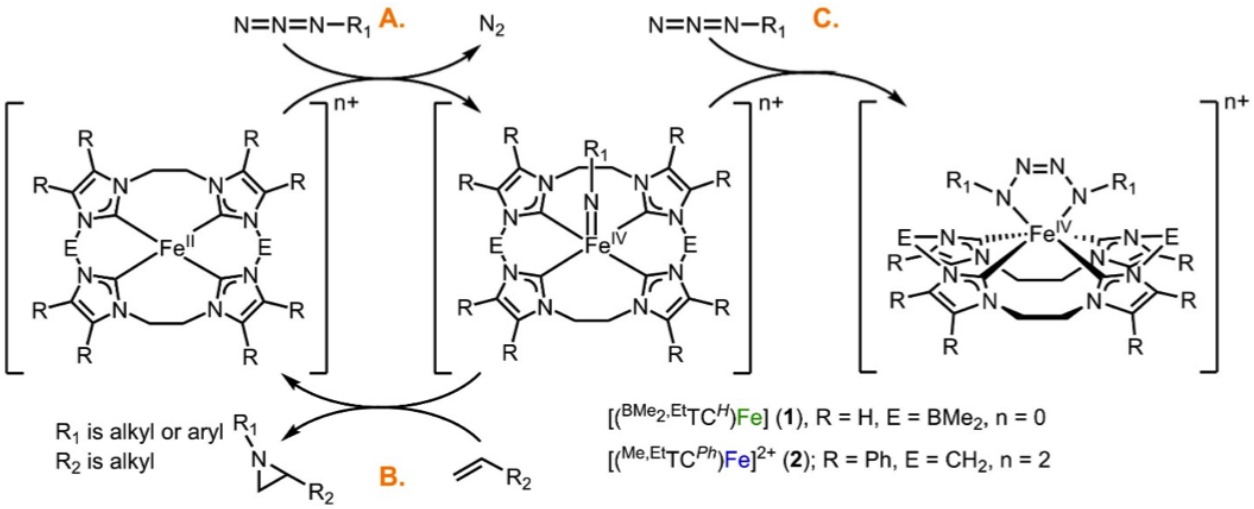


Figure 5.1: Catalytic cycle for the formation of aziridine from tetracarbene iron catalysts **5.1** and **5.2**.

will allow for the development of more effective aziridination catalysts supported by strong σ-donors, such as NHCs.

In this manuscript, we report the first mechanistic study of aziridination catalysis on the tetracarbene iron system by modeling the reaction pathways of the first- and second-generation tetracarbene-iron catalysts using DFT, and corroborating the DFT results with new and previously reported experimental evidence. These results show that incorporation of boron atoms into the ligand backbone significantly accelerates iron-imide formation with the second-generation catalyst,[(^{BMe_2,Et}TC^{H})Fe] (**5.1**) compared to the first-generation catalyst, [(^{Me,Et}TC^{Ph})Fe(NCCH$_3$)$_2$](PF$_6$)$_2$ (**5.2**). In both catalysts the predicted iron(IV) imide intermediate has an effective Fe-N double bond. Calculations also strongly suggest that the iron imide directly reacts with alkene through an open-chain radical mechanism. The calculated results are consistent with associated experimental studies with stereoisomers of the aziridines. However, disparate activation energies between the two catalysts leads to different levels of stereoretention. Finally, the steric properties of the organic azide can lead to the preclusion of metallotetrazene formation, which in turn, allows for lower alkene loadings during catalysis.

5.3 Methods

The computational study of the catalyst was performed using DFT within the Gaussian09 quantum-chemistry software package.[154] The TPSSh exchange-correlation functional[155] was used in conjunction with the Ahlrichs def2-TZVPP basis set[156,157] to obtain electronic energies while free-energy corrections were obtained using the TPSS exchange-correlation functional[155] in conjunction with the def2-SVP basis set[156,157] and density fitting.[156,157] The functional was corrected for dispersion using Grimme's D3 empirical dispersion scheme[158] with Becke-Johnson damping parameters.[159] The method used in the present work was selected due to its accurate description of geometric properties and calculated spin multiplicity of **5.1**, as well as computational efficiency. Catalyst **5.1** has 59 atoms and 240 electrons, while catalyst **5.2** has 127 atoms and 528 electrons after removing the counterions and axial acetonitrile ligands. All electrons of the catalysts, reactants, and products were treated explicitly in the calculations.

5.4 Results and Discussion

When aziridines are formed catalytically from organic azides and alkenes, metal imides are widely believed to be the key intermediates.[54,56,78,160] Gallo[77] and Ghosh[64] employed DFT to investigate the mechanisms of imide formation and subsequent aziridination by Ru- and Co-based porphyrin catalysts, respectively. Notably, the imide intermediates in these porphyrin systems were not isolated. In both catalytic systems that we have studied (**5.1** and **5.2**), no imide intermediates have been isolated despite extensive investigations.[56,58] Conversely, there are numerous examples of stable imides on Fe, Ru, and Co formed *via* organic azides, but these imides generally do not perform catalytic aziridination.[8,161–167] The notable exceptions to this observation are a Ru(VI) diimide isolated by the Che group and an Fe(III) radical imide isolated by the Betley group, both of which perform aziridination.[71,168]

Virtually all aziridination catalysts for organic azides (N_3R) are only effective with aryl azides and not alkyl azides. For example, Ceneni's and Zhang's Ru and Co porphyrin systems only react with aryl azides.[66,150] In the present study, catalyst **5.1** reacts with both aryl and

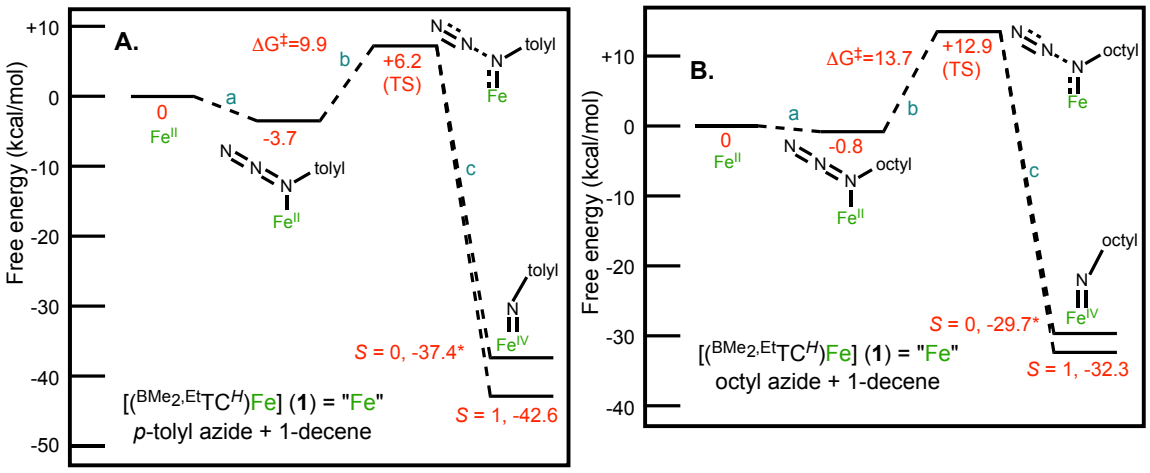


Figure 5.2: DFT-computed free-energy pathway for formation of imide from reaction between an organic azide and **5.1**. All species are in $S = 1$ (triplet) spin state unless designated with an * in which case they are in S = 0 (singlet) spin state. TS designates a transition state. A.) Depicts reaction between *p*-tolyl azide and **5.1**. B.) Depicts reaction between *n*-octyl azide and **5.1**. Free energies (ΔG) are given in kcal/mol.

alkyl azides, but **5.2** reacts catalytically only with aryl azides.[56,58] Since no imides have been isolated, DFT can assist in understanding the difference in reactivity between the two NHC systems and elucidating how the key intermediate is formed. We have computed three important steps of the catalytic pathways using DFT to understand how the aziridination mechanism operates for catalysts **5.1** and **5.2** and analyze some of the critical differences between them. These steps are (a) formation of the iron imide, (b) formation of aziridine from the iron imide, and (c) formation of a metallotetrazene. All calculations were performed using *p*-tolyl azide as the aryl azide, *n*-octyl azide as the alkyl azide, and 1-decene as the alkene.

5.4.1 Formation of iron imides - Step A

The first test case was studied between *p*-tolyl azide and **5.1** (Figure 5.2A). In this system, the lowest-energy spin state of all intermediates and transition states was $S = 1$, *i.e.*, a spin triplet. An iron imide could be formed through initial binding of the α-nitrogen or γ-nitrogen of the azide to the catalyst, so both intermediates were investigated.[65,169–172] Similar to Co and Ru systems, the energy of the α-bound intermediate was lower than that of the

γ-bound case.[64,77,173] The free energy of activation for formation of the imide from the α-bound intermediate was calculated to be $\Delta G^{\ddagger} = 9.9$ kcal/mol, suggesting that the formation of imide *via* this route is highly facile at room temperature (rt) (no route to an imide was found for the γ-bound case). This low free-energy barrier is consistent with experimental results that show reactivity of organic azides with **5.1** at rt (See discussion on tetrazenes, Section 5.4.3). The formation of the imide from **5.1** and *p*-tolyl azide is highly exergonic ($\Delta G = -42.6$ kcal/mol).

The reaction of *n*-octyl azide with **5.1** yielded similar results for imide formation as that of *p*-tolyl azide with **5.1** (Figure 5.2B). The ground spin state of all species in the pathway was a triplet. The α-bound azide intermediate was energetically more stable than the γ-bound azide intermediate. The free energy of activation to form the imide ($\Delta G^{\ddagger} = 13.7$ kcal/mol) was greater than that for the *p*-tolyl-azide case ($\Delta G^{\ddagger} = 9.9$ kcal/mol), but lower than corresponding energies for imide formation from other reactive organic azides reported by Ghosh and Gallo.[64,77] Experimental results show that *n*-octyl azide also reacts with **5.1** at room temperature, albeit quite slowly. In this case, the formation of the imide intermediate from azide and catalyst is also very exergonic ($\Delta G = -32.3$ kcal/mol), but less so than imide formation from **5.1** and *p*-tolyl azide.

An analysis of the calculated imide intermediates with $S = 1$ ground states demonstrates why these species are effective for aziridination. The imide intermediate for **5.1** with *p*-tolyl azide ($S = 1$) has a bond order of two between the iron and nitrogen. The calculated Fe-N bond distance is 1.72 Å and the Fe-N-C bond angle is 144.5°. While the bond distance is within the range of stable iron imides, the bond angle would be one of the tightest angles recorded for an iron imide.[163,168,174] A bond order of two is consistent with an analysis of the populated orbitals, which show a fully populated d_{xy} (non-bonding) and two singly populated π-antibonding orbitals that align with the Fe-N bond (Figure 5.3). Therefore, this iron imide would be more reactive than the more typical iron imides that have a bond order of three.[175,176] Other calculated imide intermediates from this set of iron complexes with $S = 1$ ground states had similar bond metrics and molecular-orbital diagrams.

The differences between **5.1** and **5.2** become apparent when comparing the free-energy diagrams for the reactions of the two catalysts with *p*-tolyl azide (Figures 5.2A and 5.4A).

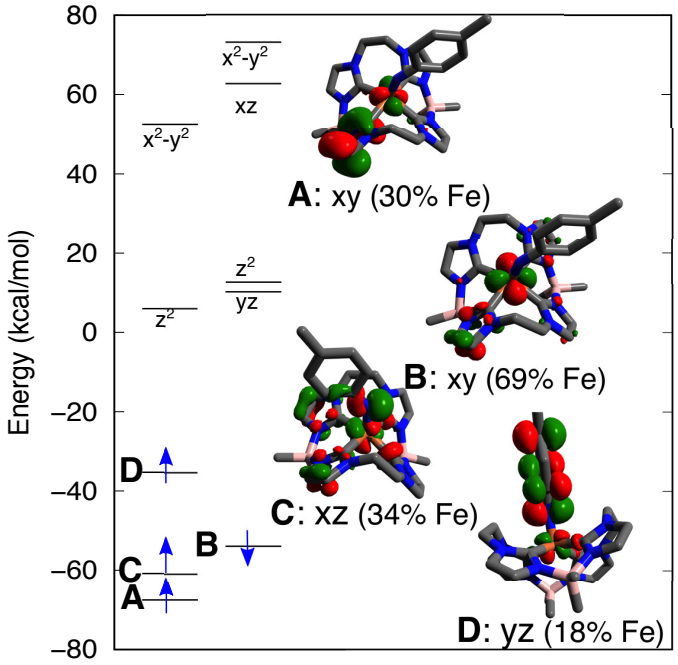


Figure 5.3: Energies, orbitals, and occupancies from DFT of the Fe d-orbital splitting of [(^{BMe_2},^{Et}TC^{H})Fe=N(tolyl)]. The zero of energy is set equal to the average energy of the d-orbitals of Fe. Canonical orbital surfaces are shown overlaying optimized molecular structures calculated with an isovalue of 0.04 with hydrogen atoms removed for clarity.

The free energy of activation to form the imide from the α-bound *p*-tolyl azide of **5.2** was calculated to be $\Delta G^{\ddagger}$ = 14.9 kcal/mol, and this value is similar to activation energies for systems that have been studied by Gallo and Ghosh.[64,77] The greater free energy of activation for imide formation from *p*-tolyl azide using **5.2** compared to **5.1** ($\Delta G^{\ddagger}$ =14.9 kcal/mol versus $\Delta G^{\ddagger}$ = 9.9 kcal/mol) is corroborated by their experimental reactivity. While **5.1** reacts with *p*-tolyl azide rapidly at room temperature, **5.2** only reacts with *p*-tolyl azide at 40 °C.[78]

Similar to the case with **5.1**, in reactions with **5.2**, the free energy of activation to form the imide is greater for the alkyl azide ($\Delta G^{\ddagger}$ = 18.7 kcal/mol) than for the aryl azide ($\Delta G^{\ddagger}$ = 14.9 kcal/mol) (Figure 5.4). Only the α-bound azide was calculated to be stable in reactions of aryl and alkyl azides with **5.2**. In the case of *n*-octyl azide reacting with **5.2**, the iron imide was calculated to have an $S = 0$ ground state, although the free-energy gap between the $S = 0$ and $S = 1$ spin states of the imide was calculated to be only ΔG = 0.5 kcal/mol suggesting that both spin states would be populated.

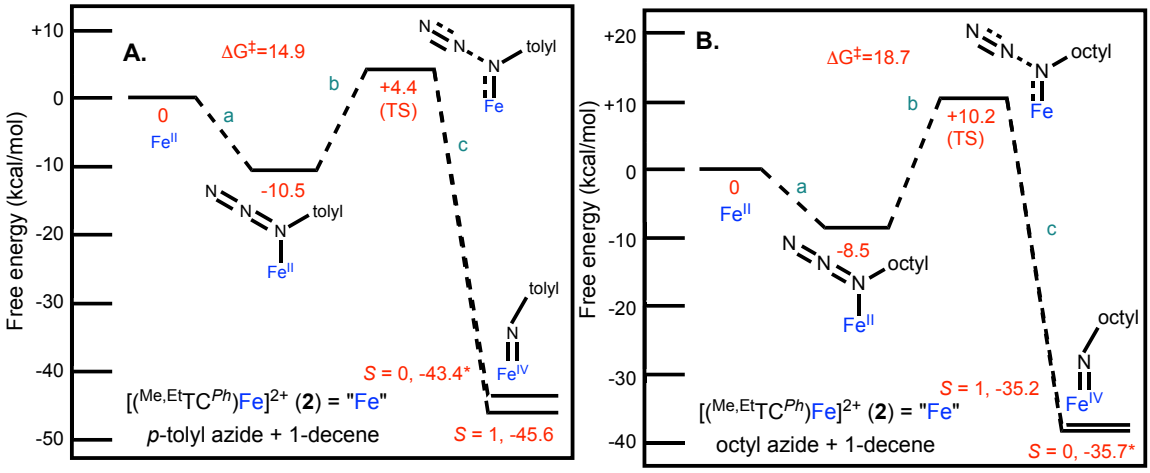


Figure 5.4: DFT-computed free-energy pathway for formation of imide from reaction between an organic azide and **5.2**. All species are in $S = 1$ (triplet) spin state unless designated with an * in which case they are in S = 0 (singlet) spin state. TS designates a transition state. A.) Depicts reaction between *p*-tolyl azide and **5.2**. B.) Depicts reaction between n-octyl azide and **5.2**. Free energies (ΔG) are given in kcal/mol.

The computational results in Figures 5.2 and 5.4 show that the free energy of activation for imide formation increases by $\Delta\Delta G^{\ddagger} = 5.0$ kcal/mol when the catalyst is changed from **5.1** to **5.2** using the same azide, and by $\Delta\Delta G^{\ddagger} = 3.8$ kcal/mol when the azide is changed from *p*-tolyl azide to octyl azide using the same the catalyst. Calculation of the Boltzmann factor ($\exp(\Delta\Delta G^{\ddagger}/RT)$) shows that changing the catalyst from **5.1** to **5.2** reduces the rate constant of imide formation by a factor of 4624 at rt (a factor of 1242 at 80 °C), whereas changing the azide from *p*-tolyl azide to octyl azide reduces the rate constant of imide formation by a factor of 610 at rt (a factor of 224 at 80 °C). A comparison of Figures 5.2A versus 5.4A and 5.2B versus 5.4B shows that the increase in free energy of activation upon change of catalyst from **5.1** to **5.2** occurs primarily due to the decrease in free energy of the α-bound intermediate. The Fe center in doubly-positively-charged **5.2** is more electron deficient than the Fe center in charge-neutral **5.1** and is more strongly attracted to the α-nitrogen lone pair of the azide, thereby forming a significantly more stable α-bound intermediate that requires a greater activation energy to dissociate into an imide and N_2. In contrast, a comparison of Figures 5.2A versus 5.2B and 5.4A versus 5.4B shows that the increase in free energy of activation upon change from *p*-tolyl azide to octyl azide occurs because the transition state

to form the imide, which oxidizes Fe(II) to Fe(IV), is stabilized by the more electron-donating *p*-tolyl group compared to the *n*-octyl group.

The greater free energy of activation for imide formation from alkyl azide versus aryl azide using **5.2** is consistent with experimental results. Compound **5.2** is not an active catalyst with alkyl azides in the presence of excess alkenes (the conditions that are necessary for aryl azides). Furthermore, reactions with *n*-octyl azide and **5.2** show limited direct reactivity. A reaction with *n*-octyl azide and **5.2** in toluene showed no reactivity even up to 80 °C. A similar reaction in acetonitrile showed no reaction at room temperature and only a partial reaction, *via* the imide to the expected metallotetrazene, at 80 °C. The combination of a less effective catalyst for imide formation and a greater activation energy for alkyl azides versus aryl azides demonstrates why this combination is ineffective for aziridination.

5.4.2 Formation of aziridines - Step B

While a metal imide is thought to be a key intermediate in $C_2 + N_1$ aziridination with organic azides, the steps upon addition of alkene to form the aziridine are less well understood. The two leading candidates are a concerted reaction that goes through an azametallacyclobutane intermediate, and a radical pathway that goes through a pair of single electron transfers. The Ghosh and Gallo groups have supported radical pathways for the Co porphyrin and Ru porphyrin systems, respectively, for aziridination, while, to date, no one has provided definitive evidence that a "box" intermediate is favorable.[64,77] Since our macrocyclic systems are more flexible than porphyrins and we previously synthesized metallotetrazenes, we have evaluated both pathways for an azide and alkene that form aziridines with our catalysts.[78]

The first test reaction was computed between the *p*-tolyl imide of **5.1** and 1-decene (Figure 5.5). This combination was chosen because we have previously reported that this permutation of azide and alkene yielded the expected aziridine, 2-octyl-1-(*p*-tolyl)aziridine, in 95% yield.[58] Calculations showed that the spin-triplet pathway was the minimum-energy pathway for the reaction. The formation of aziridine can conceivably proceed through two intermediates, an azametallacyclobutane intermediate and an open-chain-radical intermediate. The box intermediate strictly preserves the stereochemistry of the alkene in the resulting aziridine, whereas the chain intermediate can change the

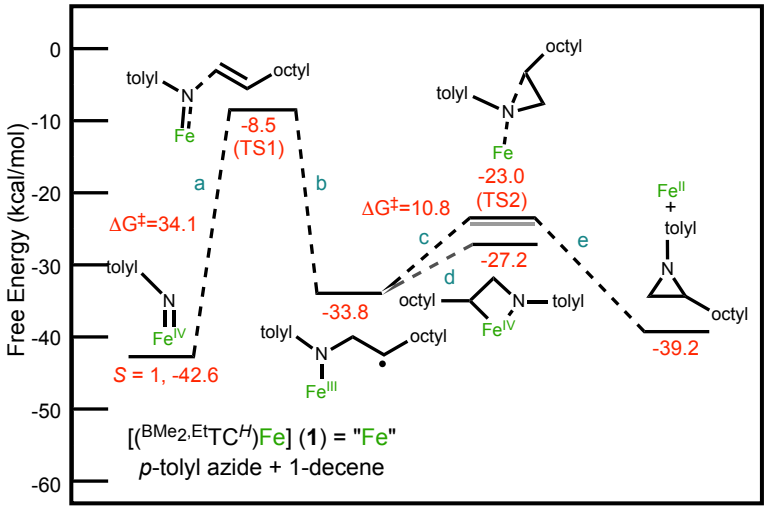


Figure 5.5: DFT-computed free-energy pathway for formation of aziridine from *p*-tolyl imide and 1-decene using catalyst **5.1**. All species are in $S = 1$ (triplet) spin state. TS designates a transition state. Free energies (ΔG) are given in kcal/mol.

stereochemistry *via* intramolecular rotation prior to the ring closing. Therefore, an important goal of our computational study was to compare the chain-mediated and box-mediated pathways to examine the stereochemical retention by the catalyst. The free energy of activation (TS1) to form the open-chain-radical or "bridge" intermediate from the imide was calculated to be $\Delta G^{\ddagger} = 34.1$ kcal/mol, whereas the activation energy to form the box intermediate from the imide was calculated to be >50 kcal/mol. Such a large activation energy for box formation from the imide suggests that the box intermediate is inaccessible through this reaction. The free-energy gap between the box intermediate and the bridge intermediate is relatively small ($\Delta G = 6.6$ kcal/mol) due to the flexible nature of the macrocyclic tetracarbene ligand. Since the box intermediate can be accessed *via* the chain intermediate, we calculated transition states to form the aziridine from either intermediate. We found that while the free energy of activation to form the aziridine from the open-chain intermediate (TS2) is $\Delta G^{\ddagger} = 10.8$ kcal/mol, the activation energy to form the aziridine from the box intermediate is >40.0 kcal/mol. Notably, Ghosh and Gallo both reported no energy barriers for the formation of aziridine in their porphyrins systems.[64,77]

These calculations of the transition states and intermediates yield two primary conclusions about the mechanism. First, the reaction proceeds solely through a radical mechanism of one-electron reductions without employing a box intermediate. Second, the

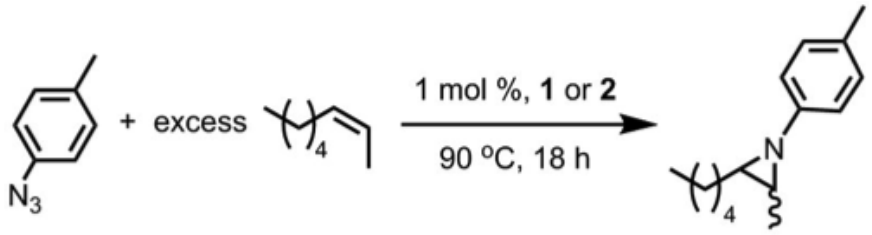


Figure 5.6: General catalytic reaction.

rate-determining step for the reaction is addition of alkene to the iron imide. This conclusion is distinct from the previously studied porphyrin systems where the rate-determining step is the addition of organic azide to the porphyrin. It is supported by the experimental finding that azides react with **5.1** at room temperature, but the aziridination only occurs if the reaction is heated. Finally, the presence of an energy barrier to form the aziridine from the open-chain-radical intermediate suggests that there could be chiral scrambling if the activation energy for intramolecular rotation of the intermediate about the pro-chiral center is similar to the activation energy for transformation to aziridine. The free energy of activation for intramolecular rotation was calculated to be $\Delta G^{\ddagger} = 10.4$ kcal/mol (Figure 5.5, pink line), which is very similar to the free energy of activation for formation of aziridine ($\Delta G^{\ddagger} = 10.8$ kcal/mol), strongly suggesting that there will be considerable chiral scrambling of the product aziridine. Importantly, the calculated free energy of the rotated bridge intermediate was almost the same as that of the initial bridge intermediate, and it is assumed that the activation energies to form aziridine from the two bridge intermediates are either the same or very similar. Of course, the competition between free energies of activation for aziridine formation versus intramolecular rotation is sensitive to the nature of the alkene. For example, we expect greater stereoretention with sterically bulkier alkenes, such as 2-octene, due to a greater activation energy for intramolecular rotation.

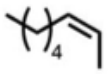
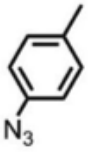
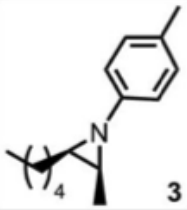
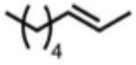
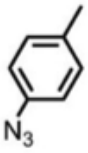
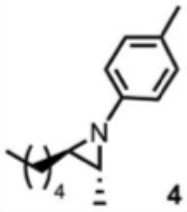
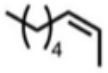
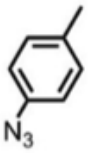
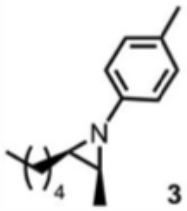
A second test reaction was computed between the *p*-tolyl imide of **5.2** and 1-decene (Figure 5.7), following the same open-chain radical (bridge) pathway as that for catalyst **5.1**. The free energy of activation to form the bridge intermediate from the imide was calculated to be $\Delta G^{\ddagger} = 25.3$ kcal/mol, which is considerably less than the corresponding imide-to-bridge free energy of activation of $\Delta G^{\ddagger} = 34.1$ kcal/mol for **5.1**. The free-energy gap between the box intermediate and the bridge intermediate is even smaller for **5.2** (ΔG

= 1.3 kcal/mol) than for **5.1** (ΔG = 6.6 kcal/mol) due to the even more flexible nature of the macrocyclic ligand. Critically, the free energy of activation to form the aziridine from the bridge intermediate is just $\Delta G^{\ddagger}$ = 4.1 kcal/mol, compared to the corresponding free energy of activation of $\Delta G^{\ddagger}$ = 10.8 kcal/mol for **5.1**. The intramolecular rotational barrier was calculated to be $\Delta G^{\ddagger}$ = 10.5 kcal/mol (Figure 5.7, pink line), which is very similar to the corresponding barrier of $\Delta G^{\ddagger}$ = 10.4 kcal/mol for **5.1**. These results predict that **5.2** should show greater stereochemical control on azirdine formation than **5.1**. Similar to **5.1**, the rate-determining step in **5.2** is the addition of alkene to the iron imide.

To experimentally test the results of the DFT calculations, we ran a series of reactions that yield distinct stereoisomers. A general reaction is shown in Figure 5.6. Depending on the mechanism of aziridination, we would expect the stereochemistry to be fully retained, partially retained, or fully lost. Test reactions included *cis*-2-octene and *trans*-2-octene with both catalysts **5.1** and **5.2**. Except for a single study by the Betley group using *cis*-β-deuterostyrene, no one has experimentally probed these mechanisms through product distribution with organic azides and *cis* and *trans* alkenes.[177]

Initial tests focused on reactions of **5.1** with *cis*-2-octene and *trans*-2-octene. The reaction of neat *cis*-2-octene, *p*-tolyl azide and 1% **5.1** as catalyst yielded two recoverable products that were separated by careful gradient elution of ethyl acetate and hexanes over silica gel. ^{1}H and ^{13}C NMR showed only modest differences between the two species with the primary distinctions between 1.5-2.2 ppm in the ^{1}H NMR. COSY and HSQC confirmed that the two peaks for the major product at 2.03 ppm and 2.16 ppm in the ^{1}H NMR were the expected single protons off the aziridine ring. In a similar manner, the minor product's peaks at 1.91 ppm and 2.15 ppm correspond to the protons on an aziridine ring, which would be the alternate stereoisomer. To distinguish between *syn* aziridine and *anti* aziridine, we employed homonuclear decoupling NMR to compare the coupling between the two protons on the aziridine ring.[177–180] The major product showed coupling constants of J = 6.6 Hz and 6.5 Hz, while the minor product showed coupling constants of J = 2.3 Hz and 2.0 Hz. The larger coupling constants are consistent with a *syn* aziridine, while the smaller values are consistent with an *anti* stereochemistry.[68,177,181–183] We thus assigned the major product

Table 5.1: Aziridination reactions with **5.1** and **5.2**.

Entry	Alkene	Azide	Catalyst	Aziridine	Yield
1			1		**3**: 67% **4**: 28%
2			1		**3**: 12% **4**: 58%
3			2		**3**: 24% **4**: 0% **3**: 44%[a] **4**: 7%[a]

a = reaction run over 6 days

as *syn*-2-methyl-3-pentyl-1-(*p*-tolyl)aziridine (**5.3**) and the minor product as *anti*-2-methyl-3-pentyl-1-(*p*-tolyl)aziridine (**5.4**). The isolated yields for **5.3** and **5.4** were 67% and 28%, respectively, which gives a total yield of 95% (Table 5.1, Entry 1). The d.r. for this reaction is 2.4:1.

The reaction of neat *trans*-2-octene, *p*-tolyl azide and 1% **5.1** yielded the same two products, albeit in lower yield. In this case, **5.3** was formed in 12% yield, while **5.4** was formed in 58% yield, giving a total yield of 70% (Table 5.1, Entry 2). The d.r. for this reaction is 4.8:1.

In both *cis* and *trans* alkene with catalyst **5.1**, the expected diastereomer was the major product, but a considerable amount of the opposite diastereomer was produced. Since the stereochemistry would be retained if the azametallacyclobutane was the sole intermediate formed by reaction with alkene, these results confirm that aziridination occurs *via* the radical open-chain mechanism, in qualitative agreement with results from DFT. Intramolecular rotation of the radical intermediate prior to aziridine formation will result in formation of the

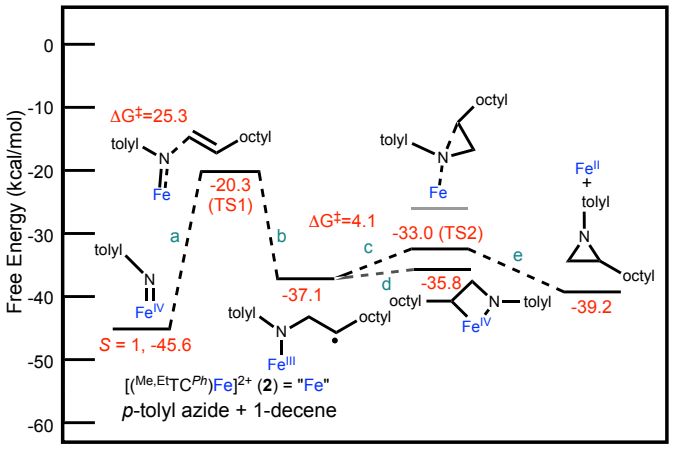


Figure 5.7: DFT-computed free-energy pathway for formation of aziridine from *p*-tolyl imide and 1-decene using catalyst **5.2**. All species are in $S = 1$ (triplet) spin state. TS designates a transition state. Free energies (ΔG) are given in kcal/mol.

opposite diastereomer. As expected for this type of mechanism, the *trans* case leads to greater retention of stereochemistry since there is less steric repulsion in the radical intermediate.

We repeated the same two reactions with the *cis* and *trans* 2-octene with **5.2**. After 18 hours, which was the complete reaction time for catalyst **5.1**, the reaction was not complete with *cis*-1-octene (as determined by following consumption of organic azide), but only one aziridine product was detected. Aziridine **5.3** was isolated in 24% yield showing complete retention of stereochemistry (Table 5.1, Entry 3). A second reaction was run for six days to ensure that all organic azide reacted. In this case, both **5.4** and **5.5** were produced in 44% and 7% yield, respectively (d.r. ratio of 6.3:1). This is much improved stereocontrol and at low reaction times there is very high d.r. Regrettably, test reactions with *trans*-2-octene did not yield sufficient aziridine for analysis of products, which is not surprising, since **5.2** is a less reactive catalyst than **5.1** as observed experimentally.[56] These results support the DFT calculations, which show that going through an open-chain radical intermediate is acceptable for stereochemical control provided the activation energy for radical recombination to form aziridine is much lower than the activation energy for rotation-induced chiral scrambling.

Our combined theoretical and experimental studies of Steps A and B reveal that while the rate of imide formation is faster with the second-generation catalyst (**5.1**) than with the first-generation catalyst (**5.2**), the rates of imide reaction with alkene and subsequent aziridine formation are faster with the first-generation catalyst than with the second-generation

catalyst. A faster rate of imide formation makes a catalyst reactive with both aryl and alkyl azides, whereas a faster rate of aziridine formation from the open-chain radical intermediate enhances stereochemical control on the product. Both differences between the two catalysts arise because the Fe(II) center in doubly-positively-charged **5.2** is more electron deficient than in charge-neutral **5.1**. In Step A, **5.2** forms more stable α-bound azides than **5.1** that require more energy to dissociate into iron imides and nitrogen molecules. In Step B, the imide of **5.2** undergoes alkene addition (reduction of Fe(IV) to Fe(III)) and subsequent radical recombination faster than the imide of **5.1**. The significantly more facile radical recombination in **5.2** compared to **5.1** is evident in the calculated distance between the ring-closing carbon and nitrogen atoms (C-N) in the TS2 transition states of Figures 5.6 and 5.7. The C-N distances are 2.50 Å and 2.51 Å in the open-chain radical intermediates of **5.1** and **5.2**, respectively, and 1.46 Å in the product aziridine. Notably, the C-N distance is 2.00 Å in TS2 of **5.1** and 2.21 Å in TS2 of **5.2**, demonstrating that TS2 of **5.2** is a significantly earlier transition state than TS2 of **5.1** and consequently has a much lower activation energy. One approach to developing the next-generation tetracarbene-iron catalyst that accelerates imide and aziridine formations more equally might be to modify **5.1** using electron-withdrawing substituents such that the electron density at the Fe center is less than that in **5.1** but more than that in **5.2**.

5.4.3 Formation of metallotetrazenes - Step C

The reaction to form aziridine from the metal-imide intermediate is complicated by a competing reaction, the formation of metallotetrazene *via* addition of a second equivalent of organic azide (Figure 5.1). The metallotetrazene forms through a formal [2+3] cycloaddition reaction between the metal imide and organic azide.[184,185] While previous iron tetrazenes prepared by Riordan[186] and Holland[185] were not reactive, our first-generation catalyst forms a metallotetrazene that can reform the catalyst and yield diazene.[78] Preventing this competing reaction is critical for effective catalysis, particularly for expensive alkenes. Therefore, we investigated the mechanism of metallotetrazene formation through DFT calculations. These DFT calculations motivated a series of experiments that suggest possible ways to prevent the formation of metallotetrazene.

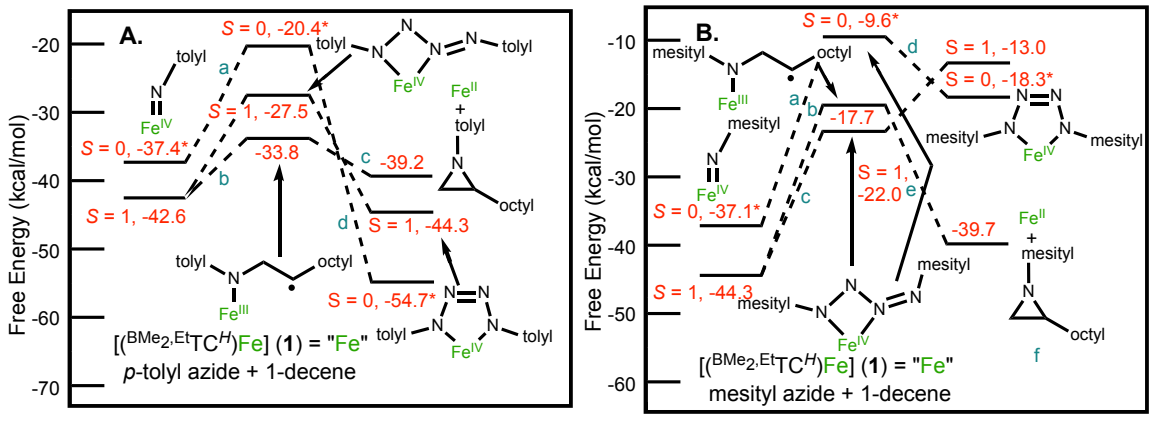


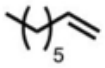
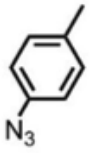
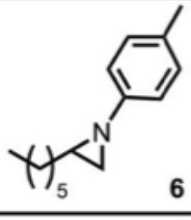
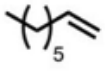
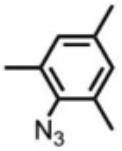
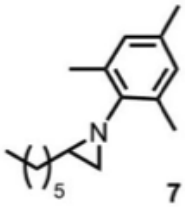
Figure 5.8: DFT-computed free-energy pathway for formation of tetrazene from *p*-tolyl azide and mesityl azide with **5.1**. All species are in S = 1 (triplet) state unless designated with an * in which case they are S = 0 (singlet) spin state. Free energies (ΔG) are given in kcal/mol. A.) Depicts reaction between *p*-tolyl azide and **5.1**. B.) Depicts reaction between mesityl azide and **5.1**.

Calculations for the second-generation catalyst (**5.1**) with *p*-tolyl azide show why excess alkene is necessary for this pairing. While formation of the metallotetrazene from the iron imide releases much more energy than formation of the aziridine from the same iron imide (Figure 5.8A) ($\Delta\Delta G = -5.1$ kcal/mol in favor of forming the metallotetrazene compared to aziridine for the *p*-tolyl case with 1-decene), the intervening open-chain-radical intermediate that proceeds to aziridine is more stable by $\Delta G = -6.3$ kcal/mol than the intervening metallotriazetidine intermediate that proceeds to metallotetrazene. Consequently, the reaction can be driven to form aziridine over tetrazene by employing a considerable excess of alkene during catalysis. The corresponding higher-energy spin singlet pathway to metallotetrazene was also calculated and showed that while the net formation of metallotetrazene from the imide was highly exergonic ($\Delta G = -17.3$ kcal/mol compared to $\Delta G = -1.7$ kcal/mol in the spin-triplet pathway), the formation of the intervening metallotriazetidine intermediate from the imide was highly endergonic ($\Delta G = 17.0$ kcal/mol compared to $\Delta G = 6.3$ kcal/mol in the spin-triplet pathway). The relative energies of aziridination and metallotetrazene formation will, of course, depend on the nature of the azide and alkene. Very little research on the mechanism of formation of metallotetrazenes has been conducted,[184,187–189] and to our knowledge, the metallotriazetidine structure has not been previously postulated as an intermediate to a metallotetrazene. Notably, the bond

distances around the metallotriazetidine are consistent with single bonds. The ground state of this intermediate is also in a triplet spin state with two electrons on the iron in the same manner as the imide complex, suggesting that the oxidation state remains at Fe(IV). As a test for the DFT results, we reacted *p*-tolyl azide with **5.1**. This reaction formed the tetrazene, [(^{BMe_2,Et}TC^{H})Fe((*p*-tolyl)N$_4$(*p*-tolyl))] (**5.5**). Complex **5.5** is a distorted trigonal prismatic complex and spectroscopically similar to our previously reported Fe(IV) tetrazene with the first-generation catalyst.[78]

These results suggested that destabilizing the tetrazene relative to formation of aziridine may allow for lower loading of alkene by shutting off the path to metallotetrazene formation. We postulated that a bulkier organic azide would be one manner of achieving this outcome. DFT calculations were performed for a reaction pathway with **5.1**, mesityl azide, and 1-decene (Figure 5.8B). The same intermediates were calculated for the formation of aziridine and metallotetrazene. The free-energy profile in Figure 5.8B is qualitatively different than the free-energy profile in Figure 5.8A because the formation of the tetrazene complex with mesityl azide is strongly endergoinc (ΔG = 31.3 kcal/mol relative to the corresponding iron imide) whereas the analogous formation of the tetrazene complex with *p*-tolyl azide is exergonic (ΔG = $-$1.7 kcal/mol). In both cases, the formation of aziridine from the iron imide is similarly endergonic (ΔG = 3.4 kcal/mol for *p*-tolyl azide and ΔG = 4.6 kcal/mol for mesityl azide). Therefore, while the formation of tetrazene competes with formation of aziridine in the case of *p*-tolyl azide, it does not compete with formation of aziridine in the case of mesityl azide. This computational predictions was verified by experiments, which shows that no tetrazene complex is formed from addition of mesityl azide and **5.1**. If there is no competition reaction during aziridination catalysis, then the formation of aziridine should be feasible using a lower loading of alkene. To test this hypothesis, we ran catalytic reactions with **5.1**, 1-octene, and either *p*-tolyl azide or mesityl azide. A catalytic reaction of neat 1-octene, *p*-tolyl azide and 1% loading of **5.1** (versus azide) yielded the expected aziridine, 2-hexyl-1-(*p*-tolyl)aziridine (**5.6**), in 91% isolated yields after purification with column chromatography (Table 5.2, Entry 1). This high yield for a primary alkene is consistent with yields from our previous research with **5.1**.[58] However, reducing the alkene loading to five equivalents of alkene and running the reaction in toluene led to an isolated yield of only 32%. In contrast, when mesityl

Table 5.2: Aziridination reactions with **5.1**.

Entry	Alkene	Azide	Catalyst	Aziridine	Yield
1			1	 **6**	91%[a] 32%[b]
2			1	 **7**	45%[a] 44%[b]

a = reaction run with excess alkene
b = reaction run with 5 equivalents of alkene with toluene as solvent

azide was employed with excess alkene, 2-hexyl-1-mesitylaziridine (**5.7**) was formed in 45% isolated yield (Table 5.2, Entry 2). But in this case, lowering the loading to five equivalents of 1-octene produced **5.7** in 44% yield, which is effectively no lower than using excess alkene. Thus, experiments confirm that a bulkier organic azide prohibits the competition reaction and makes the reaction more effective with lower alkene loading due to destabilization of the metallotetrazene relative to aziridine formation.

5.5 Conclusions

We have investigated three steps of the catalytic aziridination cycle with macrocyclic tetracarbene iron catalysts, organic azides, and alkenes. By performing a detailed computational study of the reaction pathways of two tetracarbene iron catalysts using DFT calculations and experimentally testing the results, we can deduce some of the key elementary steps of the cycle. The first key step is the formation of an iron-imide intermediate. The calculations also show that the pathway goes through an α-bound azide and direct loss of N_2. The calculated energy barriers for imide formation using **5.1** are lower than those for **5.2** , and much lower than other aziridination catalysts and are consistent with the experimental results that organic azides react at room temperature.

The second key step is the formation of the aziridine from the iron imide. The addition of alkene to imide is the rate-determining step for our system, which is contrary to porphyrin systems where the addition of azide is the rate-determining step. One additional question was whether this step proceeded through a radical pathway, which could lose stereochemical information, or through a box pathway, which would retain the stereochemistry. Both DFT calculations and experimental results show that the radical pathway is favored for both catalysts. The key experimental result is that *cis* and *trans* isomers of 2-octene form both the *syn* and *anti* aziridines. DFT calculations show that the rotational free-energy barrier for the open-chain-radical intermediate has roughly the same height as reductive elimination for **5.1**. However, catalyst **5.2** does not show loss of stereochemistry for the same reactions and this experimental result is supported by calculations that show a lower free-energy barrier for reductive elimination to give aziridine. Keeping this barrier low for the ring-closing step is critical for effective stereocontrol in this catalytic reaction and a key insight for aziridines.

Finally, the aziridination reaction is in competition with the formation of a metallotetrazene. It is critical to prevent the formation of this species for effective use of high-value alkenes. DFT results for **5.1** and *p*-tolyl azide show that the overall transformation of the iron imide to metallotetrazene is much more exergonic than the corresponding transformation to aziridine, but the intervening open-chain radical intermediate to aziridne formation is more stable than the intervening metallotriazetidine intermediate to tetrazene formation. Notably, increasing the steric bulk of the organic azide flips the relative stability of product aziridine and metallotetrazene, vastly favoring the formation of aziridine. This calculation is corroborated by experimental results that show no tetrazene is formed when mesityl azide is used, and lower alkene loading is as effective as excess alkene during catalysis with mesityl azide. These combined computational and experimental results will allow us to develop the next generation of aziridination catalysts supported by macrocyclic tetracarbene ligands as well as provide important chemical insight into the performance of first-row transition metals for catalytic aziridination.

Chapter 6

Chiral iron-tetracarbene catalysts for stereoselective aziridination

6.1 Disclosure

This work have been done in conjunction with experiments performed by the group of David Jenkins. Several undergraduate research students have contributed to these calculations including Daniel Hendrix who contributed to the work discussed in Section 6.4.1, and Conner Masteran and Trell Stroud who contributed to the work discussed in Section 6.4.2.

6.2 Introduction

Many natural and biological products, including sugars, amino acids, and proteins, are chiral molecules. As a result of this inherent chirality in nature, it has been found that only one stereoisomer of many pharmaceutical compounds are active for the intended target.[190] For example, ibuprofen is sold as a racemic mixture of both the R- and S-enantiomers; however, only the S-enantiomer is active toward inflammation reduction.[191] While not the case with ibuprofen, there are occasions where the inactive enantiomer is toxic or reactive elsewhere in the body.[192] There has been a push in recent years to market only a single enantiomer in medications, either through separation techniques or by enantioselective synthesis.[193] For

this reason, we seek to design a catalyst that can not only favor aziridination at low alkene loading, as in Chapter 5, but one that is also stereoselective.

In Chapter 5, it was found that [(^{BMe_2},^{Et}TC^{H})Fe] showed promise as a new generation of iron-tetracarbene catalyst due to increased reactivity with both alkyl and aryl azides over previous generations and thermodynamic preference for aziridinaiton over formation of a metallotetrazene with the use of bulky azides. In this work, [(^{BMe_2},^{Et}TC^{H})Fe] was modified to include wings on the ethylene bridges of the macrocycle. The goal was to favor a specific isomer of the aziridine product and favor this aziridination over formation of metallotetrazene. Initially, the thermodynamic stability of the imide and tetrazene for four different catalysts were compared. A promising catalyst is one whose reaction profile goes downhill in moderate energy steps. The imide should be stable with respect to the bare catalyst but also less stable than the aziridine. Additionally, the aziridine should be thermodynamically favored over the metallotetrazene.

6.3 Methods

This study was performed using DFT within the Gaussian09 quantum-chemistry software package.[154] To compare the four modified catalysts, the same method as that outlined in Section 5.3 was used. The lowest-energy structure and free-energy corrections were calculated using the TPSS exchange-correlation functional[155] with the Ahlrichs def2-SVP basis set[156,157] and density fitting.[156,157] More accurate electronic energies were obtained using the hybrid TPSSh functional in conjunction with the def2-TZVPP basis set.[156,157] The TPSSh functional was corrected for dispersion using Grimme's D3 empirical dispersion[158] scheme with Becke-Johnson damping parameters.[159] All electrons of the catalysts, reactants, and products were treated explicitly in the calculations.

6.4 Results

As was discussed in Chapter 5, the [(^{BMe_2,Et}TC^{H})Fe] catalyst was reactive with both aryl and alkyl azides. Chapter 5 also showed that aziridination can be thermodynamically favored over

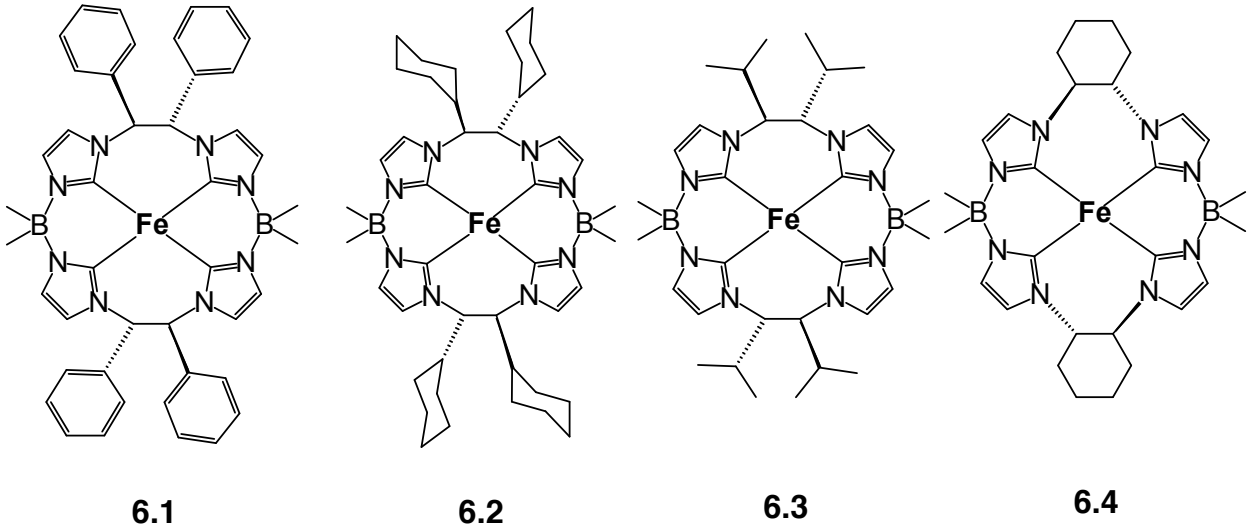


Figure 6.1: Chiral iron tetracarbene catalysts for aziridination investigated in the present study: [($^{BMe_2,(S,S')-diphenyl)_2-Et}$TC^{H})Fe] (**6.1**), [($^{BMe_2,(S,S')-dicyclohexyl)_2-Et}$TC^{H})Fe] (**6.2**), [($^{BMe_2,(S,S')-isopropyl)_2-Et}$TC^{H})Fe] (**6.3**)[($^{BMe_2,(S,S')-C_4H_8)_2-Et}$TC^{H})Fe] (**6.4**).

metallotetrazene formation when bulky azides are used without the need to include excess alkene in the reaction. While this improves the atom economy of the reaction, the need to use bulky azides limits the number of azides that can be effectively utilized for aziridination in the absence of high alkene loading. In Section 6.4.1, four different organometallic complexes have been considered. The stability of the imide relative to the bare catalyst, as well as the relative stability of the metallotetrazene and aziridine are compared.

6.4.1 Chiral iron-tetracarbene catalysts

The second-generation catalyst containing dimethyl-boron-bridging units in Chapter 5 showed great improvements over previous generations of catalyst. However, the stereochemical retention was decreased due to competition between aziridination and internal rotation in the radical intermediate. Four catalysts containing wings off the ethylene bridge of [(^{BMe_2,Et}TC^{H})Fe] were investigated. These wings were added such that the catalyst itself became a chiral species which should help steer the alkene, favoring formation of a single enantiomer of the aziridine product. The modified catalysts, shown in Figure 6.1, consist of phenyl, cylohexyl, and isopropyl wings, as well as a variation that contained a cyclohexyl ring which is fused to the macrocycle.

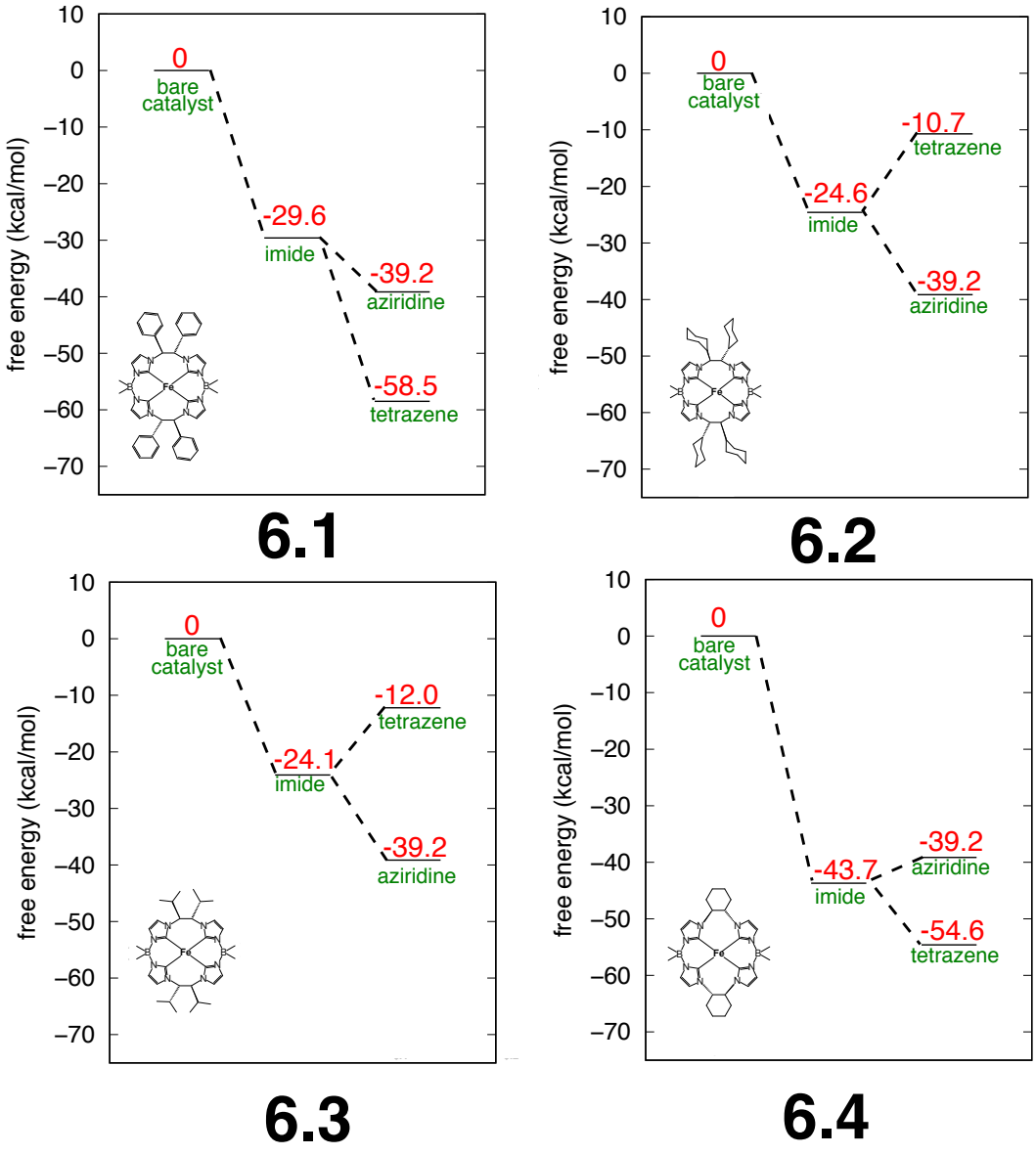


Figure 6.2: Free energies (kcal/mol) of key species along the reaction pathway to aziridine for the four variations of iron-tetracarbene catalysts given in Figure 6.1.

Prior to investigating the potential of each species for stereoselective aziridination, the thermodynamic stability of the bare catalyst, imide, tetrazene, and aziridine were compared to probe the atom economy of each catalyst, *i.e.* does the catalyst require high-alkene loading to favor aziridination. The aryl *p*-tolyl azide and 2,3,3-trimethylbutene were used as the nitrogen source and alkene, respectively. The ideal catalyst will react with azide to form a moderately stable imide compared to the bare catalyst and azide at infinite separation. This imide should also favor aziridination by reaction with alkene over metallotetrazene formation through reaction with a second equivalent of azide (Figure 5.1). As shown in Figure 6.2, only species **6.2** and **6.3** with cyclohexyl and isopropyl wings, respectively, yield such a profile. Both **6.1** and **6.4** form very stable metallotetrazene intermediates. In fact, the tetrazene species formed by these catalysts are more thermodynamically stable than that of the parent catalyst (ΔG=$-$54.7 kcal/mol). This would suggest aziridination would be more difficult for **6.1** and **6.4**. Larger alkene loadings would be needed to favor aziridination. Additionally, **6.2** and **6.3** form the least stable imide intermediates of all macrocycles considered in this work, including the parent catalyst (ΔG=$-$42.6 kcal/mol). Recall that this was one of the desired qualities of our chiral catalyst, as a metastable imide should readily react to form aziridine.

6.4.2 Mechanistic investigation of favored chiral catalyst

We not only seek to design a catalyst which steers alkenes, leading to a single binding geometry, but also that does not allow for stereochemical scrambling. One way this can be accomplished is by alkene reaction with the imide through a concerted intermediate. This is a rather complex mechanism, requiring multiple bonds to form and dissociate simultaneous. To date, no catalytic aziridination reactions have been shown to proceed through a concerted pathway. Stereochemical retention can also be enforced *via* the radical intermediate by decreasing the amount of time the species spends in this state or by preventing intramolecular rotation. The first of these can be accomplished by decreasing the activation energy required to form aziridine from the radical intermediate. Several catalysts have been reported to barrierlessly form aziridine in this way.[64,77] Furthermore, the activation energy for intramolecular rotation can be increased to prevent stereochemical

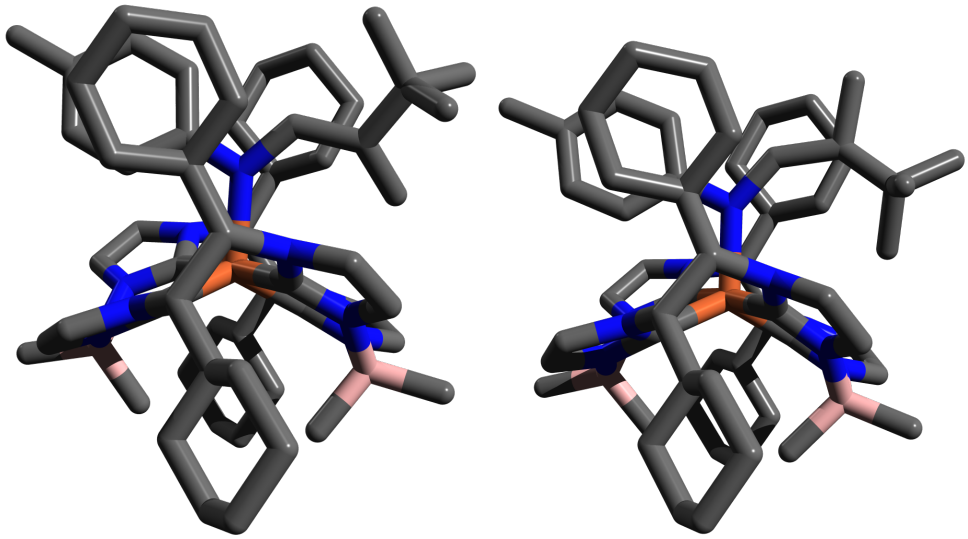


Figure 6.3: Possible bridge intermediates formed between the interaction of the cyclohexyl-winged imide (**6.2**) and 2,3,3-trimethylbutene. The two bridge intermediates differ only in the orientation of the methyl and *t*-butyl substituents relative to the macrocycle. On the left, the methyl substituent points toward the macrocycle while the *t*-butyl points toward the macrocycle on the right.

scrambling. We hypothesize this can be done not only by increasing the bulkiness of the alkene substituents but also by increasing the bulkiness of the wings on the macrocycle. For this reason, we have investigated the thermodynamic stability of radical intermediates with **6.2**, the more sterically hindered of the two promising catalysts.

To investigate the steering of alkene-approach to the imide of **6.2**, the stability of possible bridge intermediates using 2,3,3-trimethylbutene have been calculated. This molecule is highly asymmetric, suggesting different molecular geometries of the radical intermediate will have significantly different energies. These geometries, shown in Figure 6.3, differ in the orientation of the *t*-butyl substituent relative to the macrocycle of the imide. The free-energy gap of the two bridge-geometries is 20.6 kcal/mol. Thus, the bulky alkene with **6.2** does show steering, favoring a geometry where the methyl group rather than the bulkier *t*-butyl group points down toward the macrocycle. What is surprising is that these bridge intermediates are unstable with respect to the bare catalyst of **6.2**. Calculations for the radical intermediate of the parent catalyst showed a stable bridge species; however, the alkene used in Chapter 5 was 1-decene, a much smaller alkene than 2,3,3-trimethylbutene. Substituting this alkene with 2,3-dimethylbutene reduced the energy of the radical intermediate by 8 kcal/mol. Using

1-decene additionally stabilized the bridge (ΔG=+5.20 kcal/mol) though this species was still less stable than the bare catalyst, suggesting a radical intermediate would not be formed.

Since it was found that **6.3** also gave a favorable energy profile when the imide and metallotetrazene species were considered, the free energy of bridge intermediates with this catalyst were also calculated. Reducing the size of the alkene with **6.2** led to more stable bridge intermediates, though these species were all unstable with respect to the bare catalyst. We believe this increased stability was a result of lowered steric hinderance between the alkene and the cyclohexyl wings of the macrocycle. Thus, we expect bridges formed with **6.3** should be more stable than those formed by **6.2** due to the reduced size of the wings. However, this was not the case. The bridges formed from the reaction of **6.3** with 2,3,3-trimethylbutene, 2,3-dimethylbutene, and 1-decene had free energies of +14.9, +11.6, and -0.6 kcal/mol, respectively, compared to the bare catalyst.

6.5 Summary and Conclusions

In this work, we have investigated the relative thermodynamic stability of imide and metallotetrazene formed from four chiral iron-tetracarbene catalysts. This work sought to determine the propensity for atomically-economical and enantiomerically-selective aziridination. We have found two possible candidates for further consideration; however, additional calculations revealed steric repulsion between radical intermediates with three alkenes of varying bulkiness. This results was found for both variations of chiral catalyst with different sized wings on the macrocyclic backbone. Thus, our calculations show that if **6.2** and **6.3** are catalytic toward aziridination, they likely do not proceed through a radical intermediate.

Chapter 7

Summary and Conclusions

7.1 Interaction of atomic oxygen with Ag(111) and Ag(110)

In Chapter 2, the interaction of AO with both Ag(111) and Ag(110) surfaces was investigated using classical dynamics. This study looked at the effect of both coverage and temperature. While it was found that generally oxygen prefers to adsorb to sites which increase the number of nearest neighbors, the reactive potential could not well describe some behavior observed by *ab initio* calculations. For this reason, DFT calculations were performed, the results of which can be found in Chapters 3 and 4. These studies showed that on Ag(111), AO favors adsorption on the surface at low coverages while adsorption in the subsurface is favored at high coverages. It was found that this change in preference from surface to subsurface occurs at coverages similar to the saturation coverage of several experimentally observed surface reconstructions. These adsorption energies were then used to develop an adsorption model which can describe AO adsorption as a function of neighbor occupations. To compare the interaction of AO between Ag(111) and Ag(110), three coverages were investigated on the (110) facet, revealing interaction with AO is very different between the two surfaces with increasing coverage. Surface adsorption on Ag(110) was found to be favored at all coverages. Work functions were calculated for the favored surface, subsurface, and subsurface-23 sites on both facets of silver to probe the electronic structure of the catalyst. Both Ag(111)

and Ag(110) revealed work functions that were only sensitive to surface coverage. At all coverages, the work function on Ag(111) was larger than that on Ag(110). This indicates more O-O repulsion on the close-packed surface which is consistent with the results of our adsorption studies. This work significantly contributes to the field of epoxidation by silver surfaces due to the new understanding of O-O interactions on the catalytic surface at industrially-relevant coverages. This work can also be used as a foundation to build more complex models, some of which are discussed below.

While this work has given new insight into the interaction of AO with silver surfaces, especially the role of nearest-neighbor interactions on adsorption, it will serve as the groundwork for several ongoing projects in the group. Both the calculated adsorption energies, as well as the adsorption model will be used to develop a kinetic Monte Carlo (KMC) code which will give information about the distribution of oxygen between surface and subsurface not only at different coverages but various temperatures, as well. What is presently missing to complete the KMC algorithm is information about the kinetic barriers to oxygen diffusion. This will require calculating activation energies for oxygen movement vertically between layers in addition to laterally between sites in a single layer, both on the surface and in the subsurface. A second area of future focus lies in further understanding AO interactions with reconstructed surfaces. While the work reported in Chapter 3 can give some insight into what motivates surface reconstruction on Ag(111), it does not give any information as to how subsurface adsorption may change in the presence of such reconstructions. We plan to perform an adsorption study for AO in the subsurface of a $p(4\times4)$-reconstructed surface. The symmetry of the surface is changed from that of an unreconstructed surface and the surface-AO adsorption sites are known. This would allow not only understanding of the interaction of AO with the subsurface of a reconstructed surface, but also how the interaction changes in going from an unreconstructed to a reconstructed surface. Though subsurface oxygen does not appear to be favored at high AO coverages on Ag(110), we plan to further investigate this facet. We plan to perform a more extensive coverage investigation on Ag(110) which will allow an adsorption model to be developed for this surface. We are interested to see if the O-O cooperation seen on Ag(111) is surface

dependent or simply a result of placing charged AO anions in close proximity, with the surface acting only as an electron donor.

7.2 Aziridination *via* iron-tetracarbene catalysts

In Chapter 5, the mechanism of aziridination for two structurally-different generations of iron-tetracarbene catalysts was investigated. The first generation catalyst was reactive only with aryl azides while the second generation catalyst was reactive with both aryl and alkyl azides. Calculations revealed the free energy of activation was higher for the alkyl azide with both generations of catalyst. This activation energy was also consistently higher for the first generation catalyst. Thus, formation of the imide, a key intermediate in the reaction, was kinetically unfavorable for the first generation catalyst with alkyl azides. Our work also revealed both generations of catalyst formed aziridine through a radical-mediated pathway. The nature of the radical intermediate led to competition between aziridination and intramolecular rotation. The relative activation energies for these two processes could result in significant loss of stereochemistry. This was observed for the second generation catalyst, where the free-energy of activation between aziridination and rotation differed only by 0.3 kcal/mol. This gap was much larger for the first generation catalyst ($\Delta\Delta G^{\ddagger}$=6.4 kcal/mol), resulting in better stereochemical retention. This result was in qualitative agreement with experiment. Finally, we showed that the metallotetrazene of the second generation catalyst could be destabilized by using bulkier azides, reducing the required alkene loading for aziridination. In Chapter 6, this work was extended to chiral variations of the second generation catalyst. We found two catalysts that showed great potential for improved atom economy. Unfortunately, no stable radical intermediates could be found for these complexes. While this does not indicate that these complexes are not catalytic, it does suggest catalysis would proceed through a different mechanism than that found for the achiral, second generation catalyst. Our experimental collaborators have also isolated an inserted species which seems to hinder catalysis. We will additionally investigate this species, seeking an understanding of its formation and stability, and attempt to propose future structural modifications which destabilize the inserted complex. This work has given

valuable insight into the mechanism of aziridination by iron-tetracarbene complexes which can be used to design future catalysts for azirdination, allowing for low-alkene loading and high stereochemical retention.

Bibliography

[1] Phillips, C. R. *Am. J. Hyg.* **1949**, *50*, 280–288. 1

[2] Phillips, C. R.; Kaye, S. *Am. J. Hyg.* **1949**, *50*, 270–279. 1

[3] Beijnen, J. H.; Lingeman, H.; van Munster, H. A.; Underberg, W. J. M. *J. Pharm. Biomed. Anal.* **1986**, *4*, 275–295. 1, 61

[4] Foulke-Abel, J.; Agbo, H.; Zhang, H.; Mori, S.; Watanabe, C. M. H. *Nat. Prod. Rep.* **2011**, *28*, 693–704. 1, 61

[5] Yue, H.; Zhao, Y.; Ma, X.; Gong, J. *Chem. Soc. Rev.* **2012**, *41*, 4218–4244. 1

[6] Martínez, L. E.; Leighton, J. L.; Carsten, D. H.; Jacobsen, E. N. *J. Am. Chem. Soc.* **1995**, *117*, 5897–5898. 1

[7] Jacobsen, E. N. *Acc. Chem. Res.* **2000**, *33*, 421–431.

[8] Hu, X. E. *Tetrahedron* **2004**, *60*, 2701–2743. 61, 64

[9] Han, Y.; Xie, Y. X.; Zhao, L. B.; Fan, M. J.; Liang, Y. M. *Synthesis* **2008**, *1*, 87–93. 1, 62

[10] Oh, H.-S.; Kang, H.-Y. *J. Org. Chem.* **2012**, *77*, 8792–8796. 2, 61

[11] Brandes, B. D.; Jacobsen, E. N. *J. Org. Chem.* **1994**, *59*, 4378–4380. 2

[12] Xia, Q.-H.; Ge, H.-Q.; Ye, C.-P.; Liu, Z.-M.; Su, K. X. *Chem. Rev.* **2005**, *105*, 1603–1662. 2

[13] Nakatsuji, H.; Hu, Z.-M.; Nakai, H.; Ikeda, K. *Surf. Sci.* **1997**, *387*, 328–341. 2

[14] Ozbek, M. O.; Onal, I.; van Santen, R. A. *J. Catal.* **2011**, *284*, 230–235. 2

[15] Ren, R.; Lü, Y.; Pang, X.; Wang, G. *J. Nat. Gas Chem.* **2011**, *20*, 303–310. 2

[16] Jones, G. S.; Mavrikakis, M.; Barteau, M. A.; Vohs, J. M. *J. Am. Chem. Soc.* **1998**, *120*, 3196–3204. 2

[17] Medlin, J. W.; Barteau, M. A. *J. Phys. Chem. B* **2001**, *105*, 10054–10061.

[18] Linic, S.; Barteau, M. A. *J. Am. Chem. Soc.* **2002**, *124*, 310–317. 39

[19] Linic, S.; Barteau, M. A. *J. Catal.* **2003**, *214*, 200–212.

[20] Lukaski, A. C.; Barteau, M. A. *Catal. Letters* **2009**, *128*, 9–17.

[21] Ozbek, M. O.; Onal, I.; van Santen, R. A. *Top. Catal.* **2012**, *55*, 710–717. 2, 52

[22] Michaelides, A.; Reuter, K.; Scheffler, M. *J. Vac. Sci. Technol. A* **2005**, *23*, 1487–1497. 3, 10, 40

[23] Kolasinski, K. W. *Surface Science: Foundations of Catalysis and Nanoscience*, 3rd ed.; Wiley: Chichester, UK, 2012. 3

[24] Binnig, G.; Rohrer, H.; Gerber, C.; Weibel, E. *Phys. Rev. Lett.* **1982**, *49*, 57–61. 3, 10

[25] Puschmann, A.; Haase, J. *Surf. Sci.* **1984**, *144*, 559–566. 3

[26] Becker, L.; Aminpirooz, S.; Schmalz, A.; Hillert, B.; Pedio, M.; Haase, J. *Phys. Rev. B* **1991**, *44*, 13655–13659. 3

[27] Rovida, G.; Pratesi, F.; Maglietta, M.; Ferroni, E. *Surf. Sci.* **1974**, *43*, 230–256. 3, 10, 39

[28] Campbell, C. T. *Surf. Sci.* **1985**, *157*, 43–60. 4, 39, 45

[29] Schnadt, J.; Michaelides, A.; Knudsen, J.; Vang, R. T.; Reuter, K.; Lægsgaard, E.; Scheffler, M.; Besenbacher, F. *Phys. Rev. Lett.* **2006**, *96*, 146101. 4, 10, 39, 47

[30] Schmid, M.; Reicho, A.; Stierle, A.; Costina, I.; Klikovits, J.; Kostelnik, P.; Dubay, O.; Kresse, G.; Gustafson, J.; Lundgren, E.; Andersen, J. N.; Dosch, H.; Varga, P. *Phys. Rev. Lett.* **2006**, *96*, 146102. 4, 10

[31] Hohenberg, P.; Kohn, W. *Phys. Rev.* **1964**, *136*, B864–B871. 4

[32] Carlisle, C. I.; Fujimoto, T.; Sim, W. S.; King, D. A. *Surf. Sci.* **2000**, *470*, 15–31. 4, 39, 47

[33] Schnadt, J.; Knudsen, J.; Hu, X. L.; Michaelides, A.; Vang, R. T.; Reuter, K.; Li, Z.; Lægsgaard, E.; Scheffler, M.; Besenbacher, F. *Phys. Rev. B* **2009**, *80*, 075424. 4, 10, 37, 39

[34] Martin, N. M.; Klacar, S.; Grönbeck, H.; Knudsen, J.; Schnadt, J.; Blomberg, S.; Gustafson, J.; Lundgren, E. *J. Phys. Chem. C* **2014**, *118*, 15324–15331. 4, 10, 39, 40, 47

[35] Derouin, J.; Farber, R. G.; Turano, M. E.; Iski, E. V.; Killelea, D. R. *ACS Catal.* **2016**, *6*, 4640–4646. 4, 39, 40

[36] Knop-Gericke, A.; Kleimenov, E.; Hävecker, M.; Blume, R.; Teschner, D.; Zafeiratos, S.; Schlögl, R.; Bukhtiyarov, V. I.; Kaichev, V. V.; Prosvirin, I. P.; Nizovskii, A. I.; Bluhm, H.; Barinov, A.; Dudin, P.; Kiskinova, M. *Adv. Catal.* **2009**, *52*, 213–272. 4

[37] Ishikawa, A.; Nakatsuji, H. *J. Comput. Chem.* **2013**, *34*, 1828–1835. 4, 39

[38] Günther, S.; Böcklein, S.; Wintterlin, J.; Niño, M. A.; Menteş, T. O.; Locatelli, A. *ChemCatChem* **2013**, *5*, 3342–3350. 4, 39

[39] Waterhouse, G. I. N.; Bowmaker, G. A.; Metson, J. B. *Appl. Catal. A Gen.* **2004**, *265*, 85–101. 4, 39

[40] Milov, M. A.; Zilberberg, I. L.; Ruzankin, S. P.; Zhidomirov, G. M. *J. Mol. Catal. A Chem.* **2000**, *158*, 309–312. 4, 39

[41] Michaelides, A.; Bocquet, M.-L.; Sautet, P.; Alavi, A.; King, D. A. *Chem. Phys. Lett.* **2003**, *367*, 344–350. 39, 40

[42] Rawal, T. B.; Hong, S.; Pulkkinen, A.; Alatalo, M.; Rahman, T. S. *Phys. Rev. B* **2015**, *92*, 035444. 4, 5, 19, 52, 57

[43] Li, W.-X.; Stampfl, C.; Scheffler, M. *Phys. Rev. B* **2002**, *65*, 075407. 4, 18, 39, 44, 50

[44] Li, W.-X.; Stampfl, C.; Scheffler, M. *Phys. Rev. B* **2003**, *67*, 045408. 4, 18, 39, 44, 50

[45] Backx, C.; de Groot, C. P. M.; Biloen, P. *Surf. Sci.* **1981**, *104*, 300–317. 5

[46] Roy, S.; Mujica, V.; Ratner, M. A. *J. Chem. Phys.* **2013**, *139*, 074702. 5, 18, 52

[47] Zhu, L.; Xu, H.; Nan, Y.; Zhu, J.; Cheng, D. *Comput. Mater. Sci.* **2018**, *155*, 17–27. 5

[48] Ingleson, M. J.; Layfield, R. A. *Chem. Commun.* **2012**, *48*, 3579–3589. 5

[49] Jung, N.; Bräse, S. *Angew. Chemie - Int. Ed.* **2012**, *51*, 5538–5540.

[50] Degennaro, L.; Trinchera, P.; Luisi, R. *Chem. Rev.* **2014**, *114*, 7881–7929.

[51] Pellissier, H. *Adv. Synth. Catal.* **2014**, *356*, 1899–1935. 5

[52] Keller, C. L.; Kern, J. L.; Terry, B. D.; Roy, S.; Jenkins, D. M. *Chem. Commun.* **2018**, *54*, 1429–1432. 6, 7

[53] Klotz, K. L.; Slominski, L. M.; Hull, A. V.; Gottsacker, V. M.; Mas-Ballesté, R.; Que, Jr., L.; Halfen, J. A. *Chem. Commun.* **2007**, *0*, 2063–2065. 6, 61

[54] Liu, P.; Wong, E. L.-M.; Yuen, A. W.-H.; Che, C.-M. *Org. Lett.* **2008**, *10*, 3275–3278. 64

[55] Nakanishi, M.; Salit, A.-F.; Bolm, C. *Adv. Synth. Catal.* **2008**, *350*, 1835–1840. 6

[56] Cramer, S. A.; Jenkins, D. M. *J. Am. Chem. Soc.* **2011**, *133*, 19342–19345. 7, 62, 64, 65, 74

[57] Muñoz III, S. B.; Lee, W. s.; Dickie, D. A.; Scepaniak, J. J.; Subedi, D.; Pink, M.; Johnson, M. D.; Smith, J. M. *Angew. Chemie - Int. Ed.* **2015**, *54*, 10600–10603.

[58] Chandrachud, P. P.; Bass, H. M.; Jenkins, D. M. *Organometallics* **2016**, *35*, 1652–1657. 7, 62, 64, 65, 69, 77

[59] Shehata, M. F.; Ayer, S. K.; Roizen, J. L. *J. Org. Chem.* **2018**, *83*, 5072–5081. 6

[60] Zdilla, M. J.; Abu-Omar, M. M. *J. Am. Chem. Soc.* **2006**, *128*, 16971–16979. 6, 61

[61] Gao, G.-Y.; Jones, J. E.; Vyas, R.; Harden, J. D.; Zhang, X. P. *J. Org. Chem.* **2006**, *71*, 6655–6658. 6, 61, 62

[62] Ruppel, J. V.; Jones, J. E.; Huff, C. A.; Kamble, R. M.; Chen, Y.; Zhang, X. P. *Org. Lett.* **2008**, *10*, 1995–1998. 6

[63] Jones, J. E.; Ruppel, J. V.; Gao, G.-Y.; Moore, T. M.; Zhang, X. P. *J. Org. Chem.* **2008**, *73*, 7260–7265. 6, 62

[64] Hopmann, K. H.; Ghosh, A. *ACS Catal.* **2011**, *1*, 597–600. 6, 8, 62, 64, 66, 67, 69, 70, 84

[65] Olivos Suarez, A. I.; Jiang, H.; Zhang, X. P.; de Bruin, B. *Dalt. Trans.* **2011**, *40*, 5697–5705. 6, 65

[66] Jin, L.-M.; Xu, X.; Lu, H.; Cui, X.; Wojtas, L.; Zhang, X. P. *Angew. Chemie - Int. Ed.* **2013**, *52*, 5309–5313. 64

[67] Tao, J.; Jin, L.-M.; Zhang, X. P. *Beilstein J. Org. Chem.* **2014**, *10*, 1282–1289. 6, 62

[68] Evans, D. A.; Faul, M. M.; Bilodeau, M. T. *J. Am. Chem. Soc.* **1994**, *116*, 2742–2753. 6, 62, 72

[69] Xu, Q.; Appella, D. H. *Org. Lett.* **2008**, *10*, 1497–1500.

[70] Nebra, N.; Lescot, C.; Dauban, P.; Mallet-Ladeira, S.; Martin-Vaca, B.; Bourissou, D. *European J. Org. Chem.* **2013**, 984–990. 6, 61

[71] Au, S.-M.; Huang, J.-S.; Yu, W.-Y.; Fung, W.-H.; Che, C.-M. *J. Am. Chem. Soc.* **1999**, *121*, 9120–9132. 6, 64

[72] Kawabata, H.; Omura, K.; Katsuki, T. *Tetrahedron Lett.* **2006**, *47*, 1571–1574. 6, 62

[73] Kawabata, H.; Omura, K.; Uchida, T.; Katsuki, T. *Chem. Asian J.* **2007**, *2*, 248–256. 6, 62

[74] Fantauzzi, S.; Gallo, E.; Caselli, A.; Piangiolino, C.; Ragaini, F.; Cenini, S. *European J. Org. Chem.* **2007**, 6053–6059. 6, 62

[75] Chan, K.-H.; Guan, X.; Lo, V. K.-Y.; Che, C.-M. *Angew. Chemie - Int. Ed.* **2014**, *53*, 2982–2987. 6

[76] Jat, J. L.; Paudyal, M. P.; Gao, H.; Xu, Q.-L.; Yousufuddin, M.; Devarajan, D.; Ess, D. H.; Kürti, L.; Falck, J. R. *Science* **2014**, *343*, 61–65. 6

[77] Zardi, P.; Pozzoli, A.; Ferretti, F.; Manca, G.; Mealli, C.; Gallo, E. *Dalt. Trans.* **2015**, *44*, 10479–10489. 6, 8, 62, 64, 66, 67, 69, 70, 84

[78] Cramer, S. A.; Hernández Sánchez, R.; Brakhage, D. F.; Jenkins, D. M. *Chem. Commun.* **2014**, *50*, 13967–13970. 7, 62, 64, 67, 69, 75, 77

[79] Isbill, S. B.; Roy, S.; Keffer, D. J. *Mol. Simul.* **2017**, *43*, 355–369. 9

[80] Campbell, C. T. *J. Catal.* **1986**, *99*, 28–38. 10, 37, 47

[81] Carlisle, C. I.; King, D. A.; Bocquet, M.-L.; Cerdá, J.; Sautet, P. *Phys. Rev. Lett.* **2000**, *84*, 3899–3902. 10

[82] Rehren, C.; Isaac, G.; Schlögl, R.; Ertl, G. *Catal. Letters* **1991**, *11*, 253–266. 10, 37

[83] Bao, X.; Muhler, M.; Schedel-Niedrig, T.; Schlögl, R. *Phys. Rev. B* **1996**, *54*, 2249–2262. 10, 37

[84] Lloyd, A.; Cornil, D.; van Duin, A. C. T.; van Duin, D.; Smith, R.; Kenny, S. D.; Cornil, J.; Beljonne, D. *Surf. Sci.* **2016**, *645*, 67–73. 11, 15, 23

[85] Daw, M. S.; Foiles, S. M.; Baskes, M. I. *Mater. Sci. Reports* **1993**, *9*, 251–310. 12

[86] Gale, J. D. *Philos. Mag.* **2016**, *73*, 3–19. 12

[87] Devine, B.; Shan, T. R.; Cheng, Y. T.; McGaughey, A. J. H.; Lee, M.; Phillpot, S. R.; Sinnott, S. B. *Phys. Rev. B* **2011**, *84*, 125308. 12

[88] Yu, J.; Sinnott, S. B.; Phillpot, S. R. *Phys. Rev. B* **2007**, *75*, 085311. 12

[89] Shan, T.-R.; Devine, B. D.; Phillpot, S. R.; Sinnott, S. B. *Phys. Rev. B* **2011**, *83*, 115327. 12

[90] Plimpton, S. *J. Comput. Phys.* **1995**, *117*, 1–19. 12

[91] Nosé, S. *Mol. Phys.* **2002**, *100*, 191–198. 12

[92] Verlet, L. *Phys. Rev* **1967**, *159*, 98–103. 12

[93] Hoover, W. G. *Phys. Rev. A* **1985**, *31*, 1695–1697. 12

[94] Kresse, G.; Hafner, J. *Phys. Rev. B* **1994**, *49*, 14251–14269. 13, 40

[95] Kresse, G.; Furthmüller, J. *Comput. Mater. Sci.* **1996**, *6*, 15–50. 13, 40

[96] Perdew, J. P.; Ruzsinszky, A.; Csonka, G. I.; Vydrov, O. A.; Scuseria, G. E.; Constantin, L. A.; Zhou, X.; Burke, K. *Phys. Rev. Lett.* **2008**, *100*, 136406. 13

[97] Ashcroft, N.; Mermin, N. *Solid State Physics*, 1st ed.; Brooks Cole: Belmount, 1976. 13, 15, 40

[98] Blöchl, P. E. *Phys. Rev. B* **1994**, *50*, 17953–17979. 13, 40

[99] Monkhorst, H. J.; Pack, J. D. *Phys. Rev. B* **1976**, *13*, 5188–5192. 13, 40

[100] Methfessel, M.; Paxton, A. T. *Phys. Rev. B* **1989**, *40*, 3616–3621. 13, 40

[101] Kumikov, V. K.; Khokonov, K. B. *J. Appl. Phys.* **1983**, *54*, 1346–1350. 16

[102] Bonzel, H. P.; Nowicki, M. *Phys. Rev. B* **2004**, *70*, 245430. 17

[103] Brewer, L.; Rosenblatt, G. M. *Adv. High. Temp. Sci.* **1969**, *2*, 1. 18

[104] Kunisada, Y.; Nakanishi, H.; Diño, W. A.; Kasai, H. *J. Phys. Conf. Ser.* **2012**, *379*, 012013. 18

[105] Rovida, G.; Pratesi, F.; Maglietta, M.; Ferroni, E. *J. Vac. Sci. Technol.* **1972**, *9*, 796. 39

[106] de Mongeot, F. B.; Valbusa, U.; Rocca, M. *Surf. Sci.* **1995**, *339*, 291–296.

[107] Boronin, A. I.; Koscheev, S. V.; Zhidomirov, G. M. *J. Electron Spectros. Relat. Phenomena* **1998**, *96*, 43–51. 39

[108] Avdeev, V. I.; Zhidomirov, G. M. *Surf. Sci.* **2001**, *492*, 137–151.

[109] Li, W.-X.; Stampfl, C.; Scheffler, M. *Phys. Rev. Lett.* **2003**, *90*, 256102. 40, 59

[110] Xu, Y.; Greeley, J.; Mavrikakis, M. *J. Am. Chem. Soc.* **2005**, *127*, 12823–12827. 39

[111] Greeley, J.; Mavrikakis, M. *J. Phys. Chem. C* **2007**, *111*, 7992–7999.

[112] Derouin, J.; Farber, R. G.; Heslop, S. L.; Killelea, D. R. *Surf. Sci.* **2015**, *641*, L1–L4.

[113] Jones, T. E.; Rocha, T. C. R.; Knop-Gericke, A.; Stampfl, C.; Schlögl, R.; Piccinin, S. *Phys. Chem. Chem. Phys.* **2015**, *17*, 9288–9312. 39

[114] Jones, T. E.; Rocha, T. C. R.; Knop-Gericke, A.; Stampfl, C.; Schlögl, R.; Piccinin, S. *ACS Catal.* **2015**, *5*, 5846–5850.

[115] Heine, C.; Eren, B.; Lechner, B. A. J.; Salmeron, M. *Surf. Sci.* **2016**, *652*, 51–57. 39

[116] Carbonio, E. A.; Rocha, T. C. R.; Klyushin, A. Y.; Píš, I.; Magnano, E.; Nappini, S.; Piccinin, S.; Knop-Gericke, A.; Schlögl, R.; Jones, T. E. *Chem. Sci.* **2018**, *9*, 990–998.

[117] Kenge, N.; Pitale, S.; Joshi, K. *Surf. Sci.* **2018**, *679*, 188–195. 39

[118] Schedel-Niedrig, T.; Schlögl, R.; Bao, X.; Muhler, M. *Berichte der Bunsengesellschaft für Phys. Chemie* **2010**, *101*, 994–1006. 39

[119] Bocquet, M.-L.; Michaelides, A.; Sautet, P.; King, D. A. *Phys. Rev. B* **2003**, *68*, 075413. 40

[120] Kresse, G.; Hafner, J. *Phys. Rev. B* **1993**, *47*, 558–561. 40

[121] Kresse, G.; Furthmüller, J. *Phys. Rev. B* **1996**, *54*, 11169–11186. 40

[122] Perdew, J. P.; Burke, K.; Ernzerhof, M. *Phys. Rev. Lett.* **1996**, *77*, 3865–3868. 40

[123] Perdew, J. P.; Burke, K.; Ernzerhof, M. *Phys. Rev. Lett.* **1997**, *78*, 1396. 40

[124] Kresse, G.; Joubert, D. *Phys. Rev. B* **1999**, *59*, 1758–1775. 40

[125] Chelvayohan, M.; Mee, C. H. B. *J. Phys. C Solid State Phys.* **1982**, *15*, 2305–2312. 41, 53

[126] Tang, W.; Sanville, E.; Henkelman, G. *J. Phys. Condens. Matter* **2009**, *21*, 084204. 42

[127] Sanville, E.; Kenny, S. D.; Smith, R.; Henkelman, G. *J. Comput. Chem.* **2007**, *28*, 899–908.

[128] Henkelman, G.; Arnaldsson, A.; Jónsson, H. *Comput. Mater. Sci.* **2006**, *36*, 354–360. 42

[129] Redhead, P. A. *Vacuum* **1962**, *12*, 203–211. 47

[130] Bare, S. R. *J. Vac. Sci. Technol. A* **1992**, *10*, 2336–2341. 52

[131] Gravil, P. A.; Bird, D. M.; White, J. A. *Phys. Rev. Lett.* **1996**, *77*, 3933–3936. 52

[132] van den Hoek, P. J.; Baerends, E. J.; van Santen, R. A. *J. Phys. Chem.* **1989**, *93*, 6469–6475. 52

[133] Jenkins, D. M. *Synlett* **2012**, *23*, 1267–1270. 61

[134] Goswami, M. et al. *J. Am. Chem. Soc.* **2015**, *137*, 5468–5479.

[135] Mukherjee, M.; Gupta, A. K.; Lu, Z.; Zhang, Y.; Wulff, W. D. *J. Org. Chem.* **2010**, *75*, 5643–5660.

[136] Avenier, F.; Latour, J.-M. *Chem. Commun.* **2004**, *0*, 1544–1545. 61

[137] Ismail, F. M. D.; Levitsky, D. O.; Dembitsky, V. M. *Eur. J. Med. Chem.* **2009**, *44*, 3373–3387. 61

[138] Lu, P. *Tetrahedron* **2010**, *66*, 2549–2560. 61

[139] Schneider, C. *Angew. Chemie - Int. Ed.* **2009**, *48*, 2082–2084.

[140] Njardarson, J. T. *Synlett* **2013**, *24*, 0787–0803.

[141] Lu, S.-M.; Alper, H. *J. Org. Chem.* **2004**, *69*, 3558–3561.

[142] Wang, J.-Y.; Hu, Y.; Wang, D.-X.; Pan, J.; Huang, Z.-T.; Wang, M.-X. *Chem. Commun.* **2009**, *0*, 422–424.

[143] Kim, M. S.; Kim, Y.-W.; Hahm, H. S.; Jang, J. W.; Lee, W. K.; Ha, H.-J. *Chem. Commun.* **2005**, *0*, 3062–3064. 61

[144] Ghorai, M. K.; Shahi, C. K.; Bhattacharyya, A.; Sayyad, M.; Mal, A.; Wani, I. A.; Chauhan, N. *Asian J. Org. Chem.* **2015**, *4*, 1103–1111. 61

[145] Huang, Y.-M.; Zheng, C.-W.; Pan, L.; Jin, Q.-W.; Zhao, G. *J. Org. Chem.* **2015**, *80*, 10710–10718. 62

[146] Wang, Y.-N.; Li, T.-R.; Zhang, M.-M.; Cheng, B.-Y.; Lu, L.-Q.; Xiao, W.-J. *J. Org. Chem.* **2016**, *81*, 10491–10498.

[147] Yang, D.; Wang, L.; Han, F.; Li, D.; Zhao, D.; Cao, Y.; Ma, Y.; Kong, W.; Sun, Q.; Wang, R. *Chem. Eur. J.* **2014**, *20*, 16478–16483. 62

[148] Yudin, A. *Aziridines and Epoxides in Organic Synthesis*; Wiley-VCH: Weinheim, 2007. 62

[149] Minakata, S. *Acc. Chem. Res.* **2009**, *42*, 1172–1182. 62

[150] Caselli, A.; Gallo, E.; Fantauzzi, S.; Morlacchi, S.; Ragaini, F.; Cenini, S. *Eur. J. Inorg. Chem.* **2008**, 3009–3019. 62, 64

[151] Bräse, S.; Gil, C.; Knepper, K.; Zimmermann, V. *Angew. Chemie - Int. Ed.* **2005**, *44*, 5188–5240.

[152] Heydt, H.; Regitz, M.; Mapp, A. K.; Chen, B. *Encyclopedia of Reagents for Organic Synthesis*; John Wiley & Sons, Ltd, 2001.

[153] Nishioka, Y.; Uchida, T.; Katsuki, T. *Angew. Chemie - Int. Ed.* **2013**, *52*, 1739–1742. 62

[154] Frisch, M. J. et al. Gaussian 09 Revision D.01. Gaussian Inc. Wallingford CT 2009. 64, 81

[155] Tao, J.; Perdew, J. P.; Staroverov, V. N.; Scuseria, G. E. *Phys. Rev. Lett.* **2003**, *91*, 146401. 64, 81

[156] Weigend, F.; Ahlrichs, R. *Phys. Chem. Chem. Phys.* **2005**, *7*, 3297–3305. 64, 81

[157] Weigend, F. *Phys. Chem. Chem. Phys.* **2006**, *8*, 1057–1065. 64, 81

[158] Grimme, S.; Antony, J.; Ehrlich, S.; Krieg, H. *J. Chem. Phys.* **2010**, *132*, 154104. 64, 81

[159] Grimme, S.; Ehrlich, S.; Goerigk, L. *J. Comput. Chem.* **2011**, *32*, 1456–1465. 64, 81

[160] Fantauzzi, S.; Caselli, A.; Gallo, E. *Dalt. Trans.* **2009**, 5434–5443. 64

[161] Searles, K.; Fortier, S.; Khusniyarov, M. M.; Carroll, P. J.; Sutter, J.; Meyer, K.; Mindiola, D. J.; Caulton, K. G. *Angew. Chemie - Int. Ed.* **2014**, *53*, 14139–14143. 64

[162] Bowman, A. C.; Milsmann, C.; Bill, E.; Turner, Z. R.; Lobkovsky, E.; DeBeer, S.; Wieghardt, K.; Chirik, P. J. *J. Am. Chem. Soc.* **2011**, *133*, 17353–17369.

[163] Bart, S. C.; Lobkovsky, E.; Bill, E.; Chirik, P. J. *J. Am. Chem. Soc.* **2006**, *128*, 5302–5303. 66

[164] Brown, S. D.; Betley, T. A.; Peters, J. C. *J. Am. Chem. Soc.* **2003**, *125*, 322–323.

[165] Takaoka, A.; Gerber, L. C. H.; Peters, J. C. *Angew. Chemie - Int. Ed.* **2010**, *49*, 4088–4091.

[166] King, E. R.; Sazama, G. T.; Betley, T. A. *J. Am. Chem. Soc.* **2012**, *134*, 17858–17861.

[167] Shay, D. T.; Yap, G. P. A.; Zakharov, L. N.; Rheingold, A. L.; Theopold, K. H. *Angew. Chemie - Int. Ed.* **2005**, *44*, 1508–1510. 64

[168] King, E. R.; Hennessy, E. T.; Betley, T. A. *J. Am. Chem. Soc.* **2011**, *133*, 4917–4923. 64, 66

[169] Albertin, G.; Antoniutti, S.; Baldan, D.; Castro, J.; García-Fontán, S. *Inorg. Chem.* **2008**, *47*, 742–748. 65

[170] Barz, M.; Herdtweck, E.; Thiel, W. R. *Angew. Chemie - Int. Ed.* **1998**, *37*, 2262–2265.

[171] Dias, H. V. R.; Polach, S. A.; Goh, S.-K.; Archibong, E. F.; Marynick, D. S. *Inorg. Chem.* **2000**, *39*, 3894–3901.

[172] Grant, L. N.; Carroll, M. E.; Carroll, P. J.; Mindiola, D. J. *Inorg. Chem.* **2016**, *55*, 7997–8002. 65

[173] Takaoka, A.; Moret, M.-E.; Peters, J. C. *J. Am. Chem. Soc.* **2012**, *134*, 6695–6706. 66

[174] Cowley, R. E.; Holland, P. L. *Inorg. Chem.* **2012**, *51*, 8352–8361. 66

[175] Lin, Z.; Hall, M. B. *Coord. Chem. Rev.* **1993**, *123*, 149–167. 66

[176] Mehn, M. P.; Peters, J. C. *J. Inorg. Biochem.* **2006**, *100*, 634–643. 66

[177] Hennessy, E. T.; Liu, R. Y.; Iovan, D. A.; Duncan, R. A.; Betley, T. A. *Chem. Sci.* **2014**, *5*, 1526–1532. 72

[178] Meyer, N. H.; Zangger, K. *Angew. Chemie - Int. Ed.* **2013**, *52*, 7143–7146.

[179] Nishida, T.; Widmalm, G.; Sandor, P. *Magn. Reson. Chem.* **1995**, *33*, 596–599.

[180] Bull, J. A.; Boultwood, T.; Taylor, T. A. *Chem. Commun.* **2012**, *48*, 12246–12248. 72

[181] Sasaki, M.; Yudin, A. K. *J. Am. Chem. Soc.* **2003**, *125*, 14242–14243. 72

[182] Chen, G.; Sasaki, M.; Li, X.; Yudin, A. K. *J. Org. Chem.* **2006**, *71*, 6067–6073.

[183] Wróblewski, A. E.; Drozd, J. *Tetrahedron: Asymmetry* **2011**, *22*, 200–206. 72

[184] Meyer, K. E.; Walsh, P. J.; Bergman, R. G. *J. Am. Chem. Soc.* **1995**, *117*, 974–985. 75, 76

[185] Cowley, R. E.; Bill, E.; Neese, F.; Brennessel, W. W.; Holland, P. L. *Inorg. Chem.* **2009**, *48*, 4828–4836. 75

[186] Mock, M. T.; Popescu, C. V.; Yap, G. P. A.; Dougherty, W. G.; Riordan, C. G. *Inorg. Chem.* **2008**, *47*, 1889–1891. 75

[187] Otten, B. M.; Figg, T. M.; Cundari, T. R. *Inorg. Chem.* **2014**, *53*, 11633–11639. 76

[188] Ren, W.; Zhou, E.; Fang, B.; Hou, G.; Zi, G.; Fang, D.-C.; Walter, M. D. *Angew. Chemie - Int. Ed.* **2014**, *53*, 11310–11314.

[189] Vaddypally, S.; McKendry, I. G.; Tomlinson, W.; Hooper, J. P.; Zdilla, M. J. *Chem. Eur. J.* **2016**, *22*, 10548–10557. 76

[190] Nguyen, L. A.; He, H.; Pham-Huy, C. *Int. J. Biomed. Sci.* **2006**, *2*, 85–100. 80

[191] Hao, H.; Wang, G.; Sun, J. *Drug Metab. Rev.* **2005**, *37*, 215–234. 80

[192] Davies, N. M.; Teng, X. W. *Adv. Pharm.* **2003**, *1*, 242–252. 80

[193] Sanganyado, E.; Lu, Z.; Fu, Q.; Schlenk, D.; Gan, J. *Water Res.* **2017**, *124*, 527–542. 80

Appendix

Appendix A

Additional Tables and Figures from Chapter 2

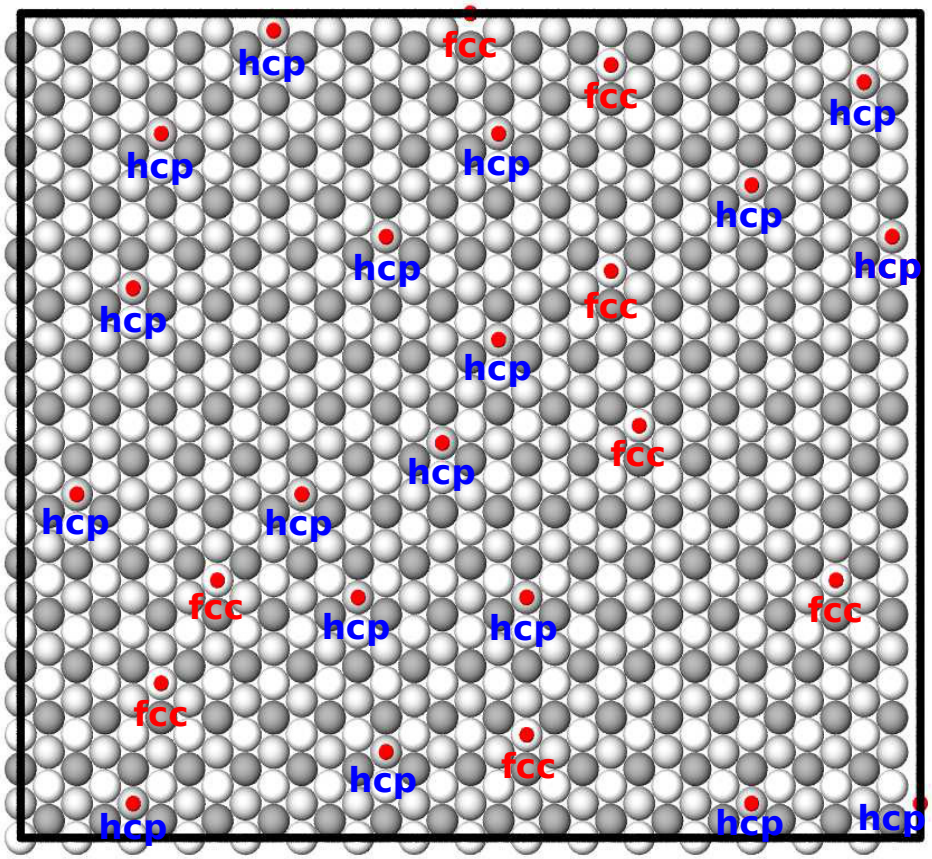


Figure A.1: Location of oxygens that were originally placed at the top site of the (111) surface at a 0.1 fraction coverage after relaxation.

Table A.1: Suite of 153 simulations performed the molecular dynamics investigations of the interaction of atomic oxygen with Ag(111) and Ag(110).

JobID	Miller index of surface	oxygen location	symmetry site	factional occupancy	temperature (K)
001	(111)	surface	top	0.1	77
002	(111)	surface	top	0.1	300
003	(111)	surface	top	0.1	500
004	(111)	surface	top	0.5	77
005	(111)	surface	top	0.5	300
006	(111)	surface	top	0.5	500
007	(111)	surface	top	1.0	77
008	(111)	surface	top	1.0	300
009	(111)	surface	top	1.0	500
010	(111)	surface	bridge	0.1	77
011	(111)	surface	bridge	0.1	300
012	(111)	surface	bridge	0.1	500
013	(111)	surface	bridge	0.5	77
014	(111)	surface	bridge	0.5	300
015	(111)	surface	bridge	0.5	500
016	(111)	surface	bridge	1.0	77
017	(111)	surface	bridge	1.0	300
018	(111)	surface	bridge	1.0	500
019	(111)	surface	fcc hollow	0.1	77
020	(111)	surface	fcc hollow	0.1	300
021	(111)	surface	fcc hollow	0.1	500
022	(111)	surface	fcc hollow	0.5	77
023	(111)	surface	fcc hollow	0.5	300
024	(111)	surface	fcc hollow	0.5	500

Table A.1 Continued.

JobID	Miller index of surface	oxygen location	symmetry site	factional occupancy	temperature (K)
025	(111)	surface	fcc hollow	1.0	77
026	(111)	surface	fcc hollow	1.0	300
027	(111)	surface	fcc hollow	1.0	500
028	(111)	surface	hcp hollow	0.1	77
029	(111)	surface	hcp hollow	0.1	300
030	(111)	surface	hcp hollow	0.1	500
031	(111)	surface	hcp hollow	0.5	77
032	(111)	surface	hcp hollow	0.5	300
033	(111)	surface	hcp hollow	0.5	500
034	(111)	surface	hcp hollow	1.0	77
035	(111)	surface	hcp hollow	1.0	300
036	(111)	surface	hcp hollow	1.0	500
037	(111)	subsurface	tetrahedral-1	0.1	77
038	(111)	subsurface	tetrahedral-1	0.1	300
039	(111)	subsurface	tetrahedral-1	0.1	500
040	(111)	subsurface	tetrahedral-1	0.5	77
041	(111)	subsurface	tetrahedral-1	0.5	300
042	(111)	subsurface	tetrahedral-1	0.5	500
043	(111)	subsurface	tetrahedral-1	1.0	77
044	(111)	subsurface	tetrahedral-1	1.0	300
045	(111)	subsurface	tetrahedral-1	1.0	500
046	(111)	subsurface	tetrahedral-3	0.1	77
047	(111)	subsurface	tetrahedral-3	0.1	300
048	(111)	subsurface	tetrahedral-3	0.1	500
049	(111)	subsurface	tetrahedral-3	0.5	77

Table A.1 Continued.

JobID	Miller index of surface	oxygen location	symmetry site	factional occupancy	temperature (K)
050	(111)	subsurface	tetrahedral-3	0.5	300
051	(111)	subsurface	tetrahedral-3	0.5	500
052	(111)	subsurface	tetrahedral-3	1.0	77
053	(111)	subsurface	tetrahedral-3	1.0	300
054	(111)	subsurface	tetrahedral-3	1.0	500
055	(111)	subsurface	octahedral	0.1	77
056	(111)	subsurface	octahedral	0.1	300
057	(111)	subsurface	octahedral	0.1	500
058	(111)	subsurface	octahedral	0.5	77
059	(111)	subsurface	octahedral	0.5	300
060	(111)	subsurface	octahedral	0.5	500
061	(111)	subsurface	octahedral	1.0	77
062	(111)	subsurface	octahedral	1.0	300
063	(111)	subsurface	octahedral	1.0	500
064	(111)	surface & subsurface	fcc hollow & octahedral	0.1	77
065	(111)	surface & subsurface	fcc hollow & octahedral	0.1	300
066	(111)	surface & subsurface	fcc hollow & octahedral	0.1	500
067	(111)	surface & subsurface	fcc hollow & octahedral	0.5	77
068	(111)	surface & subsurface	fcc hollow & octahedral l	0.5	300
069	(111)	surface & subsurface	fcc hollow & octahedral	0.5	500
070	(111)	surface & subsurface	fcc hollow & octahedral	1.0	77
071	(111)	surface & subsurface	fcc hollow & octahedral	1.0	300
072	(111)	surface & subsurface	fcc hollow & octahedral	1.0	500
073	(110)	surface	top	0.1	77

Table A.1 Continued.

JobID	Miller index of surface	oxygen location	symmetry site	factional occupancy	temperature (K)
074	(110)	surface	top	0.1	300
075	(110)	surface	top	0.1	500
076	(110)	surface	top	0.5	77
077	(110)	surface	top	0.5	300
078	(110)	surface	top	0.5	500
079	(110)	surface	top	1.0	77
080	(110)	surface	top	1.0	300
081	(110)	surface	top	1.0	500
082	(110)	surface	short bridge	0.1	77
083	(110)	surface	short bridge	0.1	300
084	(110)	surface	short bridge	0.1	500
085	(110)	surface	short bridge	0.5	77
086	(110)	surface	short bridge	0.5	300
087	(110)	surface	short bridge	0.5	500
088	(110)	surface	short bridge	1.0	77
089	(110)	surface	short bridge	1.0	300
090	(110)	surface	short bridge	1.0	500
091	(110)	surface	long bridge	0.1	77
092	(110)	surface	long bridge	0.1	300
093	(110)	surface	long bridge	0.1	500
094	(110)	surface	long bridge	0.5	77
095	(110)	surface	long bridge	0.5	300
096	(110)	surface	long bridge	0.5	500
097	(110)	surface	long bridge	1.0	77
098	(110)	surface	long bridge	1.0	300

Table A.1 Continued.

JobID	Miller index of surface	oxygen location	symmetry site	factional occupancy	temperature (K)
099	(110)	surface	long bridge	1.0	500
100	(110)	surface	fourfold hollow	0.1	77
101	(110)	surface	fourfold hollow	0.1	300
102	(110)	surface	fourfold hollow	0.1	500
103	(110)	surface	fourfold hollow	0.5	77
104	(110)	surface	fourfold hollow	0.5	300
105	(110)	surface	fourfold hollow	0.5	500
106	(110)	surface	fourfold hollow	1.0	77
107	(110)	surface	fourfold hollow	1.0	300
108	(110)	surface	fourfold hollow	1.0	500
109	(110)	subsurface	square pyramidal-1	0.1	77
110	(110)	subsurface	square pyramidal-1	0.1	300
111	(110)	subsurface	square pyramidal-1	0.1	500
112	(110)	subsurface	square pyramidal-1	0.5	77
113	(110)	subsurface	square pyramidal-1	0.5	300

Table A.1 Continued.

JobID	Miller index of surface	oxygen location	symmetry site	factional occupancy	temperature (K)
114	(110)	subsurface	square pyramidal-1	0.5	500
115	(110)	subsurface	square pyramidal-1	1.0	77
116	(110)	subsurface	square pyramidal-1	1.0	300
117	(110)	subsurface	square pyramidal-1	1.0	500
118	(110)	subsurface	square pyramidal-4	0.1	77
119	(110)	subsurface	square pyramidal-4	0.1	300
120	(110)	subsurface	square pyramidal-4	0.1	500
121	(110)	subsurface	square pyramidal-4	0.5	77

Table A.1 Continued.

JobID	Miller index of surface	oxygen location	symmetry site	factional occupancy	temperature (K)
122	(110)	subsurface	square pyramidal-4	0.5	300
123	(110)	subsurface	square pyramidal-4	0.5	500
124	(110)	subsurface	square pyramidal-4	1.0	77
125	(110)	subsurface	square pyramidal-4	1.0	300
126	(110)	subsurface	square pyramidal-4	1.0	500
127	(110)	subsurface	long subsurface bridge	0.1	77
128	(110)	subsurface	long subsurface bridge	0.1	300
129	(110)	subsurface	long subsurface bridge	0.1	500
130	(110)	subsurface	long subsurface bridge	0.5	77
131	(110)	subsurface	long subsurface bridge	0.5	300

Table A.1 Continued.

JobID	Miller index of surface	oxygen location	symmetry site	factional occupancy	temperature (K)
132	(110)	subsurface	long subsurface bridge	0.5	500
133	(110)	subsurface	long subsurface bridge	1.0	77
134	(110)	subsurface	long subsurface bridge	1.0	300
135	(110)	subsurface	long subsurface bridge	1.0	500
136	(110)	subsurface	short subsurface bridge	0.1	77
137	(110)	subsurface	short subsurface bridge	0.1	300
138	(110)	subsurface	short subsurface bridge	0.1	500
139	(110)	subsurface	short subsurface bridge	0.5	77
140	(110)	subsurface	short subsurface bridge	0.5	300
141	(110)	subsurface	short subsurface bridge	0.5	500

Table A.1 Continued.

JobID	Miller index of surface	oxygen location	symmetry site	factional occupancy	temperature (K)
142	(110)	subsurface	short subsurface bridge	1.0	77
143	(110)	subsurface	short subsurface bridge	1.0	300
144	(110)	subsurface	short subsurface bridge	1.0	500
145	(110)	surface & subsurface	hollow & square pyramidal-1	0.1	77
146	(110)	surface & subsurface	hollow & square pyramidal-1	0.1	300
147	(110)	surface & subsurface	hollow & square pyramidal-1	0.1	500
148	(110)	surface & subsurface	hollow & square pyramidal-1	0.5	77
149	(110)	surface & subsurface	hollow & square pyramidal-1	0.5	300
150	(110)	surface & subsurface	hollow & square pyramidal-1	0.5	500
151	(110)	surface & subsurface	hollow & square pyramidal-1	1.0	77
152	(110)	surface & subsurface	hollow & square pyramidal-1	1.0	300
153	(110)	surface & subsurface	hollow & square pyramidal-1	1.0	500

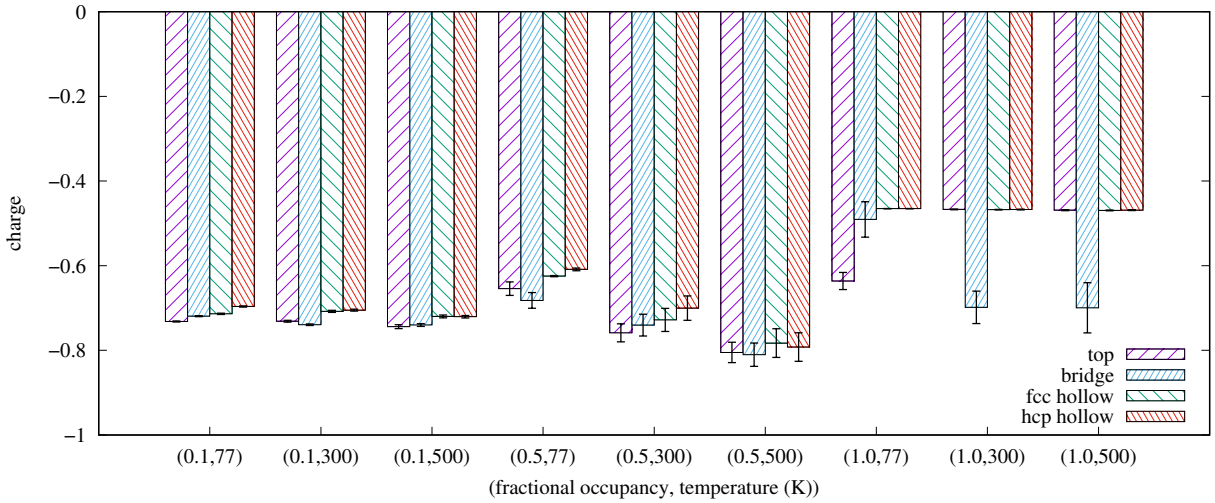


Figure A.2: Time-averaged charge on oxygen as a function of temperature and coverage for the four different initial oxygen sites on t he Ag(111) surface.

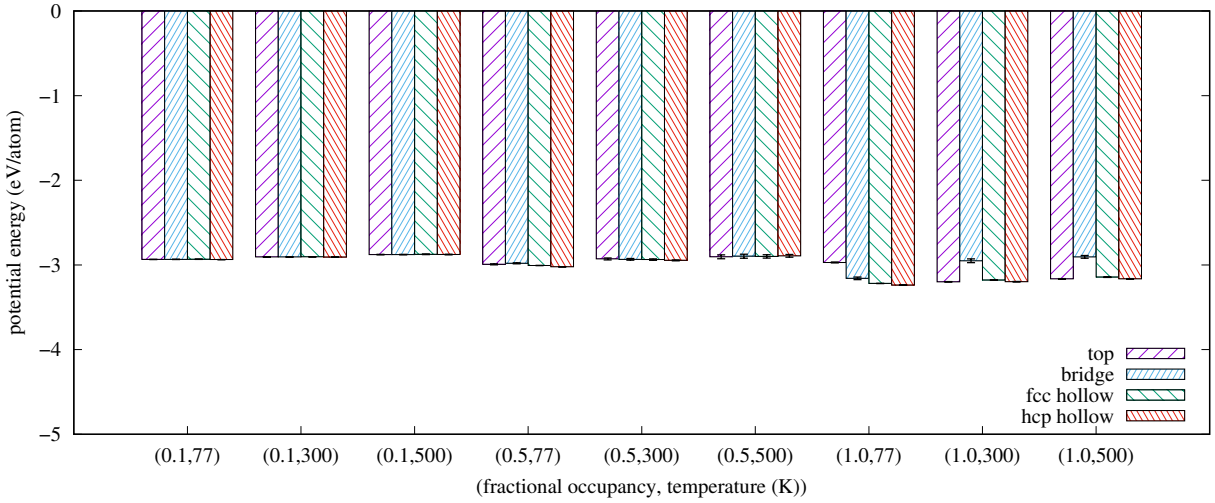


Figure A.3: Time-averaged potential energy of surface silver atoms as a function of temperature and coverage for the four different initial oxygen sites on the Ag(111) surface.

Vita

Sara Isbill is the oldest child of Mike and Shanna Isbill of Madisonville, TN. She graduated from Sequoyah High School in 2010 where she was a member of the cheerleading squad and track and field team. She also was a member of several clubs during her high school career, including Fellowship of Christian Athletes (outreach officer), Beta Club (president), student council (senior class vice president), Science National Honor Society (secretary/treasurer), and Science Olympiad. She briefly attended the University of the Cumberlands (UC) in Williamsburg, KY where she majored in chemistry and was a member of the competitive cheerleading squad. While at UC, she was a presidential scholar and was inducted into the Freshman National Honor Society. Sara transferred to Lee University in Cleveland, TN after her freshman year. While at Lee, Sara continued her involvement with cheerleading, serving as team captain her junior year. She completed her Bachelor of Science degree in May 2014, graduating as the top chemistry major and with high honors. She began at the University of Tennessee, Knoxville as a teaching assistant in the Department of Chemistry in June 2014 before officially beginning her graduate studies in August. While a graduate student, Sara presented the research she performed under the guidance of Professor Sharani Roy at several conferences. She received a departmental teaching award, won travel awards from the American Vacuum Society, received a Young Investigator Award from the Gordon Research Conference on Dynamics at Surfaces, was a winner of a departmental poster competition, and was a winner of the Fundamental Discoveries in Heterogeneous Catalysis Focus Topic student presentation award. She served as a department representative for the Graduate Student Senate for the 2017-2018 academic year where she was a member of the travel awards committee. She has also mentored several undergraduate research students.